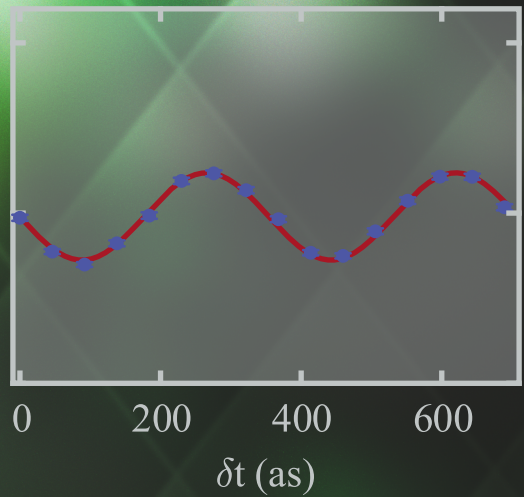
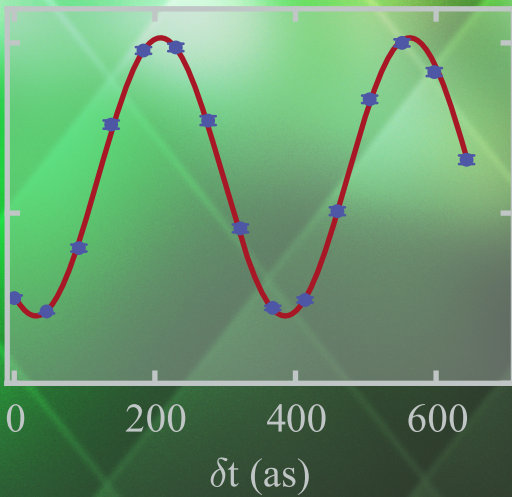


Ramsey-comb spectroscopy in the deep ultraviolet for tests of molecular quantum theory



Robert K. Altmann

**Ramsey-comb spectroscopy in the deep ultraviolet for tests of
molecular quantum theory**

VRIJE UNIVERSITEIT

**Ramsey-comb spectroscopy in the deep ultraviolet
for tests of molecular quantum theory**

ACADEMISCH PROEFSCHRIFT

ter verkrijging van de graad Doctor aan
de Vrije Universiteit Amsterdam
op gezag van de rector magnificus
prof.dr. V. Subramaniam
in het openbaar te verdedigen
ten overstaan van de promotiecommissie
van de Faculteit der Bètawetenschappen
op dinsdag 13 november 2018 om 15.45 uur
in de aula van de universiteit,
Boelelaan 1105

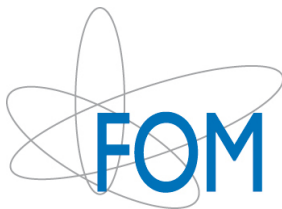
door

Robert Karl Altmann
geboren te Leiden

promotor: prof.dr. K.S.E. Eikema
copromotor: prof.dr. W.M.G. Ubachs

This thesis was approved by the members of the reviewing committee:

Marloes Groot	(Vrije Universiteit Amsterdam)
Frédéric Merkt	(Eidgenössische Technische Hochschule Zürich)
Herman Offerhaus	(University of Twente)
Krzysztof Pachucki	(University of Warsaw)
Florian Schreck	(Universiteit van Amsterdam)



This work was supported by the Foundation for Fundamental Research on Matter (FOM), which was part of the Netherlands Organisation for Scientific Research (NWO), through the program "Broken Mirrors and Drifting Constants", and was carried out at the LaserLaB of the Vrije Universiteit.

Printed by Ridderprint BV
ISBN: 978-94-6375-155-1

Contents

1	Introduction	1
1.1	Spectroscopy and QED	1
1.2	Ramsey-comb spectroscopy	5
1.3	Outline of this thesis	8
2	Frequency-comb laser and Ramsey-comb spectroscopy	9
2.1	Introduction	9
2.2	Optical frequency combs	9
2.2.1	The frequency-comb laser	10
2.2.2	Spectrum of two frequency-comb pulses	14
2.2.3	Spectroscopy with frequency combs	15
2.3	Frequency upconversion and parametric amplification	17
2.4	Ramsey-comb spectroscopy with frequency-comb pulse pairs	21
2.4.1	A Ramsey-comb measurement	24
3	The Ramsey-comb setup: from a frequency-comb laser to a high-intensity phase-stable pulse pair	35
3.1	Introduction	35
3.2	The frequency-comb laser	36
3.3	The pump laser system	42
3.3.1	The pump laser oscillator	42
3.3.2	The bounce amplifier	43
3.3.3	The post amplifier	45
3.3.4	Repetition rate synchronization	47
3.4	The non-collinear optical parametric amplifier	49
3.5	The phase measurement setup	50
3.5.1	Self reference calibration	54
3.5.2	Influence of the pump pulse intensity on the phase in the NOPCPA	58
3.5.3	Spectral dependence of the phase	60
3.6	Conclusion	62
4	High-precision Ramsey-comb spectroscopy on the two-photon $4p^6 \rightarrow 4p^5 5p[1/2]_0$ transition in krypton at 212.55 nm	65
4.1	Abstract	65

4.2	Introduction	65
4.3	Ramsey-comb method	67
4.4	Experimental setup	68
4.5	Ramsey signals at 212 nm	73
4.6	Calibration of systematic effects	75
4.6.1	Doppler shift	75
4.6.2	Phase shift	76
4.6.3	DC-Stark shift	77
4.6.4	AC-Stark shift	78
4.6.5	Detector gain shift	78
4.6.6	Zeeman shift	78
4.7	Isotope shifts	78
4.8	Conclusion	79
5	Deep UV Ramsey-comb spectroscopy of H₂ for fundamental tests of molecular quantum theory.	83
5.1	Abstract	83
5.2	Introduction	83
5.3	Ramsey excitation with frequency comb pulses	86
5.4	Experimental setup	86
5.5	Parametric amplifier phase shift	89
5.6	Results and systematic errors	92
5.6.1	Doppler shift	94
5.6.2	AC-Stark shift	96
5.6.3	DC-Stark shift	96
5.6.4	Zeeman shift	97
5.7	Conclusion	97
6	Outlook	101
6.1	Molecular hydrogen	101
6.2	Extension to the XUV: Towards spectroscopy on the 1S-2S transition in He ⁺	102
A	Excitation with two phase coherent laser pulses	103
	Bibliography	111
	Summary	127

Samenvatting	131
Acknowledgements	135

Introduction

1

1.1 Spectroscopy and QED

The electronic energy structure of an atom or molecule below the ionization limit is quantized, which means that it can only take on specific values in discrete steps, associated with so called quantum states. To change from one quantum state to another the energy difference is typically provided or taken away in the form of a photon. By recording the response of a quantum absorber as function of the photon energy, which is described by its frequency, a line spectrum is obtained. The experimental interrogation of an absorber and the acquisition and study of the resulting line spectra is called the science of spectroscopy. The characteristics of the lines in a spectrum, such as the transition frequency or linewidth, provide information about fundamental properties of the atom or molecule that is examined. This information can be used to understand the system by comparing the experimental results with a theory or model.

The basic theory that describes the electronic energy level structure is quantum mechanics, and spectroscopy has played an important role in its development over the last one hundred years or so. An essential test subject for the development of the theoretical framework was (and still is) the hydrogen atom, which due to its simplicity (only one electron orbiting a single proton), allows for exact analytic solutions. One of the first breakthrough's towards the explanation of the observed line spectrum of hydrogen was Bohr's model for the atom, put forward in 1913 [1]. However, Bohr's model proved to be an incomplete description of the hydrogen atom as there were certain discrepancies between the observed spectral features and the predictions made by the theory, e.g. some lines were split into "doublets". It first took the development of quantum mechanics by Schrödinger and Heisenberg and later the relativistic version of quantum mechanics by Dirac in 1929 to explain these spectral features [2, 3].

With advances in spectroscopic methods the determination of energy levels in the hydrogen atom became more precise, pushing the boundaries of the theoretical models. This resulted in a famous experiment by Willis Lamb and Robert Retherford in 1947 where they discovered an energy difference of 1 GHz between the $2^2S_{1/2}$ and $2^2P_{1/2}$ quantum states in atomic hydrogen [4, 5]. This so called "Lamb shift" could not be explained by the relativistic version of quantum mechanics as proposed by Dirac. Instead it required a new mathematical framework and the incorporation of electrodynamics into a new model now known as quantum electrodynamics theory or QED [6, 7]. Predictions from QED included new physical phenomena such as the self

energy of an electron and vacuum polarization. These contributions to the energy are based on the possibility for an electron to emit and absorb a virtual photon, without violating conservation laws if the process happens during a sufficiently short period of time. Similarly, a pair of an electron and a positron can be created, which align themselves with the nuclear charge during their short lifetime. Both these effects become manifest as a small shift in the electronic energy levels, and provides the explanation of the observed Lamb shift. The calculation of level energies in QED theory is based on a series expansion in terms of the fine structure constant α . By including higher order terms, increasingly more complex processes are involved, even though there is no definite reason to assume that the series eventually converges [8]. It therefore always remains the question if a higher order will make a significant contribution and improvement to the level energy. In the early days of QED another inconsistency between quantum theory and experiment surfaced, which was the incorrect prediction of the magnetic moment of the electron [9–11]. Also this deviation was quickly shown to be explained by higher-order QED calculations [12, 13], thereby solidifying the validity of the theory.

In the years after the discovery of the Lamb shift, spectroscopy on the $1S - 2S$ transition (and other transitions in atomic hydrogen) formed the foundation of QED tests in bound systems [14]. The mutual stimulation between experiment and theory has resulted in the fact that today QED is arguably the best tested theory in physics and a corner stone of the Standard Model.

The success of the theory is also nicely illustrated by the calculation of QED effects up to tenth order resulting in an anomalous magnetic moment with an astonishing precision of nine significant digits [15]. This level of accuracy is matched on the experimental side and together lead to a determination of a considerably improved fine-structure constant [16]. Moreover, independent determinations of the fine-structure constant are in agreement with each other [16–18], but the most recent measurements based on Bloch oscillations in Cs [19] actually deviates by about 2.5 sigma.

Experimental techniques improved so much that spectroscopic experiments on the hydrogen $1S - 2S$ transition reached a fractional accuracy of 5×10^{-15} [20, 21]. By combining this measurement with results of multiple optical transitions in hydrogen (e.g. $2S - nS$ and $2S - nD$ transitions), physical constants such as Rydberg constant can be determined. Currently, the uncertainty in the proton-charge radius now dominates the theoretical evaluations, limiting the comparison between theory and experiment [14, 22]. Traditionally the proton-charge radius is determined from electron-proton scattering experiments [23, 24]. However, the analysis of these results

is not trivial and is still being heavily debated [25]. Because the experimental accuracy exceeds the theoretical precision, such spectroscopic measurements can be used to determine the proton-charge radius, under the assumption that QED (including polarization effects) is correct and well enough calculated [14]. This procedure led to a value for the proton-charge radius that is in agreement with the evaluation from electron-scattering experiments [26, 27].

The status quo between experiments and theory was disrupted in 2010 when results were published from a spectroscopy experiment based on muonic hydrogen [28], i.e. hydrogen where the electron is replaced by a muon. The muon is about 200 times heavier than the electron and therefore the extent of the wavefunction is much smaller. The finite nuclear size effect scales with the overlap of the electronic wavefunction with the nucleus, which makes the muonic hydrogen a much more sensitive probe (factor 10^6) of the proton-charge radius. Measurements on the 2S-2P transition in muonic hydrogen resulted in a determination of the proton-charge radius that is ten times more accurate compared to results achieved with electronic hydrogen [28, 29]. However, the initially obtained value deviated by more than five standard deviations, which was later reinforced by new measurements that indicated an even bigger difference, of more than 7σ [30, 31]. According to the latest CODATA recommended values [32] the difference between the electronic and muonic hydrogen measurements is 5.6σ (see Fig. 1.1). This discrepancy is called the "proton-charge radius puzzle" and to date there has been no viable explanation for these results [33–35]. In fact, the puzzle was again reinforced by measurements in deuterium where the difference $r^2(d) - r^2(p)$ is in agreement with the electronic- and muonic- atom determinations [36]. However, a very recent measurement on the 2S-4P transition in electronic hydrogen obtained a value for r_p of 0.8335(95) fm, which is in agreement with the muonic r_p value [37]. Then, even more recently, a measurement on the 1S-3S transition in electronic hydrogen was performed from which a value for r_p of 0.877(13) fm was determined¹ [38]. This value is in perfect agreement with the CODATA recommended value, but deviates from the muonic value by 2.8 standard deviations, which would again reinforce the proton radius puzzle.

It is crucial that this conundrum is resolved because it could indicate new physics beyond the Standard Model, much like the discovery of the Lamb shift led to the development of QED. To tackle this problem novel experiments are required to gather information and provide new input for the theoretical efforts. One suggestion for new experiments is to make a similar comparison in singly ionized helium, to complement the experiments on hydrogen with a different nucleus [46, 47]. From a theoretical

¹Because this result is only available at the time of writing on the *arXiv* it is not shown in Fig. 1.1

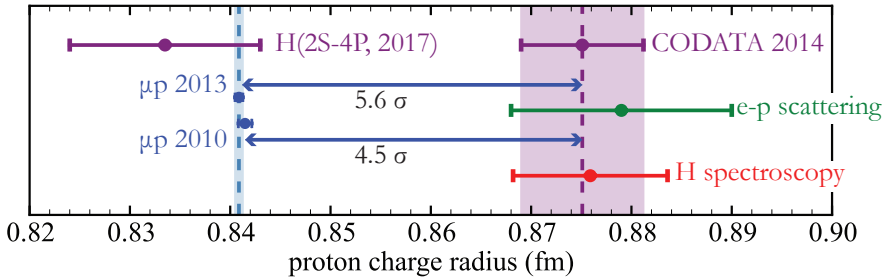


FIGURE 1.1: Overview of the proton radius puzzle. The proton radius extracted from μ -hydrogen [28, 29] is much more accurate than the proton radius extracted from spectroscopy on electronic hydrogen [14, 20, 27, 39–41] and they differ by a combined 4.6 standard deviations (see [32]). The value for extracted from electronic hydrogen spectroscopy is supported by the value extracted from electron proton scattering experiments [42], although there is much debate about the precise interpretation of these measurements [25, 31, 42–45]. The current CODATA recommended value for r_p is based on the scattering data and a selection of measurements in electronic hydrogen [32]. This value differs by 5.6σ from the most precise value extracted from μ H spectroscopy. However, a recent measurement on the 2S-4P transition in electronic hydrogen is in agreement with the muonic value for r_p [37]. The most recent published measurement with electronic hydrogen on the 1S-3S [38] (not shown in the graph) agrees again with the CODATA value.

point of view this system has the benefit of being a two-body system with the added advantage that the charge radius of the alpha particle is known ten times more accurately from scattering experiments compared to the proton charge radius [25]. A measurement on μHe^+ has been conducted, and the evaluation of the results is nearing completion. However, to make a direct comparison possible, spectroscopic measurements on electronic helium are necessary, but that has so far not been demonstrated due to the short wavelength, less than 60 nm, that is required to excite transitions from the ground state [46]. Alternatively, one can look at the squared charge radius difference obtained with muonic $^3\text{He}^+$ and $^4\text{He}^+$, and compare this with the result obtained by spectroscopy in the excited states of electronic helium [48–50]. Another possibility to determine the proton-charge radius is made possible by recent breakthroughs in molecular-QED theory. These now indicate that it will become possible to resolve the proton charge radius from sufficiently accurate spectroscopy of molecular hydrogen [51, 52], the benchmark system for molecular quantum theory and spectroscopy. Also in this system, the required wavelength of ~ 200 nm makes high-resolution spectroscopy difficult.

The motivation for the work presented in this thesis is to investigate the proton-radius puzzle and search for new physics by exploring new methods and systems for

precision spectroscopy that can be compared to theoretical calculations at the highest level. To accomplish this goal we work towards spectroscopy of the 1S-2S transition in singly ionized helium. While doing so, it became apparent that also molecular hydrogen is an interesting candidate for Ramsey-comb excitation to significantly improve the accuracy of the transitions in the X-EF band, and thereby strongly improve future comparisons with theory.

1.2 Ramsey-comb spectroscopy

The improvements in theory since the beginning of the 20th century have been matched by an equal evolution on the experimental side to challenge the calculations. The experimental advancement has led to the development of numerous advanced techniques such as narrow band laser sources, Doppler-free spectroscopy techniques, ion traps, atomic-clocks and Ramsey's method of oscillatory fields, for which numerous Nobel prizes have been awarded. Especially the development of narrowband laser sources sparked a revolution due to the increased resolution that could be obtained. In principle the maximum amount of information that can be extracted from a spectroscopic measurement is predominantly limited by the resolution and the available wavelength range to probe transitions. While the measurement resolution progressed, spectroscopists faced a new problem with the extension from the radio-frequency domain to the optical domain; the optical frequencies were too high to be counted by standard electronic counters (for reviews see e.g. [53, 54]). Therefore a limiting factor in these experiments was the accuracy in the determination of the frequency of the laser light. The definition of the S.I. second is given in terms of the cesium ground state hyperfine splitting of 9 192 631 770 Hz. The gap of several orders of magnitude between the S.I. reference and the optical frequencies of a few hundred THz of the laser light proved to be difficult to bridge [55]. It required a complicated and large setup called a frequency chain which, in addition, could only be used for one particular frequency [55]. This problem was solved far more elegantly in 1999 with the invention of the frequency-comb laser which revolutionized the field of precision spectroscopy [56–58]. In 2005 T.W. Hänsch and J. Hall received the Physics Nobel Prize for their contributions to precision spectroscopy and the invention of the frequency comb laser.

The output of a frequency-comb laser comprises of many (sometimes $> 10^6$) modes that are phase-locked together. The position of each these modes in the spectrum is referenced to a frequency standard such as an atomic clock. This forms a "comb" of modes where each mode can be determined with atomic clock precision. Because

the modes interfere, this translates in the time domain to an infinite train of ultra-short, high peak-intensity phase-locked pulses where the time separation is inversely proportional to the frequency separation of the modes in the spectrum. There have been significant developments of these devices over the past two decades to improve stability, output power and available wavelength range [58].

Due to the available gain materials most frequency combs operate in the infrared and near-infrared part of the spectrum. To enable the proposed experiments in He^+ and H_2 , radiation at much shorter wavelengths is required, where no direct frequency combs exist. One route to create short wavelength radiation is frequency up-conversion through nonlinear optics, such as second-harmonic generation or high-harmonic generation in noble gases [59]. However, the pulse energy of a frequency comb is typically in the nanojoule regime, which is orders of magnitude too low for efficient conversion in nonlinear processes. The pulsed output of the frequency-comb can be amplified to the microjoule regime using full repetition rate amplifiers or enhancement resonators [60–62]. As an alternative route we use selective amplification in a nonlinear parametric amplifier to amplify only two frequency-comb pulses. This method facilitates much higher pulse energies (millijoules) which enables much more efficient nonlinear up-conversion and excitation of weak multi-photon transitions [63]. Spectroscopy with two frequency-comb pulses is similar to, but not quite the same as, a time-domain version of traditional Ramsey spectroscopy [64, 65]. By scanning the time delay between the two excitation pulses Ramsey-fringes can be recorded from which the transition frequency is determined [63]. The effectiveness of this method was demonstrated in 2010 on a transition in neutral helium at 51 nm [66]. The transition was excited using two consecutive amplified and upconverted frequency-comb pulses and resulted in a precision of 6 MHz. Although this was a world record in this wavelength region, the accuracy of the method was limited by the maximum pulse delay, and suffered from spurious phase effects in the amplification process and subsequent high-harmonic generation. To overcome these limitations and reach even higher accuracy the method was extended to the "Ramsey-comb" spectroscopy technique which is introduced in the next paragraph [67].

In the Ramsey-comb method the limitation of pulse delay and phase shifts are circumvented by selecting and amplifying frequency-comb pulse pairs at different multiples of the original repetition time of the frequency-comb. It creates the ability to record multiple Ramsey fringes at different time delays. This extension of Ramsey's method has several important consequences. First of all, the accuracy of the method is greatly enhanced because the pulse delay can be increased, in principle only limited by the lifetime of the excited state [67]. Secondly, a phase shift that affects all Ramsey

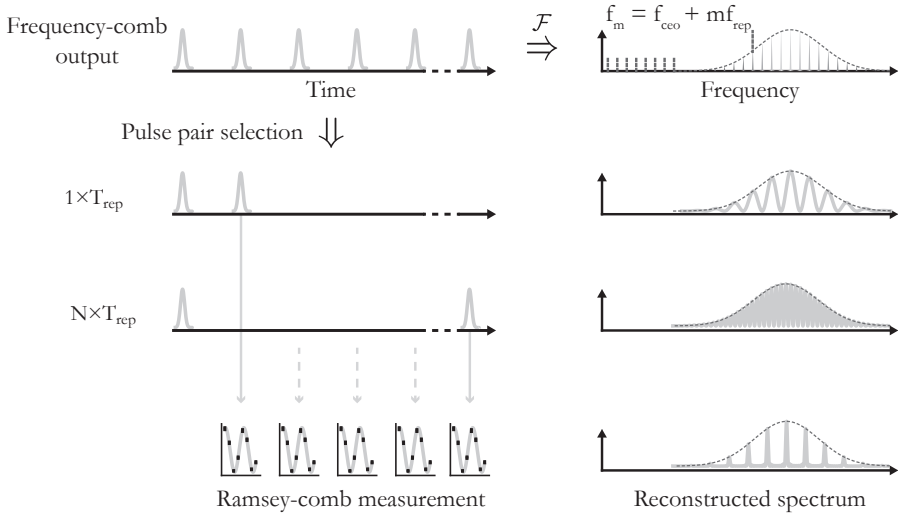


FIGURE 1.2: Schematic overview of Ramsey-comb spectroscopy based on frequency-comb pulses. At the top of the figure the pulsed output of a frequency comb laser is shown together with its spectrum (with a direct Fourier relation between the two). The spectrum is broad, but consists of many narrow modes forming a "comb"-like structure. In Ramsey-comb spectroscopy a pair of pulses is selected to perform a Ramsey-type measurement. The spectrum of a pulse pair is similar to the original spectrum, but instead of narrow modes it has a sinusoidal modulation. By selecting pulse pairs at different time delays (or different modulation frequency in the frequency domain) multiple Ramsey fringes can be measured at different delay times. Combining these measurements results in a "reconstructed" frequency-comb spectrum (in this case of a single transition) and highly accurate spectroscopy.

signals in the same way does not influence the transition frequency determination, in contrast to traditional Ramsey-spectroscopy where phase shifts lead to frequency errors. This is a particular important feature because such phase shifts are e.g. induced by the optical pulses that are used to excite the transition. This is not a problem if frequency-comb pulses are used, but the well defined phase relation of the original frequency-comb pulses is easily distorted by the amplification and up-conversion process. In addition, the method is also insensitive to the AC-Stark shift induced in the atoms of molecules by the intensity of the laser pulses themselves. Because the light shift leads to a constant phase shift of the Ramsey signals, provided the excitation pulse energy stays constant; therefore it is also simply eliminated by the analysis procedure [68]. A final consequence of the Ramsey-comb method is that multiple transitions can be excited simultaneously and resolved by evaluating the phase of the Ramsey signals from the different delay times. A recording of multiple Ramsey signals

in combination with analysis based on the phase of the multiple Ramsey-fringes together is called a Ramsey-comb measurement. The features mentioned before enable ultra-high precision spectroscopy, restoring the spectral resolution that was initially lost by using only two frequency-comb pulses. The method was initially demonstrated in the infrared at 780 nm on rubidium and cesium atoms (see [67]). The combination with mJ pulse energies results in a unique measurement system that can be used for many other spectroscopic targets.

My thesis is based on extending Ramsey-comb spectroscopy to the deep ultraviolet range of the spectrum with a demonstration in krypton and molecular hydrogen, with the prospect of eventually measuring the 1S-2S transition in singly-ionized helium.

1.3 Outline of this thesis

This thesis is organized as follows: it starts in Chapter 2 with the discussion of the key concepts of the Ramsey-comb measurements. In Chapter 3 the experimental setup is presented in detail, with an particular emphasis on the issue of the influence of the amplification process on the optical phase of the frequency-comb pulses that can potentially lead to a frequency shift. In Chapter 4 we present the first Ramsey-comb experiment at deep-ultraviolet wavelengths in krypton and demonstrate a more than an order of magnitude improvement over previous measurements. Finally, in Chapter 5 we present a measurement of the $EF\ ^1\Sigma_g^+(v=0, j=1) \leftarrow X\ ^1\Sigma_g^+(v=0, j=1)$ transition in molecular hydrogen at 202 nm with a fractional uncertainty of 2.5×10^{-11} . This is a two orders of magnitude improvement over previous measurements and it presents a major step forward for precision tests of QED with molecular hydrogen. Chapter 5 also contains a short review about the experimental and theoretical developments concerning the determination of the dissociation energy (D_0) of H_2 in which the EF-X transition plays an important role, and the relevance of this for the proton radius puzzle and searches for new physics.

Frequency-comb laser and Ramsey-comb spectroscopy

2

2.1 Introduction

Spectroscopic measurements have played an important role in the development of the theoretical (quantum) description of matter over the past century. To meet the demand for the ever increasing resolution and accuracy, many techniques for e.g. controlling atoms and molecules (like laser cooling), excitation and detection have been developed. One invention that revolutionized the field of frequency metrology is the frequency-comb laser, which provides a phase coherent link between the radio frequency and optical frequency domain, thereby enabling precise measurements of optical frequencies. It also forms the basis for the Ramsey-comb method [69], a novel spectroscopic method related to traditional frequency-comb spectroscopy (see e.g. [20]) and Ramsey's method of separated oscillatory fields [65]. Besides the demand for ever increasing precision, there is also much interest to probe transitions in the deep ultraviolet and beyond, a region of the spectrum inaccessible with standard lasers. To enable spectroscopy in the deep ultraviolet, frequency upconversion techniques based on nonlinear optics have to be used, which forms the next main ingredient for the experiments presented in this thesis. This chapter starts by introducing frequency-combs and the properties of its time and frequency domain representations. The next section discusses some of the basics of nonlinear optics that is applied in the experiments. In the last section the Ramsey-comb method and signal analysis is explained in detail.

2.2 Optical frequency combs

In the year 1999 the field of optical frequency metrology was revolutionized by the invention of the frequency-comb laser [56, 70]. Until that time measurements were hampered by the 10^5 frequency ratio between the optical domain and the microwave transition at 9.2 GHz in Cs on which the SI second is based¹, which could only be bridged by elaborate frequency chains [55]. With frequency comb lasers precise frequency determinations in the whole optical domain were possible [57, 71] with much

¹The second is defined by the energy splitting between the two hyperfine levels of the ground state of the $^{133}\text{cesium}$ atom, corresponding to 9 192 631 770 oscillation periods of radiation

less effort, which also almost immediately resulted in an order of magnitude improvement in measurement accuracy [39, 58, 72]. In a very short period of time this technology was further developed to cover a larger wavelength range including the mid and far infrared [73, 74], the THz regime [75] and later to the the deep UV, VUV and XUV spectral range [76–80]. Besides the application related to frequency metrology, frequency combs have been used for precise distance measurement [81] and cooling of atoms and molecules [82, 83]. Also, frequency combs can assist in a practical application of a time (frequency) standard based on optical transitions instead of microwave transitions, which can potentially lead to a more accurate and stable definition of the SI second [84–86]. Because frequency-comb technology provides control over the phase evolution of the pulse train, it also opened the door for applications in attosecond science [59].

The fundamental properties of a frequency-comb laser can be described in both the time domain and the frequency domain, which are related to each other through basic Fourier transforms. To understand how frequency combs can be utilized for precision spectroscopy and Ramsey-comb spectroscopy it is important to understand the characteristics in both domains and their intimate connection. This section is devoted to describing the basic principles of a frequency-comb laser.

2.2.1 The frequency-comb laser

Frequency-combs are based on mode-locked lasers, a technique that was already developed in the early seventies of the last century [87, 88]. Mode-locking refers to establishing a fixed phase relation between the longitudinal modes of a laser cavity over a large range of frequencies [89]. In practice this is the result of a nonlinear mechanism that results in higher net gain for short pulses compared to continuous-wave lasing. The mode-locking mechanism can either be an active element or be established passively by some means of saturable absorption or Kerr-lensing. Passive mode locking generally yields shorter pulses because the self adjusting mechanism becomes more efficient if the pulse becomes shorter (up to a certain limit [90]). An example of passive mode locking is based on a cavity with a semiconductor saturable absorber mirror (SESAM) that provides higher losses for lower intensities (see [91] for operation principle). Although this type of mode-locking does not generate the shortest pulses possible, it is a robust and fairly easy way to realize picosecond pulses. This technique is used in this thesis for the generation of 1064 nm picosecond pulses (see Chapter 3).

Another particular type of mode-locked laser that has been intensively studied is the Kerr-lens mode-locked Ti:sapphire laser. The main reason that this material has become so popular is the wide gain bandwidth which enables it to support ultra-short

pulses. Based on this material pulses of only 6 fs duration have been demonstrated, which is equivalent to a duration of less than two optical cycles [92–94]. In addition, Ti:sapphire also provides the mode-locking mechanism (Kerr-lensing), making them relatively easy to operate, build and control. The limit in pulse duration of this type of mode locking is an interplay between the mode-locking mechanism, the group velocity dispersion and the net gain bandwidth [95].

To be able to utilize these devices for precise frequency metrology purposes it is important to understand the connection between the time and frequency domain representation. A simple model to describe the time-domain output of a mode-locked laser is that of a laser pulse circulating inside the cavity (for detailed textbook discussions see [71, 91, 96]). Each time the laser pulse imparts on the output coupler a pulse is emitted by the cavity, where the shape and characteristics of the pulse are determined by the interaction with the elements inside the cavity. The time between the pulses is determined by the optical path length in the cavity and the group velocity, resulting in a train of laser pulses separated by the repetition time T_{rep} . Dispersion inside the cavity leads to a group velocity that is not equal to the phase velocity, giving rise to the before mentioned carrier-envelope offset phase according to

$$\Delta\phi_{ceo} = \left(\frac{1}{v_g} - \frac{1}{v_p} \right) l_c \omega_c \quad (2.1)$$

where v_g and v_p are the effective group and phase velocity, respectively, and l_c is the effective interaction length in the cavity, and ω_c is the carrier frequency. This pulse-to-pulse phase slip with respect to the pulse envelope has an important consequence for the structure of the spectrum.

The spectrum of a single pulse emitted by a mode-locked laser is simply the Fourier transform of its envelope function centered around the carrier frequency. Neglecting the carrier-envelope phase shift for a moment, then the spectrum of a train of identical pulses consists of an infinitely long equidistant set of frequencies that are separated by the inverse of the pulse repetition time, forming a 'comb' like structure. However, since the carrier-envelope phase shift is not generally equal to zero, the influence of the $\Delta\phi_{ceo}$ on the spectrum has to be carefully considered. In the time-domain the electric field for a train of pulses can be described by [71]

$$E_{train}(t) = \sum_{n=0}^{N-1} \hat{E}(t - nT_{rep}) e^{i(\omega_c t - n\omega_c T_{rep} + n\Delta\phi_{ceo})} \quad (2.2)$$

where $\hat{E}(t)$ is the (complex) envelope of a single pulse and N is the total number of pulses. Assuming that the pulses are identical throughout the entire pulse train and

T_{rep} is constant, then the spectrum of a pulse train can be obtained by a Fourier integral

$$E_{train}(\omega) = \int \sum_{n=0}^{N-1} \hat{E}(t - nT_{rep}) e^{i(\omega_c t - n\omega_c T_{rep} + n\Delta\phi_{ceo})} e^{-i\omega t} dt \quad (2.3)$$

This equation can be written in simpler form using the integral identity $\int f(x - \alpha) e^{-i\beta x} dx = e^{-i\alpha\beta} \int f(x) e^{-i\beta x} dx$ leading to

$$E_{train}(\omega) = \int \hat{E}(t) e^{-i(\omega - \omega_c)t} dt \sum_{n=0}^{N-1} e^{in(\Delta\phi_{ceo} - \omega_c T_{rep})} e^{-in(\omega - \omega_c)T_{rep}} \quad (2.4)$$

Before the summation sign we recognize the Fourier relationship between the pulse temporal and spectral envelope centered around the carrier frequency. Using this and rewriting the terms after the summation results in

$$E_{train}(\omega) = \tilde{E}(\omega - \omega_c) \sum_{n=0}^{N-1} e^{in(\Delta\phi_{ceo} - \omega T_{rep})} \quad (2.5)$$

The components that contribute to the spectrum are those for which the exponentials in the sum add up coherently. The frequencies for which this is satisfied require a phase between the consecutive pulses that is an integer multiple of 2π , which is equivalent to $\Delta\phi_{ceo} - \omega T_{rep} = n2\pi$. The frequencies in the spectrum can thus be written as

$$\omega_n = \frac{\Delta\phi_{ceo}}{T_{rep}} + \frac{n2\pi}{T_{rep}} \quad (2.6)$$

Converting from angular frequency to 'normal' frequency ($f = 2\pi\omega$) and introducing the definitions for the repetition frequency $f_{rep} = 1/T_{rep}$ and carrier-envelope offset frequency $f_{ceo} = (\Delta\phi_{ceo}/2\pi)f_{rep}$ this equation can be written in the form of a simple formula

$$f_n = f_{ceo} + nf_{rep} \quad (2.7)$$

This is a well known equation that describes the time-averaged frequency domain output and applies to all mode-locked lasers, and the distinction with a true frequency-comb laser has yet to be made.

In Fig. 2.1 a schematic overview of the output of a mode locked laser in time domain with the corresponding spectrum is given. The pulsed output corresponds to a spectrum that comprises of many narrow modes where each frequency component is separated from the previous by the repetition frequency according to Eq. 2.7. Also according to Eq. 2.7 all the modes are shifted by the carrier envelope offset frequency

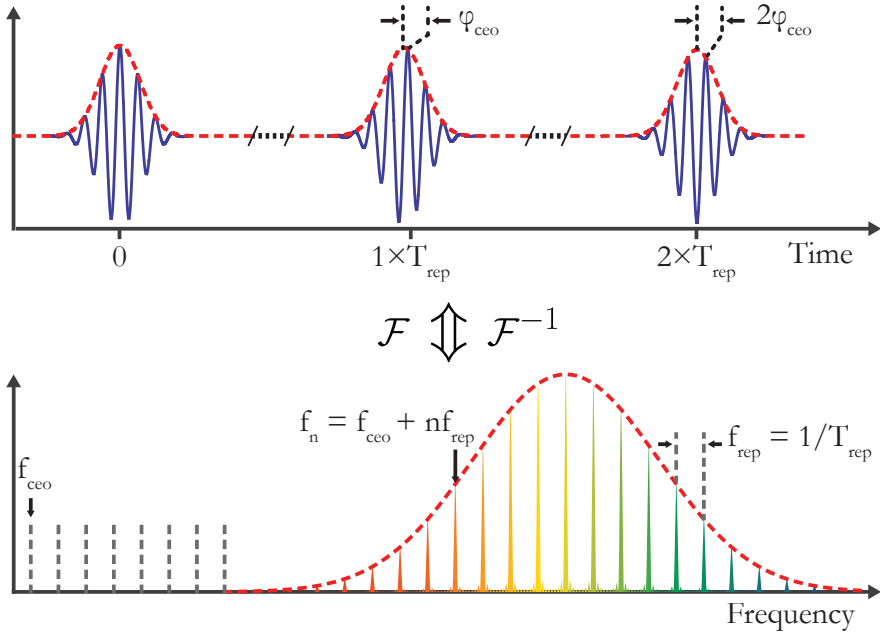


FIGURE 2.1: Illustration of the Fourier relation between the time and frequency domain of a mode-locked laser. An infinite train of ultrashort pulses that are equally spaced in time by the repetition rate T_{rep} corresponds to a comb of frequencies separated by the inverse of the repetition time, i.e. $f_{rep} = 1/T_{rep}$. A pulse-to-pulse phase shift ($\Delta\phi_{ceo}$) in the time domain, caused by a difference between the group and phase velocity, shifts all the comb lines by an amount of $f_{ceo} = (\Delta\phi_{ceo}/2\pi)f_{rep}$. When both the repetition frequency and offset frequency are stabilized to a frequency standard these devices are called frequency-combs.

(f_{ceo}) which is related to the pulse-to-pulse phase shift. So the position of all the frequencies in the spectrum is completely determined by just those two parameters, f_{rep} and f_{ceo} . What is interesting is that these two parameters are typically in the radio frequency domain whereas these lasers typically operate at optical frequencies of several hundred THz. If both f_{rep} and f_{ceo} can be measured and stabilized to a frequency standard, then these devices could be used as a phase-link between radio frequency and optical frequency domains where direct frequency measurements were previously very difficult. Concerning control over the repetition rate, this is a relatively straightforward task and can be achieved by adjusting the cavity length using e.g. piezo electric transducers (see also Section 3.2). The value of f_{rep} can simply be determined using a counter and a photodiode to measure the pulsed output. Measuring the f_{ceo} turned out to be a bigger challenge since a direct measurement is impossible due to the absence of spectral intensity at that frequency (see Fig. 2.1) and the invention of the f:2f nonlinear interferometer [57, 71]. This problem was solved in 1999 with the

introduction of nonlinear optic fibers, which allowed generation of octave spanning optical spectra with unamplified pulses from a mode-locked laser (see Section 3.2 for more detail). The term frequency-comb is (usually) reserved for a mode-locked laser that has the parameters f_{rep} and f_{ceo} measured and referenced to a primary time standard, such as a cesium atomic clock. This may seem like a small improvement over normal modelocked lasers, but controlling the large number of frequencies of the comb spectrum has led to numerous new possibilities and applications especially in frequency metrology.

2.2.2 Spectrum of two frequency-comb pulses

For the purpose of this thesis it is instructive to evaluate the spectrum of two pulses in a little more detail. If (for simplicity) we assume a Gaussian pulse envelope with FWHM duration of $\tau_t = 2\sqrt{2\ln(2)}\tau_0$ in the time domain, Eq. 2.2 can be transformed to ²

$$E_{train}(\omega) = E_o(\omega) \frac{1 - e^{iN(\Delta\phi_{ceo} - \omega T_{rep})}}{1 - e^{i(\Delta\phi_{ceo} - \omega T_{rep})}} \quad (2.9)$$

where $E_o(\omega) = \exp\left(-\frac{\tau_0^2(\omega - \omega_c)^2}{2}\right)$ is the spectrum of a single pulse with FWHM $\Delta\omega = 2\sqrt{2\ln(2)}/\tau_0$. The spectral intensity is given by the square of the electric field, resulting in

$$I(\omega) = |E(\omega)|^2 = I_o(\omega) \frac{\sin^2(N(\omega T_{rep} + \Delta\phi_{ceo})/2)}{\sin^2((\omega T_{rep} + \Delta\phi_{ceo})/2)} \quad (2.10)$$

For only two pulses $N = 2$, and this equation reduces to

$$I(\omega) = 4I_o(\omega) \cos^2\left(\frac{\omega T_{rep} + \Delta\phi_{ceo}}{2}\right) \quad (2.11)$$

This equation shows that for two pulses the spectrum is the original spectrum of a single pulse modulated with a cosine shaped amplitude. The period of the oscillation is inversely proportional to the time separation between the two laser pulses, as is graphically depicted in Fig. 2.2. The top two graphs in this figure show the sequences of two pulses separated by T_{rep} and $4 \times T_{rep}$ respectively. The corresponding spectra, that are plotted on the right, show that for the second pulse sequence the mode spacing is 4 times smaller, and therefore the resolution 4 times higher. In Fig. 1.2 it

²Using the solution of a standard series

$$\sum_{n=0}^{N-1} x^n = \frac{1 - x^N}{1 - x} \quad (2.8)$$

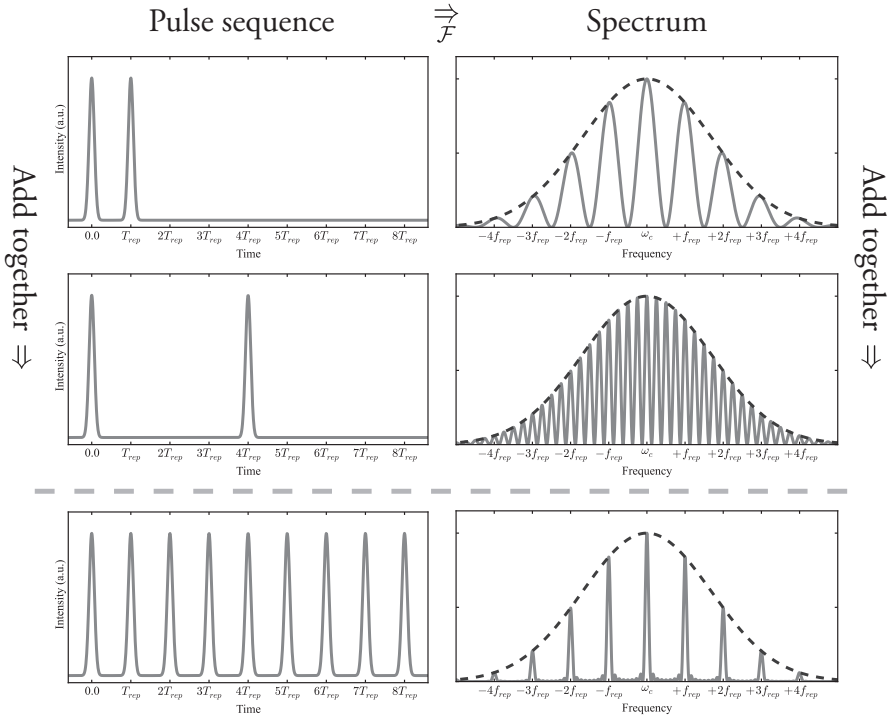


FIGURE 2.2: On the left side the temporal intensity of pulse sequences of two pulses is plotted with on the right the corresponding spectra. The single pulse spectrum determines the envelope (the dashed line) intensity of the spectrum and for two pulses the spectrum is cosine modulated with a fringe period that is inversely proportional to the repetition time. More pulses lead to sharper features, so that eventually for an infinite pulse train the frequency comb spectrum as depicted in Fig. 2.1 is recovered.

was shown graphically that a combination of several measurements at different pulse delays can recover the original information of the frequency comb, despite the fact that the spectrum of each two-pulse sequence looks like a cosine modulated continuum. In the bottom part of Fig. 2.2 an intermediate case between 2 pulses and full repetition rate is shown. The resulting spectrum starts to resemble a frequency comb much more and in the limit of an infinite pulse train, the full (narrow mode) spectrum of a frequency comb (Fig. 2.1) is recovered.

2.2.3 Spectroscopy with frequency combs

The development of the frequency-comb laser is rooted in the field of precision spectroscopy where the first ideas to use mode-locked lasers were already formed in the 1970s [88]. With the development of the self-referenced frequency-comb laser it has

become possible to measure the frequency of a narrow band continuous wave (cw) laser source by observing the beat note frequency between the cw laser and one of the comb teeth. By tuning the narrowband laser over a resonance and monitoring the beat, frequency the obtained spectrum could be calibrated with high precision. However, in this process it is still necessary to determine the correct mode number m for the absolute frequency calibration. This can be obtained straightforwardly if the resonance is known with sufficient accuracy, i.e. if it is known more precise than the repetition frequency of the frequency-comb laser. If this is not the case the correct mode can be assigned by repeating the measurement at different repetition frequencies and observing where all the frequency determinations coincide. This is the most 'traditional' use of frequency-combs in high resolution spectroscopic experiments.

Instead of using the frequency-comb laser as a kind of ruler and measure the frequency of a spectroscopy laser, it is also possible to use the frequency-comb pulses to directly excite atomic or molecular resonances. Although the traditional method has resulted in unprecedented measurement accuracy [20] it also requires an additional (possibly expensive) ultra-stable spectroscopy laser. Especially in the deep ultraviolet (and shorter wavelengths) these type of lasers are difficult to obtain or simply not available, and other techniques are required. One approach to this problem is based on direct excitation with comb pulses that are up-converted through nonlinear processes.

Direct frequency-comb spectroscopy is performed by exciting a resonance and scanning the comb spectrum over the resonance. Control of f_{rep} and f_{ceo} gives the ability to accurately scan the modes of the frequency comb laser. In such a measurement the obtained spectrum is a convolution of the atomic or molecular response with the spectrum of the frequency-comb, which can lead to complicated spectra if multiple transitions are excited by different comb modes. Similar as in the generic application of frequency comb lasers in spectroscopy, the resonances can be identified if they are known with sufficient accuracy beforehand. If this is not the case then (again) this ambiguity can be solved by repeating the measurement at different repetition rates. Excitation with comb pulses directly offers several advantages. One notable benefit is the peak power of the frequency-comb pulses which can be further enhanced to obtain much higher peak power than is feasible with continuous wave lasers. This opens up the possibility to frequency up-convert the comb pulses to the (extreme) ultraviolet in nonlinear processes which are not efficient enough at the power levels of cw lasers. These pulses can then be used to perform high-precision metrology measurements at extreme wavelengths, provided that the amplification and non-linear conversion do not compromise the phase coherence of the pulses [62, 66].

The experiments in this thesis are based on exciting resonances in the deep ultraviolet with a pair of amplified and frequency up-converted comb pulses. The basics of the nonlinear processes involved can be found in Section 2.3 and the response of an atom to a pair of frequency-comb pulses (which resembles a Ramsey-type experiment) is detailed in Section 2.4.

2.3 Frequency upconversion and parametric amplification

One of the great things about pulsed lasers is that all their energy is concentrated into a (very) short period of time. The laser pulses from e.g an oscillator based on Ti:sapphire have an energy of roughly 10 nanojoule, and can easily be made shorter than 10 fs, which results in a peak power of 1×10^6 Watts. Moreover, these pulses can be focused to a spot size on the order of 1×10^{-8} m² leading to a peak intensity of 1×10^{10} W/cm². Although this peak intensity in the focus is already quite high, the total flux is still relatively low and in some cases insufficient to perform experiments. However, over the past two decades the technology has been developed to amplify such pulses up to the millijoule regime, making it feasible to obtain pulses with several terrawatt peak power [97]. When such laser pulses are focused and propagate through media, high-intensity effects (or non-linear effects) occur that can ordinarily not be observed. In linear optics, light beams pass through optical materials without affecting each other, in the non-linear regime this is no longer the case. Under the right circumstances these effects can be exploited to, for example, create new frequencies using second-harmonic generation. When such intense fields (typically 1×10^{12} W/cm²) propagate through a medium the electrons in that medium become displaced due to the electric field of the optical wave, inducing a polarization. This polarization can act as a source term emitting these new frequencies which is described by the well known wave equation

$$\nabla^2 E(\mathbf{r}, t) - \left(\frac{n}{c}\right)^2 \frac{\partial^2 E(\mathbf{r}, t)}{\partial t^2} = \mu_0 \frac{\partial^2 P(\mathbf{r}, t)}{\partial t^2} \quad (2.12)$$

where c is the speed of light inside the medium, n is the refractive index of the medium, μ_0 is the magnetic permeability of free space and E and P are the real electric field of the light and the induced polarization. The induced polarization contains the effects of the light on the medium and vice-versa, it is what drives the wave equation and contains both linear-optical effects and non-linear optical effects.

At low field intensities only linear optical effects, such as absorption and normal refractive index, can be observed. The induced polarization is proportional to the

applied electric field (of the laser) and can be written as

$$P(\mathbf{r}, t) = \epsilon_0 \chi^{(1)} E(\mathbf{r}, t) \quad (2.13)$$

where ϵ_0 is the permittivity of free space and the linear susceptibility $\chi^{(1)}$ describes the linear optical effects. If a lossless medium is assumed, then the solution for the electric field and polarization is given by $E = E_0 \cos(\omega t - \mathbf{k} \cdot \mathbf{r})$ and $P = \epsilon_0 \chi^{(1)} E_0 \cos(\omega t - \mathbf{k} \cdot \mathbf{r})$ provided that $\omega = ck$ and $c = c_0 / \sqrt{1 + \chi^{(1)}}$. Because in linear optics the wave equation is linear, P drives the wave equation to produce light only with the frequencies that are originally present in E , i.e. no additional frequencies are created. However, at high-field intensities the induced polarization is no longer a simple linear function of the electric field and more interesting things can happen. In this case the polarization can be written as

$$P(z, t) = \epsilon_0 \left(\chi^{(1)} \mathbf{E} + \chi^{(2)} \mathbf{E}^2(z, t) + \chi^{(3)} \mathbf{E}^3(z, t) + \dots \right) \quad (2.14)$$

where $\chi^{(n)}$ is the n^{th} order susceptibility which is a tensor of rank $n + 1$. The second-order nonlinear optical effects can be calculated using the description of an optical pulse where an envelope function is superimposed on a continuous carrier wave; $E(t) = \frac{1}{2} \widehat{E}(t) e^{i\omega_c t} + cc$. Here the spatial dependence is omitted, and squaring the electric field gives

$$E^2(t) = \frac{1}{4} \widehat{E}^2(t) e^{i2\omega_c t} + \frac{1}{2} \widehat{E}(t) \widehat{E}^*(t) + \frac{1}{4} \widehat{E}^{*2}(t) e^{-i2\omega_c t} \quad (2.15)$$

This expression includes terms that oscillate at $2\omega_c$, the second harmonic of the input frequency, and a DC component due to optical rectification. It is also possible to have more than one input beam, possibly at different frequencies, angles, and polarizations, which can lead to many different processes and output beams. Suppose the electric field of two pulses is given by

$$E(\mathbf{r}, t) = \frac{1}{2} \widehat{E}_1 e^{i(\omega_1 t - \mathbf{k}_1 \cdot \mathbf{r})} + \frac{1}{2} \widehat{E}_2 e^{i(\omega_2 t - \mathbf{k}_2 \cdot \mathbf{r})} + cc \quad (2.16)$$

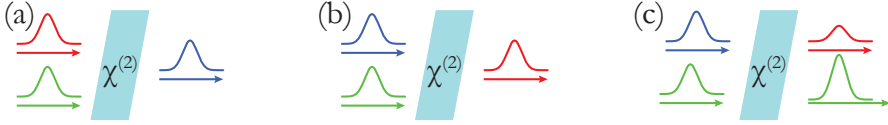


FIGURE 2.3: Simple graphical models of second-order non-linear effects: (a) sum-frequency generation (b) difference-frequency generation and (c) parametric amplification.

where the time and space dependence of the complex field amplitudes is omitted for readability. Squaring this field results in

$$\begin{aligned}
 E^2(\mathbf{r}, t) = & \frac{1}{4} \widehat{E}_1^2 e^{2i(\omega_1 t - \mathbf{k}_1 \cdot \mathbf{r})} + \frac{1}{4} \widehat{E}_1^{*2} e^{-2i(\omega_1 t - \mathbf{k}_1 \cdot \mathbf{r})} + \frac{1}{2} \widehat{E}_1 \widehat{E}_1^* \\
 & + \frac{1}{4} \widehat{E}_2^2 e^{2i(\omega_2 t - \mathbf{k}_2 \cdot \mathbf{r})} + \frac{1}{4} \widehat{E}_2^{*2} e^{-2i(\omega_2 t - \mathbf{k}_2 \cdot \mathbf{r})} + \frac{1}{2} \widehat{E}_2 \widehat{E}_2^* \\
 & + \frac{1}{2} \widehat{E}_1 \widehat{E}_2 e^{i((\omega_1 + \omega_2)t - (\mathbf{k}_1 + \mathbf{k}_2) \cdot \mathbf{r})} \\
 & + \frac{1}{2} \widehat{E}_1^* \widehat{E}_2^* e^{-i((\omega_1 + \omega_2)t - (\mathbf{k}_1 + \mathbf{k}_2) \cdot \mathbf{r})} \\
 & + \frac{1}{2} \widehat{E}_1 \widehat{E}_2^* e^{i((\omega_1 - \omega_2)t - (\mathbf{k}_1 - \mathbf{k}_2) \cdot \mathbf{r})} \\
 & + \frac{1}{2} \widehat{E}_1^* \widehat{E}_2 e^{-i((\omega_1 - \omega_2)t - (\mathbf{k}_1 - \mathbf{k}_2) \cdot \mathbf{r})}
 \end{aligned} \tag{2.17}$$

The first two lines of this result are equal to Eq. 2.15, they describe the second harmonic and optical rectification terms for the individual fields. The next lines show two new components at $\omega_1 + \omega_2$ and $\omega_1 - \omega_2$ called sum-frequency generation and difference-frequency generation respectively, and can be generated in new directions. Besides sum and difference frequency generation it is also possible for a single pulse of frequency ω_3 to split up in such a way that $\omega_3 = \omega_1 + \omega_2$. This process, that also relies on the second-order polarization term, is called parametric oscillation (or amplification if ω_1 or ω_2 is present also at the input side). These second-order nonlinear effects are graphically depicted in Fig. 2.3.

In the most complete case, i.e. for the interaction of three optical fields, the behavior is described by a set of three coupled differential equations

$$\frac{\partial \widehat{E}_1}{\partial r} + k_1' \frac{\partial \widehat{E}_1}{\partial t} - \frac{i}{2} k_1'' \frac{\partial^2 \widehat{E}_1}{\partial t^2} = -i \chi^{(2)} \frac{\omega_1}{2n_1 c} \widehat{E}_3 \widehat{E}_2^* e^{-i \Delta \mathbf{k} \cdot \mathbf{r}} \tag{2.18a}$$

$$\frac{\partial \widehat{E}_2}{\partial r} + k_2' \frac{\partial \widehat{E}_2}{\partial t} - \frac{i}{2} k_2'' \frac{\partial^2 \widehat{E}_2}{\partial t^2} = -i \chi^{(2)} \frac{\omega_2}{2n_2 c} \widehat{E}_3 \widehat{E}_1^* e^{-i \Delta \mathbf{k} \cdot \mathbf{r}} \tag{2.18b}$$

$$\frac{\partial \widehat{E}_3}{\partial r} + k_3' \frac{\partial \widehat{E}_3}{\partial t} - \frac{i}{2} k_3'' \frac{\partial^2 \widehat{E}_3}{\partial t^2} = -i \chi^{(2)} \frac{\omega_3}{2n_3 c} \widehat{E}_1 \widehat{E}_2 e^{i \Delta \mathbf{k} \cdot \mathbf{r}} \tag{2.18c}$$

where $\Delta \mathbf{k} = \mathbf{k}_3 - \mathbf{k}_1 - \mathbf{k}_2$. This set describes second-order optical effects such as sum-frequency generation and parametric amplification. Which one occurs depends on the exact realization of the phase matching condition ($\Delta = 0$), which will be explained in a bit more detail later in this section. An analytic evaluation of these equations is mathematically challenging, however, in certain cases simplifications can be made to gain insight into some of the processes.

The problem can be made simpler by considering only the second-order nonlinear polarization. Assuming the following conditions; an input pulse with a small bandwidth that is centered around ω_0 , nonlinear effects are weak and hardly deplete the fundamental field, only one signal field is considered, the field envelope of the light pulse is varying slowly compared to the carrier frequency, uniform beams and no diffraction, the electric field and the polarization have the same k -vector. Especially this last condition is usually not satisfied and needs to be taken care of. Nonetheless, under these conditions the wave equation reduces to (omitting the time and position dependence and assuming a wave traveling in the z direction)

$$\frac{\partial \hat{E}}{\partial z} = -i \frac{\mu_0 \omega_0^2}{2k_0} \hat{P} \Rightarrow \hat{E} = -i \frac{\mu_0 \omega_0^2}{2k_0} \hat{P} z \quad (2.19)$$

This shows that the new field grows linearly with the propagation distance which means that the intensity grows quadratically with distance. However, the generated wave is usually at a completely different frequency and therefore sees a different refractive index and as a result travels at a different phase velocity. The generated wave will therefore move out of phase with the induced polarization and interfere destructively with the new light that is created. To avoid this from happening the generated light and the induced polarization need to have the same phase velocity, so they are *phase matched*. To account for this effect we introduce a different k -vector for the induced polarization, k_p , which leads to an expression for the intensity after propagating a distance L through the medium of

$$I(L, t) = \frac{c \mu_0 \omega_0^2}{4} |\hat{P}|^2 L^2 \text{sinc}^2(\Delta \mathbf{k} L / 2) \quad (2.20)$$

where $\Delta \mathbf{k} = k_0 - k_p$. The sinc function has a maximum for $\Delta \mathbf{k} = 0$ so that optimal nonlinear efficiency is maximized when the induced polarization and the light it creates are in phase throughout the medium, i.e. phase matched. For the case of second-harmonic generation the phase matching condition becomes $k_2 = 2k_1$ which can be reduced to $n(\omega_1) = n(2\omega_1)$. Most materials have dispersion and will therefore have significant phase mismatch, so that over a very short distance (typically micrometers)

a significant phase difference is accumulated, leading to a low conversion efficiency. It is possible to achieve phase-matching over much longer interaction lengths using birefringent crystals. One such a crystal is β -barium-borate (BBO) which has a high $\chi^{(2)}$ coefficient and is now commonly used for efficient second-harmonic generation and parametric processes. The experiments presented in this thesis rely on the use of this type of crystal for the generation of deep ultraviolet radiation.

Besides frequency upconversion these crystals are also used for a process called parametric amplification. In parametric amplification a 'pump' photon is split in a lower frequency 'signal' photon and an even lower frequency 'idler' photon, as described earlier in this section. The indices for the beams in Eq. 2.18 are usually taken as p , s , and i instead of 1, 2 and 3. To calculate the effects of parametric amplification, in which three beams interact, the full coupled differential equations (Eq. 2.18) need to be solved. However a few conclusions can already be drawn without resorting to difficult calculations. The first is again that the phase-matching condition should be satisfied, i.e. $k_p = k_s + k_i$, for optimal efficiency. Also the efficiency of the energy transfer depends strongly on the respective intensities of the beams. Moreover, it can be shown that in the absence of dispersion (or for broad bandwidth phase matching) the small signal gain factor scales exponentially with the propagation length. It is thus feasible to obtain a gain of 10^4 with only a few mm propagation through a nonlinear crystal with a high $\chi^{(2)}$ such as BBO [98].

2.4 Ramsey-comb spectroscopy with frequency-comb pulse pairs

The techniques described in the previous sections are combined and used to perform *Ramsey-comb spectroscopy* experiments at ultraviolet wavelengths. In this section the principle of the excitation method and the frequency determination from experimental results is discussed. As the name Ramsey-comb spectroscopy suggests it is based on a combination of Ramsey's method of oscillatory fields with frequency-comb pulses. In Ramsey's method a quantum absorber, like an atom or molecule, is exposed to an excitation field for two short periods of time, τ . The interactions with the excitation field are separated by period, T_{free} , where no field is present, in contrast to applying a coherent field for the full duration of $\tau + T_{free} + \tau$. The method was originally proposed by N.F. Ramsey for transitions in the microwave regime in a molecular beam experiment. He predicted that the resonance curves would be much sharper, leading to a higher precision measurement [64]. Although the method was originally designed for an atomic beam passing through two spatially separated regions, it can equally

well be applied to atomic or molecular beams or techniques where the absorbers are stationary (e.g. in ion traps) and the interrogation field is switched on and off in a time sequence. Moreover, the signal obtained with Ramsey-spectroscopy is nearly two times narrower than equivalent CW excitation of the same duration, enabling higher resolution measurements. This Ramsey-excitation, or quantum-interference metrology, has proven to be extremely fruitful and is now applied in many laboratories around the world and most notably in cesium atomic clocks and other microwave frequency standards.

In our application of Ramsey's method, the phase evolution of an atom is probed with two frequency-comb pulses that are separated by a time Δt . In Fig. 2.4 a schematic overview is depicted of the time evolution of two resonant laser pulses (top part) interacting with a two-level quantum system (bottom part). The quantum system is described by two eigenstates with energies E_g and E_e , that are separated by an energy interval $\Delta E = E_e - E_g$, and we assume all the population is initially in the ground state. After interacting with the first resonant laser pulse, the quantum absorber is in a superposition of the ground and excited state. This superposition will evolve in time with a phase velocity $\omega_{tr} = 2\pi f_{tr}$ and an initial phase that is determined by the phase of the driving field. This is schematically depicted in Fig. 2.4 by the green trace in the lower part of the figure. Likewise, the second, time delayed, resonant laser pulse adds a superposition amplitude, indicated by the purple trace. For low excitation amplitude, one can say that the two superpositions of states will interfere and depending on the relative phase of the two superpositions the excitation amplitude is either increased or decreased. The probability of finding an atom in the excited state after two such pulses is proportional to the absolute value squared of the resulting amplitude, which is the quantity that can be observed in the measurements. In the case of excitation with two phase-locked pulses the relative phase of the superpositions is determined by the time delay between the excitation pulses and their relative phase. If one has the means of adjusting the time delay of two such pulses with sufficient resolution and accuracy, the quantum interference signal can be probed as function of Δt from which the transition frequency can be determined.

The probability of finding an atom in the excited state after applying a phase coherent pulse pair with time delay Δt is given by (see Appendix A)

$$|c_2|^2 = \frac{A_0}{2} \{1 + \cos(\omega_0 \Delta t - \Delta\phi)\} \quad (2.21)$$

With

$$A_0 = 4 \sin^2(\Omega\tau) \cos^2(\Omega\tau) \quad (2.22)$$

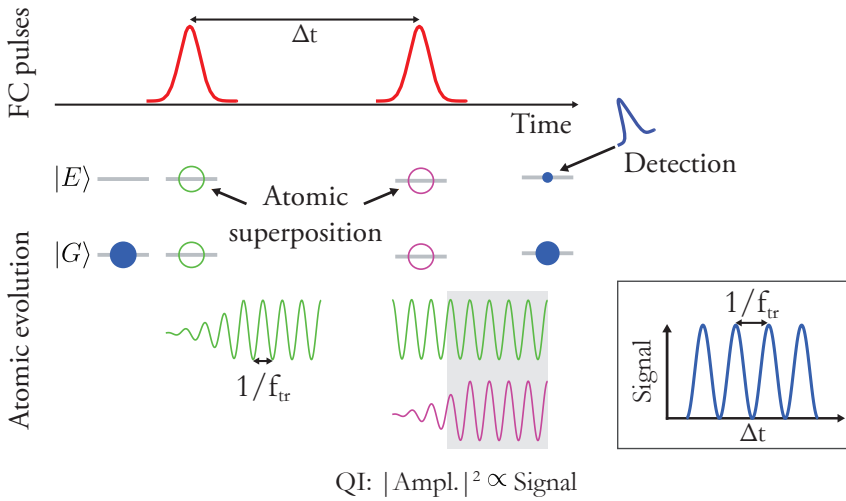


FIGURE 2.4: Principle of quantum interference as a result of interaction two phase locked laser pulses. A two level quantum system that is initially in the ground state is excited by a resonant laser pulse creating a superposition of the ground and excited state. The phase of the superposition is determined by the driving field and will evolve with phase velocity $\omega_{tr} = 2\pi f_{tr} = \Delta E/2\pi\hbar$, where f_{tr} is the transition frequency. In similar fashion, the second time delayed laser pulse also creates a superposition. Quantum interference (QI) between the superpositions of states leads to an enhanced or decreased amplitude depending on the relative phase. The absolute value squared of the amplitude is proportional to the population in the excited state, which can be detected in an experiment. With phase locked pulses the relative phase can be changed by adjusting the delay time Δt between the pulses which results in a sinusoidal signal with a period inversely proportional to the energy difference between the states.

Here τ is the duration of the excitation pulses, Ω is the Rabi frequency which depends on the electric dipole operator and the strength of the electric field (see Appendix A), ω_0 is the angular transition frequency and $\Delta\phi$ incorporates possible phase shifts between the excitation pulses. Eq. 2.21 shows that the excited state population oscillates with the energy difference between the states as function of the delay time Δt . In Ramsey spectroscopy performed with two time delayed phase coherent pulses, typically only a few oscillations of the quantum interference signal can be measured. Nonetheless, based on Eq. 2.21 the transition frequency can be determined provided that all possible phase shifts $\Delta\phi$ are known with sufficiency accuracy and Δt can be controlled accurately. In fact, the uncertainty of the frequency determination is proportional to the uncertainty in the determination for spurious phase shifts ($\delta(\Delta\phi)$), and inversely proportional to the maximum time delay between the pulses that can

be achieved, i.e.

$$\delta(\omega_{tr}) \propto \frac{\delta(\Delta\phi)}{\Delta t} \quad (2.23)$$

This means that for a longer time separation between the excitation pulses the frequency can be determined more accurately, similar to traditional Ramsey spectroscopy. In addition, the measurement becomes less sensitive to any uncertainties in $\Delta\phi$ which can be a limiting factor in these type of measurements. For the experiments discussed in this thesis the phase shift $\Delta\phi$ is of great interest and can be influenced by a number of effects. One notable source of additional phase shift in the Ramsey signal when using frequency-comb pulses for the excitation is the carrier-envelope phase shift $\Delta\phi_{ceo}$. Moreover, the phase of the optical pulses can be modified by for e.g. the parametric amplification process, in which case these phase shifts need to be determined very carefully. Not only the excitation pulses can cause a phase shift of the measured Ramsey fringes, also a phase shift in the atomic phase can be present, e.g. the AC-Stark (light-shift) appears as a shift of the measured Ramsey fringes and can influence the frequency determination from such quantum interference measurement. If the single pulse excitation amplitude becomes significant (leading to a population transfer of more than a few %), then it is more appropriate to use the Bloch vector model to describe the excitation process. However, the relative signal dependence on the time delay from which the transition frequency is determined remains the same.

2.4.1 A Ramsey-comb measurement

In contrast to more traditional Ramsey-type spectroscopy, where only a single isolated interference pattern can be recorded, *Ramsey-comb spectroscopy* enables the acquisition of multiple Ramsey signals at different time intervals. These intervals are separated from each other on a time scale that is orders of magnitude larger than the time interval over which the Ramsey interference signals are probed. This seemingly small extension of the original method leads to a significantly improved accuracy but also requires a specialized framework for analysis of the obtained signals. Although in a Ramsey-comb measurement signals are obtained as function of time, the results can be described equally well in the frequency domain, which are related to each other through their Fourier-transform relationship. In fact, many spectroscopic measurements use the frequency domain representation as the basis for fitting and extracting the relevant quantities such as transition frequencies. However, it turns out that the frequency determination from a Ramsey-comb measurement can be done better directly on the time domain signals (see Section 2.4.1). Nonetheless, it is still very instructive to think about the frequency domain and understand the equivalence

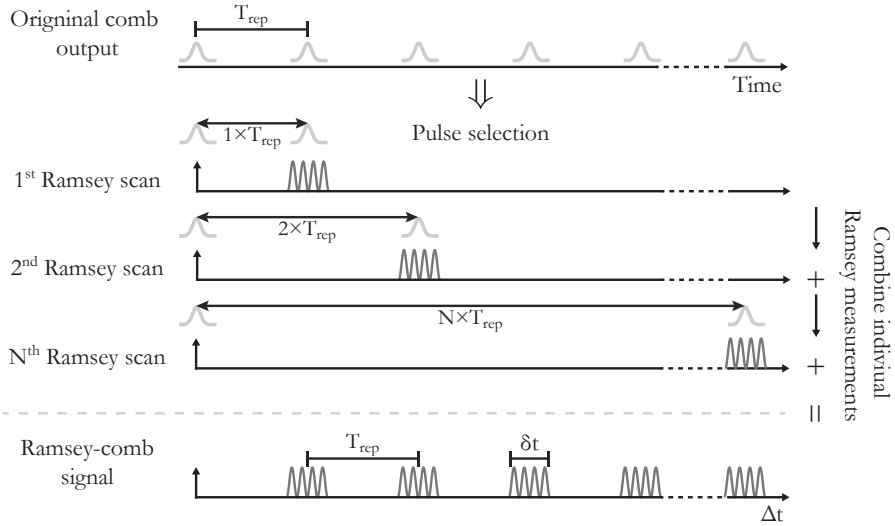


FIGURE 2.5: Schematic overview of the acquisition of a Ramsey-comb measurement. By selecting frequency-comb pulses at multiples of the fundamental repetition time a series of Ramsey-signals can be acquired. Each Ramsey signal is obtained by small adjustments of the repetition time over a timescale of ~ 100 as. The delay between the individual Ramsey signals, i.e. the repetition time of the frequency-comb, is orders of magnitude larger on the timescale of ~ 10 ns. These signals are combined afterwards to form a Ramsey-comb measurement and analyzed together.

between the time and frequency domain pictures. Therefore we first give a qualitative analysis of the signals from a frequency domain perspective and then continue to explain the details of analyzing Ramsey-comb signals in the time domain.

To perform a Ramsey experiment using frequency-comb pulses, first a pulse pair from the comb laser output need to be selected (see Chapter 3 for detail of the practical implementation). Then, as discussed in the previous section, interference 'fringes' in the excitation probability can be obtained by adjusting the relative phase of the excitation pulses, which can also be achieved through small adjustments of the pulse delay time Δt , see Eq. 2.21. In practice this is realized by adjusting the original repetition time ($T_{rep} \approx 8$ ns) of the frequency-comb laser through tiny steps ($\delta t \approx 5$ fs), i.e. $\Delta t = T_{rep} + \delta t$ ³. By selecting pulse pairs from the frequency-comb output at different multiples of the original repetition time and adjustments on the timescale of δt , multiple Ramsey-interference fringes can be recorded, as shown schematically in Fig. 2.5. The frequency-comb laser provides an absolute calibration of the pulse

³It should be noted that δt actually depends on the harmonic order that is used in the experiment. E.g. a 6 fs time step corresponds to 625 as for a two photon transition at the 4th harmonic of the original comb output.

time delay for the Ramsey measurements, and all individual scans combined form a Ramsey-comb measurement, see the bottom graph in Fig. 2.5.

Looking at it first in the frequency domain, something similar to a spectrum can be obtained by taking the direct Fourier transform (DFT) of the signals combined after adding the signals of the individual Ramsey scans, as shown in Fig. 2.6. The most notable feature of this "spectrum" is the reiteration of the spectral features, much like signals from traditional direct frequency-comb spectroscopy. This is caused by the sub-sampling of the Ramsey measurements, and as shown in the figure, the distance between the spectral features is inversely proportional to the spacing of the Ramsey measurements at T_{rep} . The second striking feature is that the overall width of the spectrum is inversely proportional to the width of a single Ramsey measurement⁴. Finally, the width of the spectral features is inversely proportional to the maximum delay time over which the transition is probed. This is a graphic representation of the fact that the measurement becomes more accurate if the transition can be probed over longer time delays.

Although the spectrum of a Ramsey-comb measurement is very similar to a spectrum obtained by more traditional direct frequency-comb spectroscopy, there are fundamental differences. In full repetition rate frequency-comb spectroscopy the excited state population is accumulated coherently over many pulses and the spectrum can be thought to be the result of scanning the comb modes over the resonances. In contrast, in Ramsey-comb spectroscopy one is probing the excited state after each pulse pair and later reconstructing the spectrum. This subtle difference leads to crucial consequences for the interpretation of the spectrum.

When only a single transition is probed this difference is not apparent, but when multiple resonances are excited at the same time interference between the spectral components influences the position of the transitions when the spectrum is calculated. This complicates fitting with often already arduous lineshape models. These issues can be circumvented by performing the analysis on the time domain signals directly as the information on the transition frequencies and their relative strength is encoded in the phase of the Ramsey signals (see Section 2.4.1) [68].

Ramsey-comb signal analysis

The time domain signals in a Ramsey-comb experiment, as depicted in Fig. 2.5, can be described by optical Ramsey interference fringes in combination with a repeating

⁴Note that this figure is not a simulation of a true Ramsey-comb measurement, in a measurement with 100 as long Ramsey measurements the overall width compared to the spectral feature is much larger, and many more than just five recurrences are observed

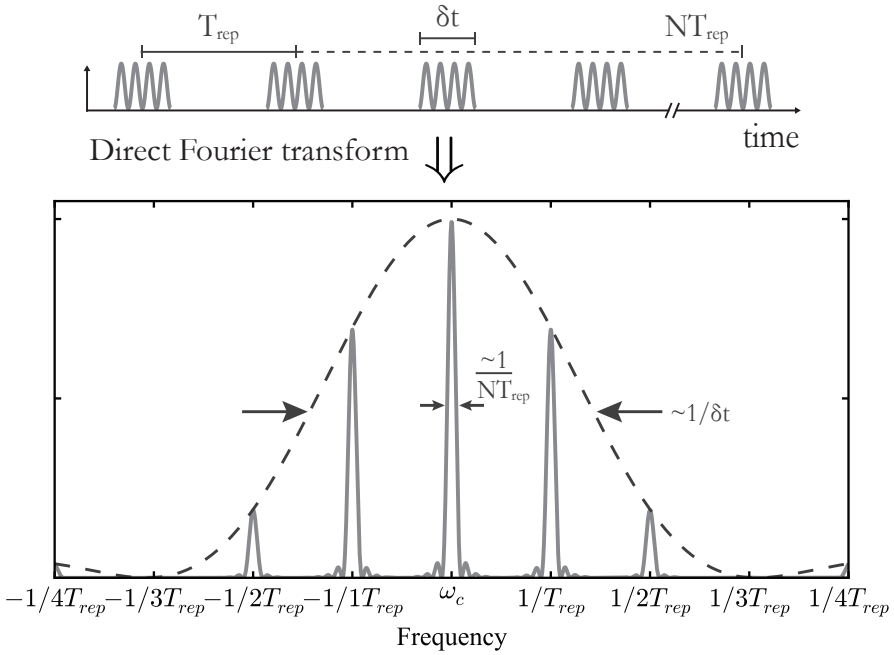


FIGURE 2.6: Illustration of a spectrum obtained from a Ramsey-comb measurement by Fourier transformation of the original data. The recurrence of the transition is caused by the sub-sampling of the Ramsey measurements and are spaced inversely proportional to T_{rep} . The overall width of the spectrum is inversely proportional to the duration of the individual Ramsey scans and the width of the spectral features is determined by the maximum time delay (NT_{rep}) at which the transition is probed.

rectangular windowing function:

$$S_{RC} = S_r(f_{tr}, A_{tr}, \Delta t, \Delta \phi) \times F_w(\delta t, \Delta N, T_{rep}) \quad (2.24)$$

The first term that describes the optical Ramsey fringes is given by Eq. 2.21 which can be extended to the case of multiple resonances as

$$\tilde{S}_r(f_n, A_n, \Delta t, \Delta \phi) = \sum_{n=0}^N A_n e^{-i(2\pi f_n \Delta t + \Delta \phi)} \quad (2.25)$$

where the complex notation is used and the constant offset is omitted since the obtained Ramsey signals can be scaled in arbitrary way without affecting the frequency. Although Eq. 2.24 can be used to fit the obtained Ramsey signals directly, this method suffers from the periodicity in the signal and coupling between fitting parameters.

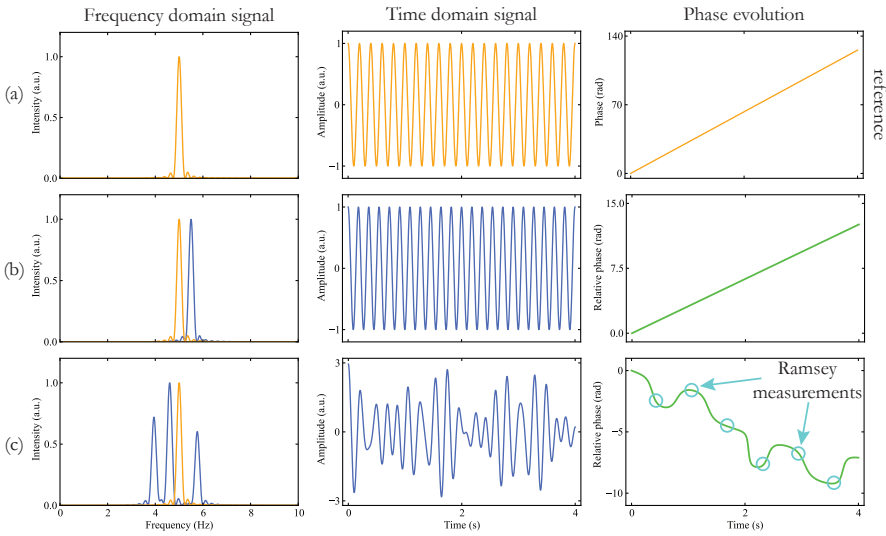


FIGURE 2.7: Visualization of time and phase evolution for a given spectrum, using low frequencies in the Hz range to illustrate the effects which in reality take place with optical frequencies. In the top row (Fig. a) the time and phase evolution of a signal frequency of 5 Hz are plotted. The phase evolution of Fig. b and c are plotted relative to the signal of Fig. a which is indicated by the orange trace in the frequency domain representation. In Fig. a and b only a single frequency is present in the signal leading to a phase evolution that is a straight line as function of time. In Fig. c multiple frequency components of different strength are present leading to complex evolution of the time and phase evolution.

Therefore a fitting model was developed that is based only on the phase of the obtained Ramsey-signals.

The evolution of the phase of a signal composed of different frequency components is graphically visualized in Fig. 2.7. The first figure in each row depicts a spectrum, the next two figures are the corresponding time domain signal and (relative) phase evolution. The top row (Fig. 2.7a) is an example of a spectrum that contains only a single frequency at 5 Hz. This leads to a straightforward oscillation in the time domain and a phase evolution that increases linear with time, and this signal will later be used as a reference. Similar, in the next row (Fig. 2.7b) a spectrum containing a single frequency at 5.5 Hz is considered (to enable a comparison the spectrum from Fig. 2.7a is also plotted in orange). But this time, instead of the absolute phase evolution, the phase evolution relative to the reference in Fig. 2.7a is plotted in the last column. The slope of the differential phase evolution is determined by the frequency difference between the signal and reference frequency. The situation can be made more complex by introducing additional frequency components of different relative strength

as depicted in Fig. 2.7c, where three different frequency components are present. The time evolution has now become a complex pattern caused by the beating between the different frequencies. Moreover, the phase evolution (which is again plotted relative to the reference in Fig. 2.7a) is no longer a straight line but also a complex function of time. Nonetheless, all the information about the frequencies and their relative strength is encoded in this phase evolution (modulo the periodicity at the distance of $1/T_{rep}$). It is precisely this phase evolution that is probed during a Ramsey-comb measurement. From each individual Ramsey measurement the phase can be extracted, relative to the reference frequency, thereby sampling the phase evolution as indicated by the open circles in Fig. 2.7c⁵. The picture above is not a full representation for excitation of multiple transitions, because in the optical measurements the frequencies are on the order of hundreds of THz, while the excitation frequencies are typically f_{rep} or less apart. So one observes phase deviations with what is essentially an effective optical carrier frequency. It should also be noted that the description above of excitation of multiple transitions at the same time assumes that these transitions are independent (e.g. exciting different isotopes). In other cases it might still be treated effectively like that because the only the phase evolution difference for different time delays is recorded. However, this needs to be checked for each experiment as potentially a more elaborate analysis is required to account e.g. for coherent effects between states.

The procedure to determine the frequency from a Ramsey-comb measurement is graphically depicted in Fig. 2.8. In this example, data from a real Ramsey-comb measurement in molecular hydrogen is presented where only one resonance is excited, and the blue data points are the measurement results with the accompanying statistical uncertainty. In total there are ten Ramsey measurements at regular intervals, indicated by the T_0 value, where each time a measurement is performed over two oscillation periods of the atomic resonance, corresponding to a pulse time delay variation of 600 as. In addition also a reference frequency, that is chosen to be as close as possible to the transition frequency, is plotted as the green trace in Fig. 2.8a. Then for each individual Ramsey measurement the phase difference ($\Delta\Phi$) with respect to the reference frequency is determined. This is achieved by fitting the Ramsey measurements separately with a cosine function with a fixed frequency but variable phase $\Delta\phi_{fit}$, i.e.

$$f(\Delta t, \Delta\phi, A) = A \cdot \cos(2\pi f_{ref} \Delta t + \Delta\phi_{fit}) \quad (2.26)$$

This "fixed frequency" fit is illustrated in Fig. 2.8a by the red line through the data points. The obtained phases are then compared to the phase of the reference frequency

⁵The frequency that is probed in a Ramsey measurement is much higher than depicted in Fig. 2.7. The Ramsey measurements are separated much further compared to the oscillation period

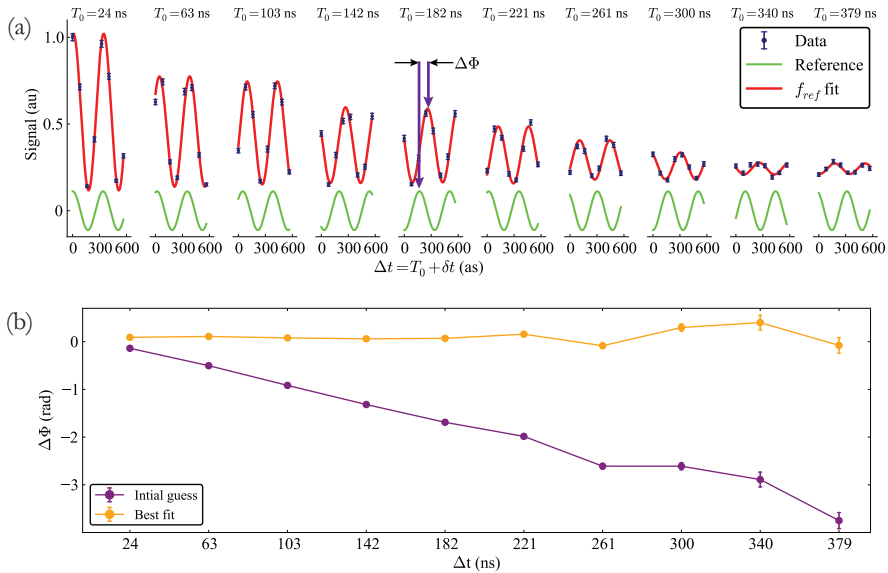


FIGURE 2.8: Visualization of the fit procedure based on the phase of the measured Ramsey signals. The measured Ramsey signals (blue data points) are fitted individually with a fixed frequency to determine a relative phase for each Ramsey measurement. The continuous evolution of the reference frequency (plotted in green) is compared to the obtained phases, plotted in the bottom figure. Minimization of the phase difference between the reference and measured phases as function of frequency (and amplitude) constitutes a least square minimization problem and can be solved by standard fitting algorithms. In the bottom figure the results for the phase difference of the first guess are plotted in purple. The result of the fitting procedure, i.e. minimization of the phase difference, is plotted in orange.

which is plotted in green below the experimental data in Fig. 2.8a, resulting in a value for $\Delta\Phi$ for each Ramsey measurement as indicated by the two purple arrows in Fig. 2.8a. This results in a phase evolution as function of delay time, Δt , which is plotted as the purple line in Fig. 2.8b. The frequency of the Ramsey-comb signal can then be obtained by minimizing the phase difference as a function of time. The phase difference between the Ramsey-comb measurement and the reference signal can be expressed as

$$\begin{aligned}\Delta\Phi &= \phi_{fit}(A_1, A_2, \dots, A_n, f_1, f_2, \dots, f_n, \Delta\phi_c, \Delta t) - \Delta\phi_{ref} \\ &= \phi_{fit}(A_1, A_2, \dots, A_n, f_1, f_2, \dots, f_n, \Delta\phi_c, \Delta t) - 2\pi f_{ref}\Delta t\end{aligned}\quad (2.27)$$

where A_n and f_n are possible frequency components and their relative strength. In addition, the possibility of a constant phase shift ($\Delta\phi_c$) is implemented that shifts all

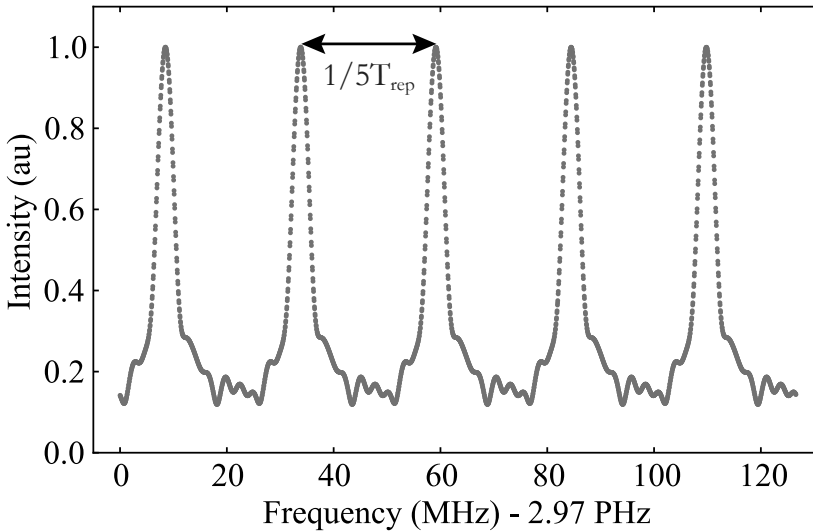


FIGURE 2.9: Spectrum of the measured Ramsey signal. Although the frequency determination is done completely on the time domain signals, this illustrates the ambiguity of the sub sampling of the Ramsey signal. In this case Ramsey measurements were done separated by five times the fundamental repetition time T_{rep} . As a result the frequency can only be determined modulo $f_{rep}/5$.

the Ramsey signals by the same amount. The minimization of the obtained phases from the Ramsey-comb measurement compared to the reference signal constitutes a χ^2 minimization problem. As long as the number of parameters, i.e. frequencies and their respective amplitudes, is lower than the number of obtained Ramsey signals a solution can be obtained by standard least-square fitting algorithms. The result of the fitting procedure as plotted in the orange trace in Fig. 2.8b.

The described procedure assumes that the phase difference between the measured phases and reference signal is caused only by the difference of the reference frequency with respect to the actual transition frequency. However, e.g. the phase of the Ramsey-comb measurements can be influenced by various effects such as e.g. the carrier-envelope phase shift of the frequency-comb pulses, or phase shifts due to the parametric amplification process. Such effects have to be carefully analyzed or measured to ensure that the transition frequency is not shifted (see Section 2.4.1). In the case of $\Delta\phi_{ceo}$ this is relatively straightforward because it is measured and stabilized so that the data can be corrected for this afterwards.

As mentioned earlier, similar to generic frequency-comb spectroscopy the sub-sampling of the phase trace leads to an ambiguity in the frequency determination.

In the example presented in Fig. 2.8, the Ramsey fringes were measured with a time separation of ~ 40 ns, which corresponds to 5 times the fundamental repetition time. Therefore, in this instance, the frequency can only be determined modulo $1/(5T_{rep}) = f_{rep}/5$, this is also visualized in Fig. 2.9 where the Fourier transform of the data in Fig. 2.8a is plotted. This ambiguity can be solved if the transition frequency is known precisely enough from previous measurements, or by measuring at different repetition times of the laser. In this particular example measuring Ramsey signals closer together, at e.g. an interval of $1 \times T_{rep}$, would already improve the resolution if needed.

One advantage of performing the analysis purely on the phases of the time domain signal is that the fitting procedure does not require any knowledge about the possibly complicated lineshape in the frequency domain. In a Ramsey-comb measurement the lineshape is further complicated by interference if multiple transition are excited simultaneously. Also, the phase is relatively robust against changes in signal strength, and the insensitivity to common phase shifts also means that the AC-Stark (light) shift is strongly suppressed, which is discussed in more detail in the next section. More detail and a quantitative analysis of the performance of the fitting algorithms can be found in reference [68].

The influence of phase shifts and broadening mechanisms

In the previous section in Eq. 2.27 the possibility of a constant phase shift was introduced. That a constant phase shift does not influence the result of a Ramsey-comb measurement can be understood by substituting $\Delta\phi = \Delta\phi_c$ into equation Eq. 2.25, and considering a single resonance, which results in

$$\tilde{S}_r = A_{tr} e^{-i(\omega_{tr}\Delta t + \Delta\phi_c)} \quad (2.28)$$

Straightforward Fourier transformation shows that the frequency is unaffected by this additional phase factor which is visualized in Fig. 2.10. The fact that identical spectra are obtained for the two traces in the top left graph in Fig. 2.10 is a fundamental difference with traditional Ramsey spectroscopy where only a single isolated Ramsey measurement is performed, and the assumption is made that for a delay of zero also the phase of the signal is zero. In that case a phase shift of the Ramsey fringes is interpreted as a frequency shift and must therefore be precisely calibrated.

In the experiments presented in this thesis the parametric amplification process changes the initial phase of the frequency-comb pulses. Therefore this needs to be carefully measured and accounted for if only a single Ramsey fringe is measured,

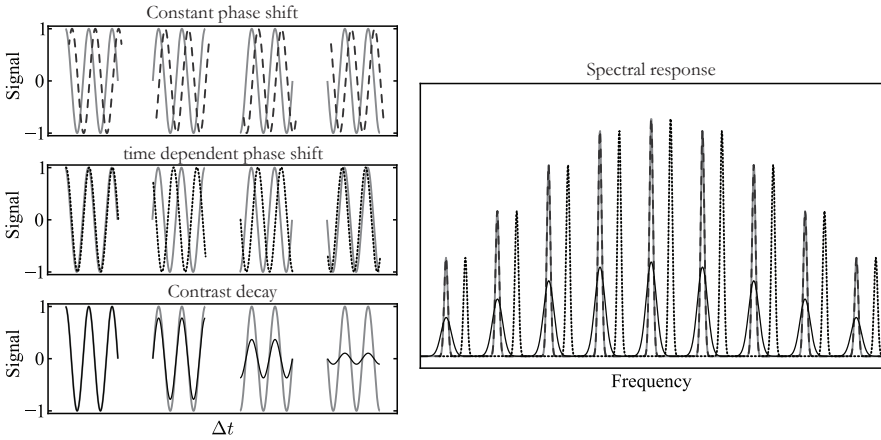


FIGURE 2.10: Visualization of the effect of a constant phase shift, time-dependent phase shift and a time-dependent decay of contrast on a Ramsey comb measurement. On the left time domain signals are plotted and on the right in the corresponding color the effect in the frequency domain.

which has been a source of significant uncertainty in previous experiments (see [63]). However, by measuring multiple Ramsey signals at different delay times, the absolute phase shift no longer matters, only the stability of the phase as function of time delay is important and needs to be verified (see [67]). The cancellation of common phase effects is a big advantage of the Ramsey-comb method because some systematic effects appear as a constant phase shift (under the right circumstances). Another example is the AC-Stark shift. Due to the intensity of the excitation pulses the energy levels are temporarily shifted, leading to a phase shift of the Ramsey-fringe that is proportional to the excitation energy. But if the energy of the excitation pulses is kept constant as function of delay time, then this phase shift is common to all Ramsey fringes and drops out of the analysis.

In contrast to a constant phase shift, a delay time dependent phase shift does influence the extracted frequency. The most simple case is a phase shift that is linear with respect to the delay time, i.e. $\Delta\phi = \Delta\phi_c\Delta t$. Inserting this into equation Eq. 2.25 and for simplicity limit the case to only a single transition gives

$$\tilde{S}_r = A_{tr}e^{-i((\omega_{tr} + \Delta\phi_c)\Delta t)} \quad (2.29)$$

Again Fourier transformation tells us that the extracted frequency is shifted proportional to the additional phase and cannot be disentangled from the signal, see Fig. 2.10. Potential phase shifts that have a time dependence therefore need to be carefully analyzed because they lead to a systematic shift of the measured frequency.

Just like other spectroscopic techniques the Ramsey-comb method is influenced by line broadening mechanisms. For example, in a Ramsey-comb measurement the broadening due to the finite lifetime of the excited state manifests itself as an exponential decay of the signal amplitude, see bottom left graph in Fig. 2.10. Other mechanisms that influence the Ramsey comb signal are the finite linewidth of the laser, the limited transit time in an atomic beam experiment, wave front curvature and Doppler broadening. All these mechanisms affect the amplitude and contrast (modulation depth) of the measured signal, and not necessarily as an exponential decay. However, the phase determination of the individual Ramsey scans is not hampered by them. However, there can still be a systematic phase shift, e.g. from a residual Doppler effect, which has to be taken into account just like with other spectroscopic methods.

The Ramsey-comb setup: from a frequency-comb laser to a high-intensity phase-stable pulse pair

3.1 Introduction

The development of the frequency-comb laser [56, 70] has revolutionized applications in the field of precision frequency metrology and fundamental tests by enabling the measurement of optical frequencies. In addition, frequency-comb lasers are an important tool for other fields of physics, such as attosecond science, quantum control and molecular dynamics. For many purposes the typical output (in the form of nJ-level pulse energy, or nW-level mode power) of a frequency-comb laser is sufficient, but for some applications it is desirable to increase the available pulse energy. In particular when one wants to extend the available wavelength range using nonlinear conversion techniques, to the extreme- and deep ultraviolet for ultra-high precision spectroscopy. This is desirable because ground state transitions of simple atoms (H, He, He⁺) and molecules (H₂) lie in this spectral range, which can be used to perform precise tests of fundamental theory such as quantum-electrodynamics (QED).

The availability of laser gain materials dictates that frequency-combs (typically) operate in the near and infrared spectral regions. Techniques such as second-harmonic generation or high-harmonic generation provide a route to operate these devices at shorter wavelengths. The pulse energy can be increased for this using enhancement cavities for intra-cavity high-harmonic generation [60–62] or by full repetition rate amplifiers [61, 99]. The downside of these techniques is that the maximum pulse energy can only be increased to several microjoules. An alternative approach is based on selective amplification of pairs of frequency comb pulses at a much lower repetition rate yielding a pulse energy of several millijoules, orders of magnitude more [97, 100]. A drawback in this case is that the spectral resolution seems to be severely limited as shown in Fig. 1.2. However, with the Ramsey-comb technique (see Chapter 2) this issue is circumvented and the resolution of the original comb is recovered.

As described before, a spectroscopic experiment performed with only two frequency-comb pulses resembles a Ramsey-type experiment. In this case it is crucial that the

pulse to pulse phase shift is exactly known, because otherwise it leads to a systematic frequency shift. Originally the laser system was designed to only support the amplification of two consecutive pulses [66, 100]. This limited the accuracy due to the constrained time delay between the excitation pulses and the requirement to know the absolute phase difference. Although the pulse to pulse phase shift is known for the initial frequency-comb pulses, it is changed in the amplification process. To tackle these issues the laser system was upgraded to support amplification of frequency-comb pulse pairs at multiples of the original repetition time to perform Ramsey-comb spectroscopy (see Chapter 2).

The complete laser system that produces a phase-stable amplified frequency-comb pulse pair is called the Ramsey-comb laser system, see Fig. 3.1 for a schematic overview of the main components. A mJ pulse pair is created by parametric amplification of the frequency-comb. Experimentally, this requires a well controlled high-energy pump-pulse pair that is synchronized with the frequency-comb laser. These pump pulses are produced by a Nd:YVO₄ oscillator operating at 1064 nm wavelength, from which a pulse pair is selected using fast modulators at a repetition rate of 28 Hz. These pulses are amplified in a 'bounce' amplifier [101, 102] and a subsequent post amplifier to a pulse energy of 28 mJ. They are then frequency doubled to 532 nm wavelength and used to pump the non-collinear optical parametric chirped pulse amplifier (NOPCPA). The seed pulses for the NOPCPA are generated by a Ti:sapphire based frequency-comb that operates around 800 nm with a bandwidth of approximately 100 nm. Before seeding the NOPCPA, the pulses are lengthened in time (by applying second-order dispersion in a grating-based stretcher, and spectral clipping in this stretcher) to have optimal temporal overlap with the pump pulses in the NOPCPA. In addition, a setup to measure the relative phase between the amplified and original frequency-comb pulses is implemented to ensure phase stable operation of the NOPCPA.

In this chapter all the components of the Ramsey-comb laser system are described in detail. In the last section the phase measurement setup is discussed in combination with experimental results. Because the phase plays such an important role in the frequency determination extra emphasis is put on this section.

3.2 The frequency-comb laser

The heart of the experiment is formed by a home-built frequency-comb laser, see Fig 3.2 for a schematic overview. The frequency-comb laser is based on a Ti:sapphire Kerr-lens mode-locked oscillator that produces a pulse train with a repetition frequency of 126 MHz. The Ti:sapphire crystal is pumped by 5.0-5.25 W of 532 nm light delivered

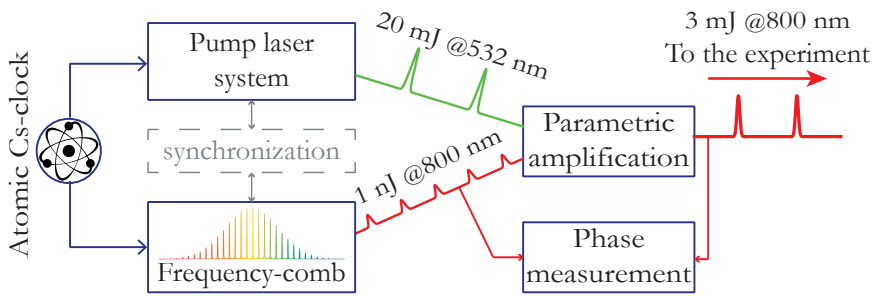


FIGURE 3.1: Schematic overview of the Ramsey-comb laser setup. Pulses from a frequency-comb laser are amplified in a non-collinear optical parametric amplifier. The pump pulses are derived from a synchronized amplified Nd:YVO₄ oscillator. The frequency-comb is referenced to an atomic-cesium clock to provide absolute frequency calibration. In addition, a phase-measurement setup monitors the effects on the phase due to the parametric amplifier.

by a commercial Coherent Verdi V-10 laser system. The oscillator has a linear cavity design where one end mirror of the cavity is formed by a 85 % reflective output coupler. The other end mirror is mounted on a translation stage to allow coarse adjustment of the repetition rate of the laser, and in addition two folding mirrors and two strongly focusing mirrors are implemented leading to a cavity length of 2.4 m. To sustain mode-locking over a large bandwidth, the group velocity dispersion in the cavity needs to be compensated, this is achieved by using chirped mirrors. The specific choice of mirror characteristics gives a degree of control over the center wavelength and spectral width (related to the pulse duration) of the output spectrum. To accommodate the experiments presented in this thesis the frequency-comb laser was modified to produce the two different output spectra shown in Fig. 3.3. In both cases the average output power is ~ 700 mW which corresponds to a pulse energy of 5.5 nJ. To operate the mode-locked Ti:Sapphire laser as a frequency-comb both the repetition frequency and the carrier-envelope offset frequency (see section 2.2.1) need to be stabilized and referenced to a primary time standard such as a atomic cesium clock.

The repetition rate of the laser is the most straightforward parameter to stabilize, and this is achieved by adjusting the cavity length through a voltage on a piezoelectric transducer on which one of the mirrors is mounted (see Fig. 3.2). The repetition rate is measured by detecting the pulse train with a 10 GHz bandwidth fast photo-diode (Electro-Optics Technology EOT4000). Then the 76th harmonic of the fundamental (126 MHz) is mixed with the output of a stable frequency generator at 9.7 GHz (Agilent PSG-L E8241A). The higher the locking point, the smaller the arm to the optical domain, and the more tightly the comb modes can be locked. However, the

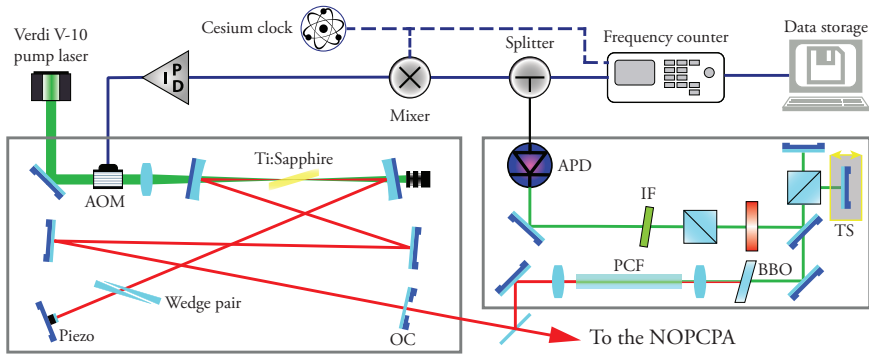


FIGURE 3.2: Schematic overview of the Ti:sapphire oscillator and $f : 2f$ measurement setup. A Coherent Verdi V-10 laser pumps the Ti:sapphire crystal with 5.25 W of 532 nm. The crystal is placed at Brewsters angle between a dispersion compensated curved mirror pair. One end-mirror is glued on a piezo-electric transducer to allow active feedback on the cavity length, while the other end-mirror is formed by an 85 % reflective output coupler (OC). A pair of wedges is inserted for coarse control of dispersion in the cavity. About 25 % of the output is split off and coupled into a photonic crystal fiber (PCF) for continuum generation in the $f : 2f$ setup to measure the f_{ceo} frequency. The f_{ceo} is compared to the 10 MHz output of an cesium atomic clock and actively stabilized via the pump-laser intensity which is adjusted through an acoustic optic modulator (AOM). (APD) Avalanche Photo Diode, (TS) Translation Stage, (BBO) β -Barium Borate crystal, (IF) Interference filter.

generator is more noisy at higher frequencies, so a locking point at 9.7 GHz is a compromise between both effects. The frequency generator is phase locked to the 10 MHz output of a cesium atomic-clock (Symmetricom CsIII 4310B) to provide an absolute frequency reference for the repetition rate. Control of the repetition rate through the 10 GHz frequency generator is undesirable because of a dead time in the output that occurs between two different frequency settings. Therefore the beat signal is offset by ~ 28 MHz. This 28 MHz difference frequency is then mixed with the output from a direct digital frequency synthesizer (DDS) board (AD9912, Analog Devices) which is also referenced to the atomic cesium clock. The resulting difference frequency is used as the error signal in a PID feedback loop that controls the voltage of the piezoelectric transducer. In this configuration the repetition rate can be adjusted in steps of μHz by setting the frequency of the DDS and keeping the frequency of the 10 GHz generator at a fixed value.

Control over the carrier-envelope offset frequency (f_{ceo}) is not straightforward because the laser output does not contain any intensity at frequencies close to zero, and it can therefore not be measured directly. This problem has been solved by the $f : 2f$ technique [56, 70], in which the carrier is frequency doubled (time domain view point),

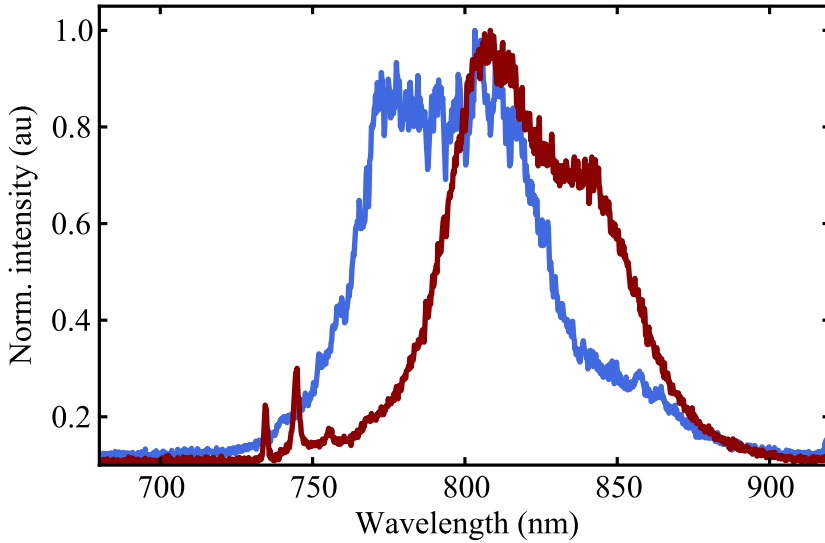


FIGURE 3.3: Output spectra of the Ti:sapphire frequency comb for two different sets of dispersion compensating mirrors. By changing the dispersion characteristics of the mirrors inside the cavity the output spectrum can be shifted. The red curve shows the spectrum that was used for the experiments on krypton (see 4), while the blue spectrum was used for the molecular hydrogen experiments (discussed in Chapter 5).

corresponding to sum frequency of the modes (in the frequency domain), leading to light at frequencies of $f_m = m f_{rep} + 2 f_{ceo}$ (see Eq. 2.7). If the spectrum of the oscillator spans a full octave then the modes obtained by sum-frequency mixing can be compared in an interferometer to modes at the high frequency side in the original comb light close to the upconverted comb. The resulting beat signal between these modes contains the difference frequency which is equal to f_{ceo} . The beat signal will also contain other components due to interference between different modes but these can be filtered out electronically. Experimentally it is difficult to create a mode-locked laser that has an output spectrum spanning a full octave. Instead, the high peak intensity of the short pulses can be used to induce non-linear interactions to broaden the original spectrum. This can be achieved in photonic crystal fibers which are fibers that have a lattice of air holes around the core. This structure can then be engineered such that the group-velocity dispersion is zero near the central wavelength of the pulse so that the pulse remains short and intense over an interaction length of many cm. Due to the long path the spectrum can be broadened sufficiently, leading to a so called super-continuum that can easily span the required octave for the $f : 2f$ technique.

The implementation of the $f : 2f$ technique in our experiment is shown in Fig. 3.2.

About 25 % of the oscillator output is split off and injected into a photonic crystal fiber of 16 cm length and 2 micron core diameter to create an octave spanning spectrum. The low frequency part of the spectrum is then 'doubled' in a BBO crystal and compared to the high frequency part in a Michelson interferometer geometry. The beat signal is recorded with a avalanche photo-diode (Analog Modulus Inc. 712-A) and electronically filtered to extract only the f_{ceo} .

The carrier-envelope offset frequency is related to the pulse-to-pulse phase slip ($\Delta\phi_{ceo}$) through $f_{ceo} = (\Delta\phi_{ceo}/2\pi)f_{rep}$. The pulse-to-pulse phase slip is caused by a difference in phase velocity and group velocity inside the laser cavity. Coarse adjustment of the carrier-envelope phase offset is realized by inserting a fused silica wedge pair in the cavity. By moving one of the wedges in or out of the beam the amount of dispersive material in the cavity is changed, leading to a relative change between the phase and group velocity. Fine control and active stabilization of f_{ceo} is achieved through control of the pump intensity, causing a change in the refractive index (and therefore mostly the phase velocity) through the Kerr effect in the Ti:Sapphire crystal. Experimentally, modulation of the pump intensity is achieved by inserting an AOM (IntraAction Corp. AFM 804A1) in the pump beam. By adjusting the RF-power in the AOM the pump intensity can be adjusted with sufficient range and accuracy. The error signal for the feedback loop is generated by comparing the measured f_{ceo} to the 10 MHz output of the atomic cesium clock. In addition, the f_{ceo} frequency is also measured with a frequency counter (Agilent 53131A) that is connected to the measurement control computer. During the experiment the f_{ceo} is monitored and stored to ensure that it is properly stabilized.

Together the stability of the f_{ceo} and the f_{rep} define the linewidth of the individual comb modes, although in practice the f_{rep} has the biggest contribution to mode broadening through mechanical vibrations. The linewidth is an important parameter because it can be a limiting factor in the precision that can be achieved in a Ramsey-comb measurement, by reducing the modulation depth (contrast) of the Ramsey-fringes. To determine the linewidth of the frequency-comb a beat note was generated with an ultra-stable laser (Menlo Systems ORS1500). The ultra-stable laser operates at 1542.48 nm and has an initial specified linewidth of less than 1 Hz. This laser is injected into a 10 m fiber and amplified with a commercial fiber amplifier (NKT Photonics Koheras Boostik). Part of the amplified light is doubled to 771.24 nm, which is within the spectral range of the frequency-comb, and injected into another piece of 5 m single mode fiber to reach the Ti:sapphire comb laser. A small part of the spectrum around 771 nm is selected via a grating and injected into a fiber.

The light from the ultra stable laser, and the frequency comb are combined using

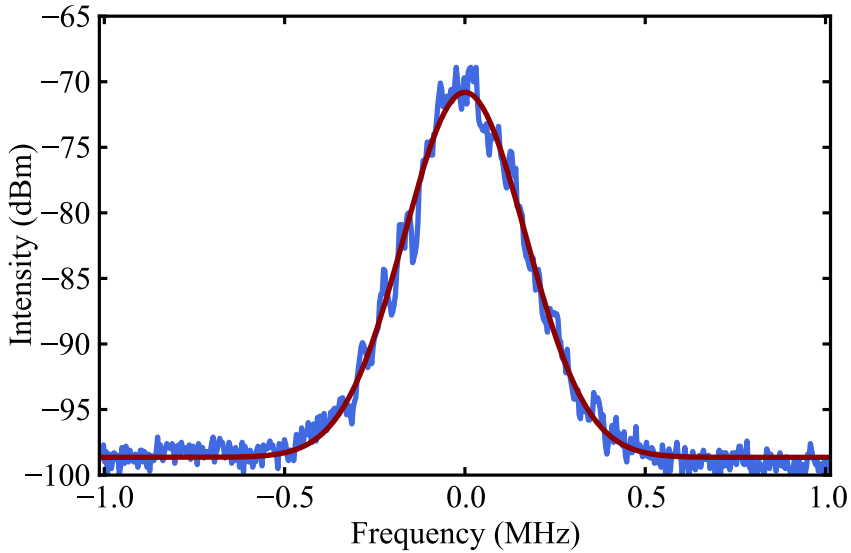


FIGURE 3.4: Beat signal between the ultra-stable reference laser and the frequency comb at 771.24 nm. The signal is fitted with a Gaussian leading to an estimated linewidth of the frequency-comb modes of 165 kHz (FWHM) with day-to-day variations of 75 kHz.

a fiber combiner, and is subsequently measured with a photo diode. The photo diode signal contains the difference frequency between the ultra stable laser and the closest frequency-comb mode. This beat signal is electronically filtered and amplified to increase the signal-to-noise ratio. A result of measurement is shown in Fig. 3.4 and from the fit we can determine a linewidth for the frequency-comb modes of 165 kHz (FWHM). This could vary on a day-to-day basis with as much as 150 kHz. The fibers and amplifier add noise, i.e. additional linewidth, to the original spectrum of the ultra stable laser but this is still far less compared to linewidth of the frequency-comb.

There are a few points noteworthy concerning the linewidth of 165 kHz that is reported here. First of all, the manner in which the linewidth influences a Ramsey-comb measurement is through the contrast of the observed Ramsey fringes. In the time domain picture: as the delay time between the pulses increases the relative variation in timing of the second pulse with respect to the first one progressively leads to a smaller contrast. Because the relative phase is determined by the time delay (and f_{ceo}) this is proportional to the stability of the f_{rep} , i.e. the linewidth. Transitions to an excited state exhibiting a longer lifetime, can be observed over longer time delays. That means that the linewidth of the comb modes needs to be sufficiently narrow to be able to observe Ramsey fringes. For the initial experiments that have

been performed on krypton, as presented in Chapter 4, the linewidth of the laser was much larger, roughly 1.5-2 MHz. However, because the lifetime of the excited state was only 55 ns the influence of the linewidth of the comb was not yet so limiting. But for the experiments on molecular hydrogen, as presented in Chapter 5, where the lifetime of the excited state is 200 ns, the influence of linewidth of the comb modes could be observed. The 1.5-2 MHz linewidth was mainly caused by acoustic and mechanical noise that was added to the cavity through the water cooling system of the base plate of the frequency-comb cavity. By building an additional housing with specific noise canceling foam around the laser cavity, and dampers in the cooling system, the linewidth could be reduced to 165 kHz, see Fig. 3.4. In order to probe transitions over even longer delay times, for example for He^+ with a lifetime of 1.9 ms, it is required to improve the linewidth even further. This would require the laser to be locked directly to the ultra stable optical reference which should be possible in the future with the newly developed high-current (5A peak) piezo-driver for sufficiently fast feedback. Alternatively the recently acquired ultra-low noise frequency comb (FC1500-250-ULN) from Menlo Systems could be used.

3.3 The pump laser system

The pump laser system that provides a high-intensity pulse pair to drive the NOPCPA consists of three major parts; the oscillator, a bounce amplifier and a post amplifier. From the initial pulse train a pulse pair is selected using acoustic and electro-optic modulators before the first amplification stage in the bounce amplifier. In addition, after the bounce amplifier Pockels cells are implemented to be able to adjust and stabilize the intensity of the pulse pair going into the post amplifier. In this section a detailed description of each part of the pump pulse system is given.

3.3.1 The pump laser oscillator

The oscillator that provides the necessary laser pulses is based on a Nd:YVO_4 crystal that is pumped by a diode producing 29 W of continuous light at 880 nm (Jenoptik, JOLD-30-CPXF-1L) [103] which is delivered through a 400 μm core fiber. The light from the fiber is imaged into the Nd:YVO_4 crystal whose surfaces are anti-reflection (AR) coated for 880 nm and wedged by 1.5° to avoid unwanted lasing effects. A schematic overview of the cavity is shown in Fig. 3.5. One end mirror of the cavity is formed by the exit surface of the Nd:YVO_4 crystal, which has, in addition to the 880 nm AR coating, also a 90 % reflective coating for 1064 nm. The other end mirror of the cavity is formed by a semiconductor saturable absorber mirror (BATOP GmbH)

that has a modulation depth of 1.2 % and a relaxation time of 10 ps, providing the passive mode locking mechanism. The repetition rate of the laser can be controlled through one of the folding mirrors that is glued on a single-stack piezoelectric transducer (Physik Instruments GmbH), which in turn is glued onto a heavy counterweight cone filled with lead [104]. The range of this feedback is limited on the order of a few μm and therefore thermal drifts during the day can cause the piezo to reach its limits. To prevent this from happening the base plate of the cavity is water cooled and a feedback mechanism is installed to keep the piezo within its working range by adjusting the temperature of the cavity base plate. The Nd:YVO₄ laser provides an output of 5 W at a repetition frequency of 126 MHz, with a spectral width of 0.25 nm centered around 1064 nm. Because the gain material in the post amplifier is Nd:YAG, which has a much smaller gain bandwidth and slightly shifted center, the spectral width has to be decreased in order to efficiently amplify in the post amplifier. To meet this requirement less than 0.05 nm bandwidth is selected using a 4f-grating based system with an adjustable slit placed in the Fourier plane. As a result we obtain pulses with a duration between 60 and 80 ps depending on the specific requirements of operating the NOPCPA. Due to the spectral clipping and losses in the grating the total efficiency is roughly a few percent, leading to a final pulse energy on the order of 1 nJ. These pulses are coupled into a single mode fiber to decouple the optical alignment of the oscillator from the subsequent amplification stages.

The selection of a pulse pair from the initial 126 MHz repetition rate (~ 7.9 ns repetition time) requires fast modulators. This is achieved with a fiber-coupled electro-optic modulator (EOM) (AM 1060 KF, Jenoptik) which requires only ~ 3 V and can sustain high repetition rate switching. This is particularly convenient because it can be controlled using commercial delay generators (Stanford Research Systems DG645), providing an easy programmable control over the pulse selection. However, the extinction ratio of the EOM is on the order of 33 dB, which results in unwanted pulses leaking through and depleting the gain in the amplifiers. To increase the extinction ratio a fiber-coupled AOM (Gooch and Housego T-M150-0.4) is placed in series before the EOM. The rise time of the AOM is much slower (30 ns) and can therefore not be used to select single pulses, but the higher extinction ratio ensures a loss of more than 80 dB outside the gate of both pulse picking gates, see Fig 3.5.

3.3.2 The bounce amplifier

After the spectral selection and the losses introduced by coupling into the fiber, and pulse selection by the AOM and EOM, two pulses with an energy of 30 pJ remain. These pulses are amplified in a bounce amplifier system (see Fig 3.6) consisting of two

be considered carefully. Because the first pulse takes out a significant amount of the stored energy in the amplifier crystals, the second pulse is subject to a significantly different gain medium. This would lead to a much stronger first pulse if the pulses are injected into the bounce-amplifier with equal energy. However, it is important for correct operation of the NOPCPA that the two pump pulses are as identical as possible [69]. To compensate for this gain depletion effect the two pulses are injected with an unequal pulse energy into the bounce-amplifier such that the resulting amplified pulses are exactly equal in energy. Experimentally this is achieved by adjusting the gates of the EOM differently such that the pulse seeding energy has a ratio of $\sim 1:4$ (see Fig 3.5). As a result the bounce amplifier delivers two pulses with an energy of 0.95 mJ and a Gaussian beam profile ($M^2 < 1.2$) with a FWHM of 1.5 mm [102, 105].

3.3.3 The post amplifier

To further amplify the pulses up to the required 20-30 mJ energy level a Nd:YAG based diode pumped post amplifier is used, see Fig. 3.6 for a schematic overview. The main component of the post-amplifier is an amplification module (Northrop Grumman REA6308-3P200HT) which houses a Nd:YAG rod of 14.6 cm length and 6.4 mm diameter, and is pumped by 120 quasi-cw diodes with a combined peak power of 24 kW. The diodes are configured in a five-fold symmetry around the rod. When seeding the amplifier module with a Gaussian beam this non-uniform pumping is mirrored in the intensity profile at the outer rim of the beam, and in addition diffraction from the edges of the amplifier aperture may be observed. These effects lead to high-intensity hotspots which need to be avoided in order to stay below the damage threshold of (possibly expensive) optical elements [69, 108]. Moreover, to be able to extract the maximum amount of stored energy a uniform beam profile across the diameter of the rod is desirable. To obtain a uniform intensity profile the seed beam is expanded to 6 mm FWHM and the center part is selected using a 3.5 mm diameter pinhole. Propagation of such a "flat-top" intensity profile immediately leads to diffraction caused by the hard edges of the pinhole. Therefore the beam needs to be relay-imaged throughout the amplifier and NOPCPA to recover the flat intensity profile (and phase front) at the essential optical elements. After the pinhole the beam is relay-imaged onto the entrance surface of the amplifier module with a beam diameter of 4.9 mm to avoid diffraction from the module aperture, and to ensure homogeneous amplification across the beam. The amplifier is operated in a double pass configuration where a Faraday rotator is placed between the two passes to rotate the polarization by a total of 90° . The rotator compensates for thermally induced depolarization effects and allows the back reflected beam to be coupled out by a thin-film polarizer. The amplifier module

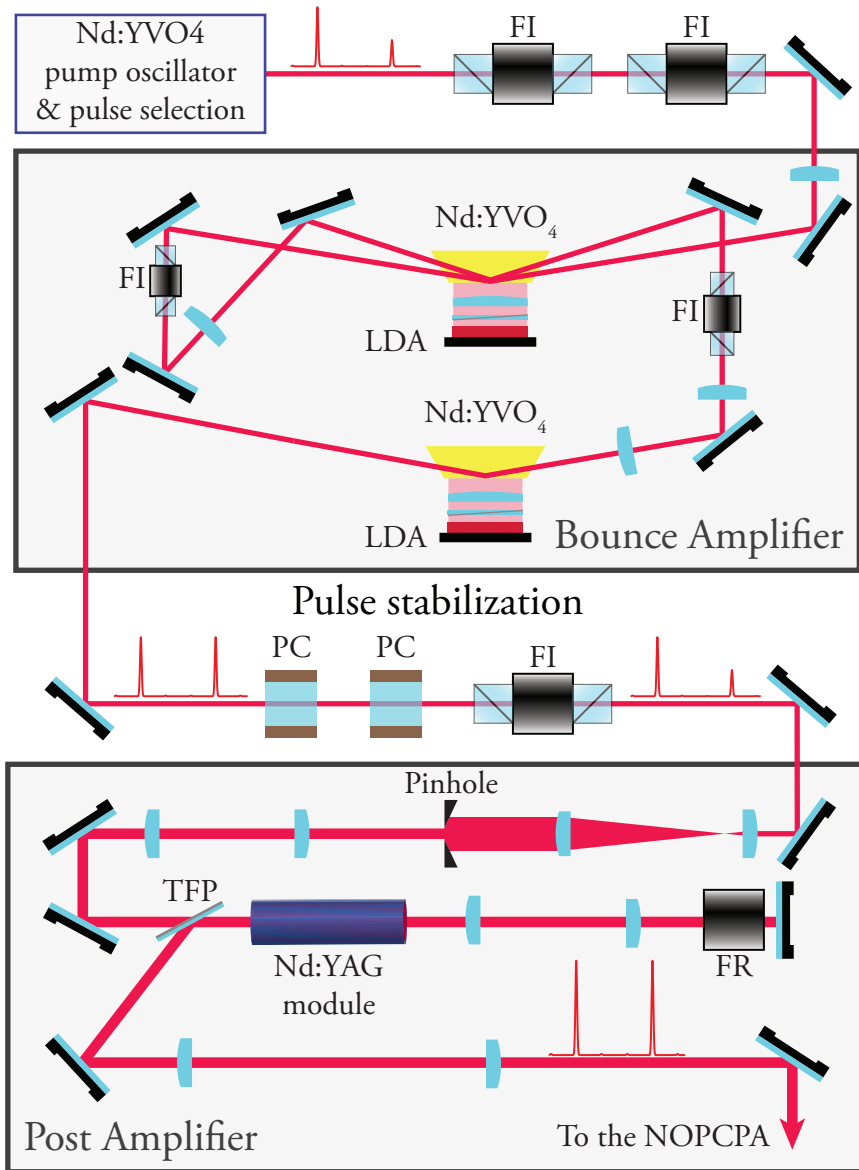


FIGURE 3.6: Schematic overview of the bounce and post amplifier after the Nd:YVO₄ oscillator. The bounce amplifier consist of two Nd:YVO₄ crystals that are pumped from one side by a linear diode array (LDA). The light is imaged on the crystal by cylindrical lenses and a waveplate is used to align the polarization to the c-axis of the crystal. The first crystal is operated in a double pass configuration and the second crystal in a single pass configuration, leading to a pulse energy of nearly 1 mJ. After the bounce amplifier two Pockel cells are used that filter out unwanted pre- and between- pulses, and are used to adjust the relative intensity. The beam is then enlarged and the center is selected using a pinhole to create a flat-top beam profile. The beam is then relay-imaged through a diode pumped Nd:YAG crystal which is operated in a double pass configuration. After the post amplification stage the pulses have a energy of 25-30 mJ. FI = Faraday isolator, FR = Faraday rotator, TFP = thin-film polarizer.

is operated with currents between 80-85 A, leading to a final pulse energy of typically 27 mJ.

Similar to the bounce amplifier, seeding the post amplifier with two equal pulses will result in a much more energetic first pulse and different temporal profiles. Therefore the energy of the seed pulses is again adjusted to obtain two identical pulses after the amplification process. This is achieved using two Pockels cells (Lasermetrics 5046ER-VC) in combination with an optical isolator. This configuration serves a double purpose because the operating voltage of Pockels cell can be adjusted in an active feedback loop to stabilize the output energy ratio of the two pulses. Moreover, the Pockels cell provides another mechanism to suppress unwanted pulses that can take out gain between the two amplified pulses.

For the experiments described in Chapter 4 only a single Pockels cell was inserted between the two amplifiers. To control the relative pulse energy, the rising edge of the optical gate of the Pockels-cell was adjusted leading to changes in the amount of polarization change of the first pulse (see Fig. 3.7). In this case the feedback mechanism was based on changing the relative timing of the Pockels cell gate with respect to the first pulse. Even though this solution worked surprisingly well it did suffer from excess amplitude noise of the first pulse due to timing jitter on the steep slope of the rising edge. In addition, the pulses in between the two amplified pulses were not suppressed, causing the gain to be depleted before amplification of the second pulse. For experiments where a relatively short pulse delay is used this is not a significant issue, however for experiments where longer delay times are required this plays an increasingly important role (see Chapter 5). The updated configuration with two Pockels cells is shown in part (b) of Fig. 3.7.

3.3.4 Repetition rate synchronization

In order to amplify the frequency-comb pulses in the NOPCPA the pulses from the frequency-comb and pump laser have to coincide in the NOPCPA with picosecond precision. To achieve this the repetition rates of both lasers have to be synchronized and stabilized very accurately. The stabilization of the repetition rate of the frequency-comb laser was already discussed in section 3.2, and the locking of the repetition rate of the pump laser is nearly identical. The repetition rate is again measured using a 10 GHz bandwidth fast photo-diode (Electro-Optics Technology EOT4000). The 76th harmonic of this signal is mixed with the same 9.7 GHz reference as was used for the frequency comb with an offset of ~ 28 MHz. This signal is then mixed with the 28 MHz output of the DDS to provide the error signal for a PID feedback loop controlling the cavity length with the piezo mounted mirror inside the cavity. Using

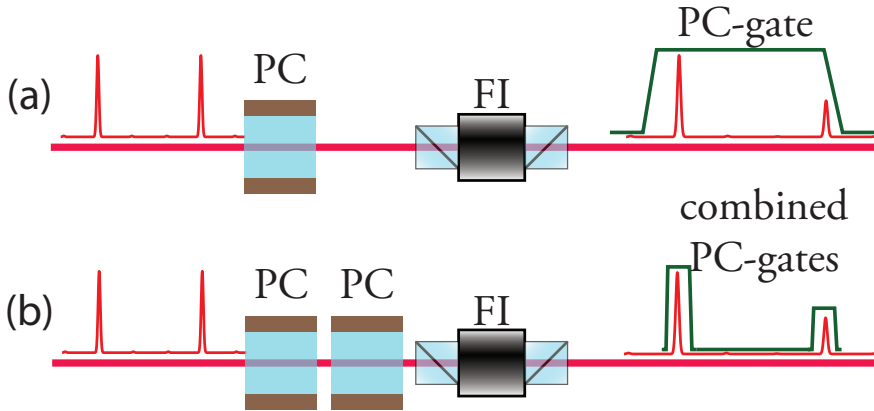


FIGURE 3.7: Sketch of the mechanism to control the relative pulse intensity. In (a) the 'old' situation is shown where the intensity of the first pulse was adjusted through adjustments of the timing of the rising edge of a Pockels gate before seeding the post amplifier. In (b) the 'new' situation is shown where each pulse is selected by a Pockels cell and the intensity of the first pulse is adjusted by adjusting the high-voltage of the Pockels cell.

the same reference for the frequency-comb and pump laser provides a synchronous lock of the repetition rates (see Fig. 3.8 for a schematic overview of the electronic scheme). However, there can still be a phase offset between the repetition rate of the pump oscillator and frequency comb that is not reproducible each time the lasers are locked. To ensure temporal overlap in the NOPCPA a phase shift mechanism for one of the locking schemes is required which is technically difficult to achieve at the 9.7 GHz of the lock. Instead, this is realized by installing a second "slow" repetition rate lock only for the frequency-comb laser. The repetition rate is also mixed directly at 126 MHz with the doubled output from another frequency generator (Agilent 33250A). This device provides a straightforward way to change the phase over 360° such that the temporal overlap between the pump and frequency comb pulses in the NOPCPA can always be obtained. Switching between the "fast" and "slow" repetition locks is realized through a potentiometer that allows a gradual change between the two locks, see Fig. 3.8. After switching from the "slow" lock to the "fast" lock the temporal overlap between the pump- and frequency-comb pulses can be fine-tuned even further using a physical delay line in the path of the frequency comb.

stage. The comb beam is then expanded and overlapped with the pump beam in a second BBO crystal of the same length (see Fig. 3.9). Here the pulses are amplified to an energy of 2-3 mJ where the second and third amplification passes are operated in the saturated regime. The flat-top intensity profile of the pump beam is reproduced in the amplified frequency-comb beam, leading to diffraction patterns after propagation. In order to create a collimated beam with a Gaussian intensity profile a 2f-lens system is built up with an additional spatial filter in the Fourier plane that filters out the higher-order spatial modes (see Fig. 3.9).

As a result, the laser system presented in this Chapter produces two near infrared frequency-comb pulses with an energy upto 3 mJ (see also [66, 69, 97, 108] for earlier versions of the system). The delay between the pulses can be adjusted on a very short time scale (attoseconds) by small adjustments of the repetition rate and on a much longer time scale (nanoseconds) by selecting a different pump pulse pair. The next section discusses in detail the influence that the pump pulses exert on the phase of the frequency-comb pulses.

3.5 The phase measurement setup

During the parametric amplification process the pump pulses influence the phase of the amplified frequency-comb pulses [69, 109]. This is a potential source of a systematic error in the frequency determination from a Ramsey-comb measurement, but only if this phase distortion is not constant as function of time delay. The pump laser system was specifically designed to avoid such spurious phase shifts by keeping the characteristics of the pump pulse pair as constant as possible as function of the delay time [69, 102, 105]. To ensure that these amplification-induced phase shifts do not influence the measurements, an additional phase measurement is performed to accurately determine the relative phase difference between the excitation pulses.

The phase difference of the amplified frequency-comb pulses is measured based on linear spectral interferometry in a Mach-Zehnder type interferometer, see Fig. 3.10 for a schematic overview (see also Ref. [108, 109]). It has the advantage that pulse intensity fluctuations do not influence the measurement much. In addition, this setup has the benefit that the wavelength dependence can also be measured. The reference to compare the amplified pulses with is formed by the original frequency-comb pulses, which are split off before the NOPCPA by a half-wave plate and polarizing beamsplitter cube. Before combining the reference pulses with the amplified pulses the path length of the reference pulses is matched to the path length of the NOPCPA to ensure interference with its original counterpart. This procedure eliminates the influence $\Delta\phi_{ceo}$

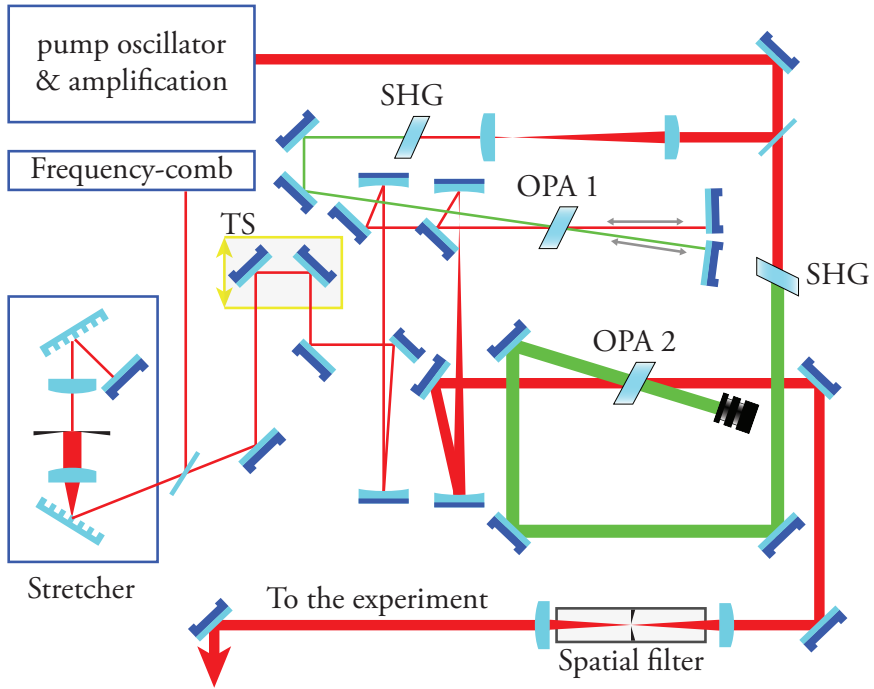


FIGURE 3.9: Overview on the non-collinear optical parametric amplifier (NOPCPA) which consists of three amplification stages in two BBO crystals (OPA1 and OPA2). Each crystal is pumped with the frequency-doubled pulses (532 nm) from the pump laser system. The seed pulses are first lengthened in time in 4f-grating based stretcher and then overlapped with the pump pulses in the NOPCPA-crystals. To fine tune the timing between the seed and pump pulses a manual translation stage (TS) is implemented. The amplified frequency-comb pulses are focused in a vacuum tube with a spatial filter to obtain a collimated beam with a Gaussian intensity profile. (SHG) second harmonic generation

of the original frequency comb pulses from the measurement. In addition, a second stretcher that is identical to the stretcher before the NOPCPA is installed to match the chirp of the reference to that in the amplified pulses. After the recombination both the reference and amplified pulses are coupled into a large mode area fiber ¹ to ensure perfect mode overlap. To avoid unwanted background signal from the non-amplified frequency-comb pulses, two Pockels cells (Lasermetrics 5046E) are used in series. The timing and duration of each Pockels cell gate is set such that it rotates either the first or second pair of reference and amplified pulses. The non-amplified frequency-comb pulses are coupled out using polarizing beamsplitter cubes (PBS) with a total contrast

¹This type of fiber is chosen to suppress non linear effects that can occur due to the pulse peak power. Because the pulses are lengthened in time these non linear effects are already strongly suppressed.

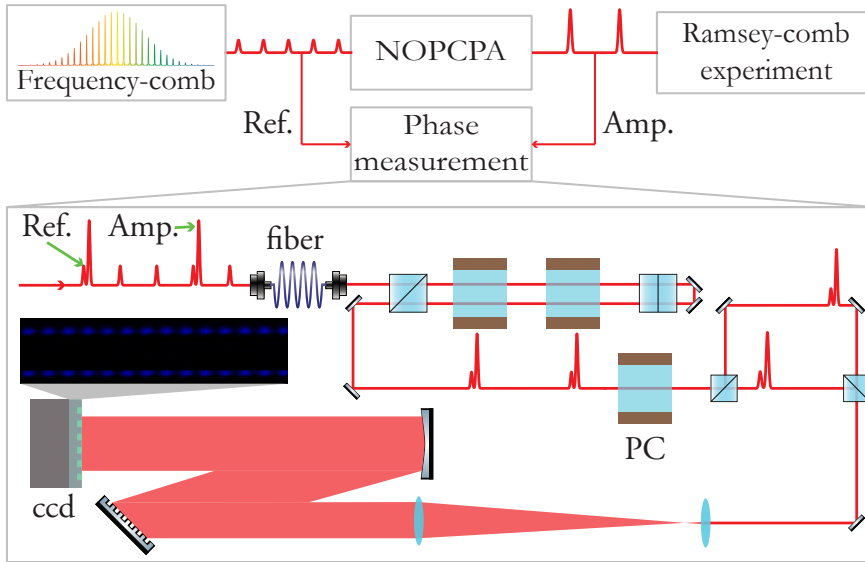


FIGURE 3.10: Overview of the phase-measurement setup. Pulses are split off the frequency comb before the NOPCPA and recombined with the amplified counterpart and coupled into a fiber. To select the amplified pulses and avoid background from the non-amplified comb pulses two Pockels cells are used in double pass configuration. Then a third Pockels cell is used to be able to project each pulse separately on a ccd-camera in a grating based spectrometer. Based on the spectral interference between the reference and amplified pulse the relative phase can be determined.

of better than 1000:1. In order to observe the phase from each pulse separately, an additional Pockels cell is then used to rotate the polarization of only one of the pulse pairs, which is again coupled out by polarizing beamsplitter cubes. The two paths are brought back together but with a slight vertical offset in order to project each pulse pair (original and amplified pulse) separately onto a camera. To observe the spectral interference a grating based spectrometer is used consisting of a 1200 lines/mm grating in combination with a high-sensitivity infrared ccd camera (IMI-TECH IMB-716-G), see Fig. 3.10. To increase the resolution the beam is enlarged to a FWHM of 2.5 cm, limited by the effective size of the grating. The frequency of the observed interference fringes can be adjusted by a manual delay stage situated in the arm of the reference pulses.

An example of an interferogram recording of a single pulse combination (e.g. first pulse with its reference) shown in Fig. 3.11 where in the top figure part of the ccd image is shown and in the bottom figure the integrated intensity. From each interferogram (belonging to the first and second excitation pulse) a phase can be extracted

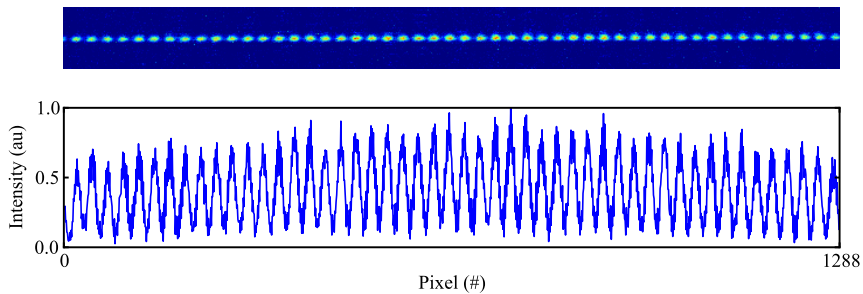


FIGURE 3.11: Example of a ccd camera image for the phase measurement. The first and second excitation pulse are projected separately in the vertical direction. Such a single frame is based on the interference of a single amplified pulse with its original frequency-comb counter part. The full width of the camera corresponds to a bandwidth of 4 nm

using a Fourier-transform based method and subsequently a phase difference can be determined [109, 110]. The optical path difference introduced in order to project each pulse separately onto the ccd camera, causes an additional phase shift between the projections. This phase shift can be calibrated out by interchanging the interference patterns by reversing the operation of the last (third) Pockels cell. With this technique the absolute phase difference between the two excitation pulses can be measured. Although we are primarily interested in the phase stability as function of time, and not so much the value of the absolute phase shift, it does provide a nice method to check that the NOPCPA is operated in the right regime.

An example of a phase measurement result conducted with this setup is shown in the upper part of Fig. 3.12. The measured phase difference is plotted as function of the delay time between the pulses where each delay is indicated by vertical bars. At each delay time the phase is measured for 750 laser shots and the projections of the first and second pulse are swapped every 50 laser shots. The result of the alternate switching of the interference patterns is clearly visible in the zoom-in of the bottom part of Fig. 3.12. The zoom-in shows the measured phase at a delay time of 79 ns, corresponding to a pulse separation of $\Delta N = 10$ in terms of the repetition rate of the laser. The real phase difference between the pulses is equal to half the phase difference between the difference projection states.

In Fig. 3.13 the averaged results of the true phase difference is plotted, and in this example the phase difference fluctuates around -168 mrad and the uncertainty of the measurement points is based on the variation within the data acquired for the data in Fig. 3.12. This measurement was taken for a center wavelength of 800 nm

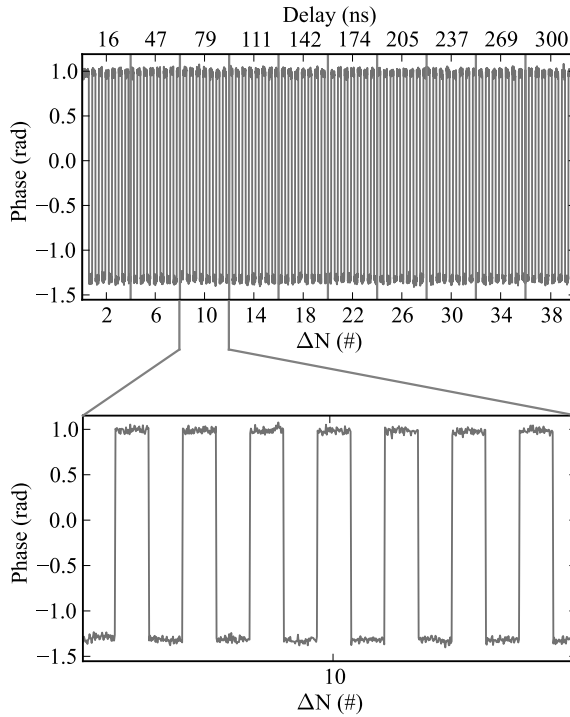


FIGURE 3.12: Results of a differential phase measurement at 800 nm wavelength and 2 nm bandwidth. The phase is measured as function of the time delay between the excitation pulses which is varied between 16 and 300 ns. Every 50 laser shots the interferograms are interchanged in order to calibrate the additional phase shift caused by the different optical paths of the projections on the ccd camera. In the bottom figure a zoom of the measured phase at $\Delta N = 10$ shows in more detail the swapping between the "up" and "down" projections.

Based on this data the true phase difference can be determined.

and a bandwidth of 2 nm, and showed no significant dependence on delay within the uncertainty of 6 mrad. There are several sources that can potentially influence the relative phase between the excitation pulses and they have to be treated carefully in order to keep the phase difference constant as function of time delay. In the next sections these potential sources of phase distortion are calibrated which is important for the results presented in Chapter 4 and Chapter 5.

3.5.1 Self reference calibration

The goal for the Ramsey-comb setup is to be able to increase the time delay between the excitation pulses as much as possible while keeping the relative phase difference as constant as possible. If the phase is not constant but, for example, the phase increases

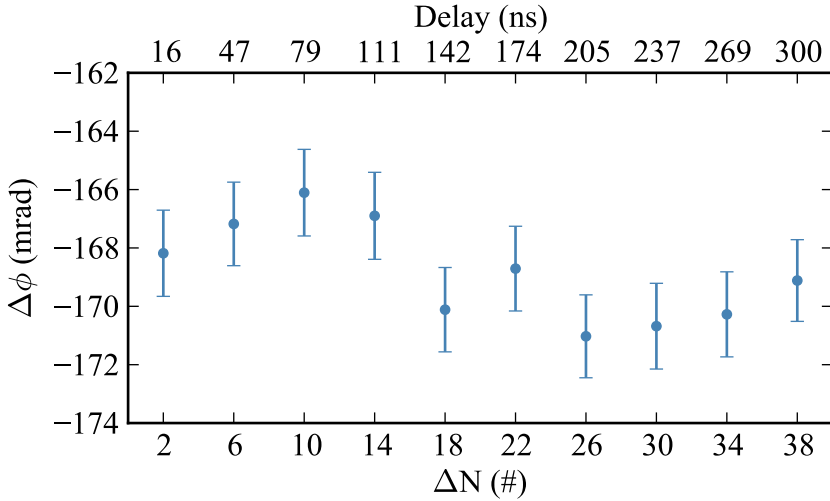


FIGURE 3.13: Example of a phase measurement result with a pulse delay up to 300 ns which. The absolute phase difference fluctuates around -168 mrad. Repeating such measurement shows that fluctuations are statistical and not systematic over the depicted time delay.

linearly with the delay time then this would lead to a frequency shift according to

$$\Delta f = \frac{\Delta\phi}{2\pi \cdot \Delta N \cdot T_{rep}} \quad (3.1)$$

where $\Delta\phi$ is the phase difference between the two excitation pulse pairs and ΔN is the delay time difference expressed in numbers of T_{rep} . If the transition that is investigated is at a harmonic of the fundamental laser light, or if a two-photon transition is probed, then also this has to be accounted for by multiplication with the effective harmonic. For example, if we probe a two-photon transition at 210 nm (the fourth harmonic of the fundamental) with a maximum delay time difference of $5 \times T_{rep} = 40$ ns, then a differential phase shift of just 5 mrad over this delay difference would lead to a frequency shift of 159 kHz. This simple calculation shows that we have to be careful when we take into account the influence of the optical phase shift.

Creating an amplified pulse pair with a time delay of a few microseconds (or even longer) is relatively straightforward. However, when the relative phase difference is measured some erratic behavior is observed, with phase differences on the order of 30 mrad after a time delay of approximately 400 nanoseconds, see Fig. 3.14. This was an unexpected result because there are no effects (to our knowledge) that should occur

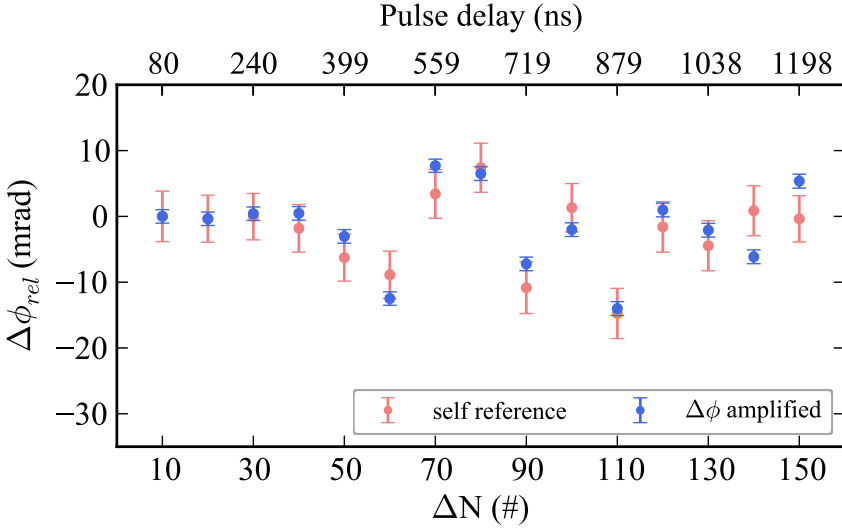


FIGURE 3.14: In blue the measured phase difference between the amplified excitation pulses as function of delay time. The phase is stable up to 450 ns delay time and then exhibits erratic fluctuations on the order of 30 mrad. In red the measured phase from the self-reference measurement. This measurement shows the same pattern indicating that the measured phase fluctuations are caused by the phase measurement setup itself.

at that specific delay time. In order to determine the cause of these phase variations much effort was put into identifying any correlation with experimental parameters such as ringing effects in the pulse picking sequence and the parameters of the Pockels cells used in the phase measurement setup. Because we were unable to determine any such correlation an additional setup was build to be able to perform a self-reference test to determine the influence of the phase measurement setup itself. This was achieved by building an additional Mach-Zehnder type interferometer in the reference arm using waveplates and polarizing beamsplitter cubes. This provides identical frequency comb pulse pairs for the phase measurement setup and should therefore produce a perfectly constant differential phase as function of time delay ². However, the measured phase difference again showed a similar erratic behavior as function of time delay, see Fig. 3.14. This result demonstrates that the measured phase differences after 400 ns delay time are actually produced in the phase measurement setup itself, and are not

²In this case all pulses are equal and the time delay no longer has any meaning. It is adjustment of the temporal gates of the Pockels cells in the phase measurement setup that now defines the time delay by picking pulse pairs.

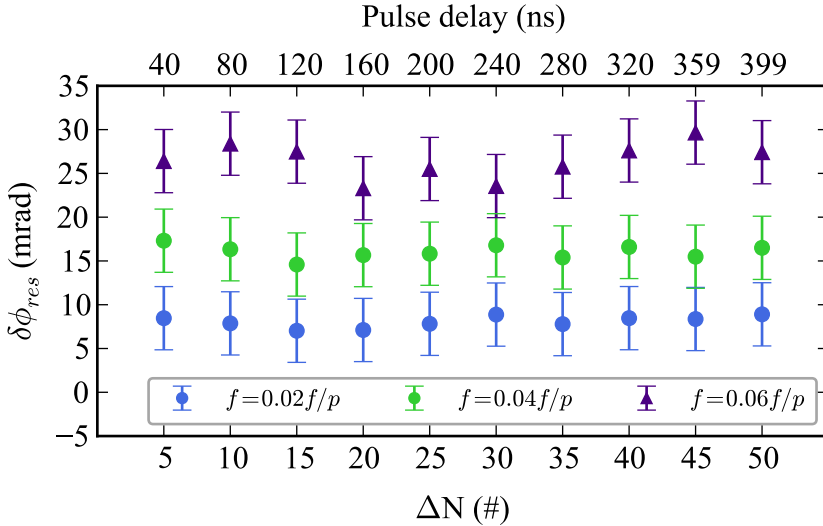


FIGURE 3.15: The measured phase difference as function of pulse delay from the self-reference measurement setup. The different colors are measurements for increasing fringe period (blue, green and purple) expressed in number of fringes per pixel on the camera. This graph illustrates that the time delay between the two interfering pulses leads to an additional absolute phase shift in the measurement, but importantly, does not influence the relative phase.

a result of the amplification process. The most likely cause for this effect is an additional phase shift that is introduced by the ringing of the high-voltage switching in the Pockels cells. In order to probe the phase over longer time delays this effects needs to be calibrated or removed from the measurement, but for the measurements presented in this thesis the time delay was not increased beyond 350 ns.

As it turned out there is another effect that influences the absolute phase difference, which is the time delay between the reference pulse and the amplified pulse, related to the observed period of the interference. Increasing the time delay between the two interfering pulses decreases the fringe period on the camera, leading to a higher potential resolution and a better statistical uncertainty. However, in the Fourier-analysis of the signal (to obtain the phase), the spectral fringe signal can be modified by spurious frequency components (e.g. due to additional pulses from beam splitters in the setup), leading to phase shifts. This we try to avoid by selecting the right interference period. Still, Fig 3.15 shows a dependence of the measured self-reference phase for increasing fringe period (expressed in fringes/pixel) indicated by the blue, green and purple data points. It is clear that the absolute measured phase increases for a longer time delay between the reference and amplified pulse. Also this effect

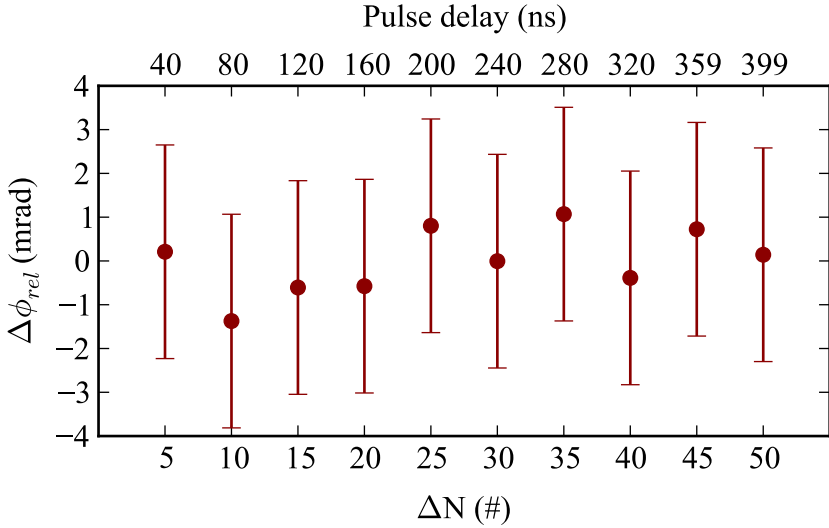


FIGURE 3.16: Self-reference phase measurement that demonstrates that the results of the phase measurement are not influenced by the setup itself up to a pulse delay time of 300 ns.

is most likely related to the operation of the Pockels cells. Because we select single pulses from the pulse train the temporal gate of the Pockels cell is as short as can be generated by the drivers. By increasing the time delay between the laser pulses they will probe a different part of the temporal evolution of the Pockels gate, leading to a small but significant phase shift.

Although there can be an additional phase shift as function of the time delay between the reference and investigated pulse, this phase shift is constant as function of time delay, see Fig. 3.16. We therefore conclude that up to pulse delays of 400 ns the phase measurement setup itself has no influence on the differential phase as function of time delay. Phase measurement beyond this time delay will require more careful evaluation to disentangle the influence of the amplification process and phase measurement setup. It is expected, however, that there is no real significant phase distortion after 400 ns but based on the available data it cannot be excluded.

3.5.2 Influence of the pump pulse intensity on the phase in the NOPCPA

Analytic solutions to the coupled wave equations describing parametric amplification (Eqs. 2.18) can be obtained in certain limiting cases [111–113]. One can find solutions

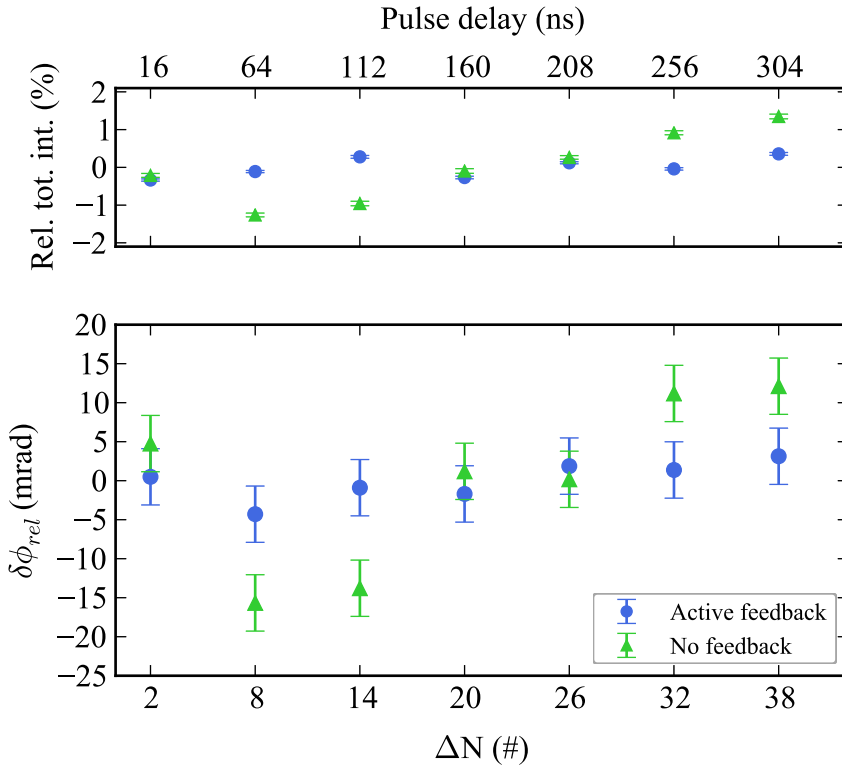


FIGURE 3.17: In the upper graph the combined energy the amplified frequency-comb pulses is plotted (relative to the first data point) as function of delay time, and the bottom graph shows the corresponding relative phase shift. For the triangular (green) data points no feedback was applied to stabilize the NOPCPA output and therefore the pulse energy changes as function of delay time. As a result the measured phase shift as function of delay time varies by more than 20 mrad. By applying active feedback through the pump pulses of the NOPCPA this effect can be controlled to the level of 5 mrad indicated by the round (blue) data points. These measurements were performed by operating the NOPCPA with a bandwidth of 2 nm.

for the evolution of the phase of the interacting beams during the amplification process. As it turns out the phase of the signal beam is independent of the phase of the pump beam. However, while the phase of the pump hardly contributes, the intensity of the pump pulses can influence the phase of the signal beam [111, 114]. Fortunately, the frequency extracted from a Ramsey-comb measurement is not influenced by an absolute phase offset. This means that the relative phase "only" needs to stay constant as function of the delay time. Nonetheless, these phase shifts can potentially influence the measurements as is illustrated in Fig. 3.17. In this figure the top graph shows the relative amplified frequency-comb pulse intensity and the bottom figure

the measured relative phase difference, both as function of time delay. The measurement was repeated for two different situations. The first, indicated by the green data points, is a measurement where the system is "free running", i.e. there is no active stabilization on the pulse energy of any kind. The second situation, indicated by the blue data points, is a measurement where the pulse energy is actively stabilized both relative to each other as well as the total energy of the pulses combined. These graphs clearly demonstrate that there is a correlation between the pulse energy and the measured phase that can lead to significant systematic frequency shift in a Ramsey-comb measurement.

To further investigate the correlation between the phase and the intensity of the pump pulses, measurements were taken at a fixed delay time while the relative intensity or total intensity of the pump pulses was varied. The results of these measurements are shown in Fig. 3.18. In this figure the left plot shows the measured phase difference as function of the relative pulse energy of the excitation pulses. Varying this relative intensity is achieved by changing the intensity of first pump pulse of the NOPCPA (see Section 3.3.3). There is a clear correlation between the relative phase and the change of the pulse ratio. Here we observe 2 mrad phase shift per 1% energy difference, assuming a linear relation. Similarly, the total intensity of the NOPCPA output can be modulated by adjusting both pump pulses at the same time, which can be achieved by adjusting the total gain of the post amplifier. The phase shift as function of the relative total intensity is plotted in the right graph of Fig. 3.18. The blue line is a linear fit to the data and indicates a -24 mrad phase shift per 1% change in total energy and we therefore have to carefully stabilize our pulse energy to avoid such phase shifts in the experiment. The magnitude of these phase shifts can vary from day to day because it depends on the exact alignment (inducing phase mismatch effects, as well as cross-phase modulation variations) of the NOPCPA. These measurement indicate that it is crucial to maintain a stable pulse energy in order to avoid phase shifts that can influence the frequency determination. Based on these measurements, data points for which the total pulse intensity deviated more than 0.25% compared to the average were discarded from the analysis.

3.5.3 Spectral dependence of the phase

Another aspect, particularly important for the measurements presented in Chapter 4, is the spectral dependence of the relative phase difference. Because of the dynamics and saturation effects in the NOPCPA the spectrum of the amplified frequency-comb pulses is not Gaussian or square but instead has a 'cathedral' shape (two peaks at the end, and a plateau in the middle). As a result the interferograms that are captured

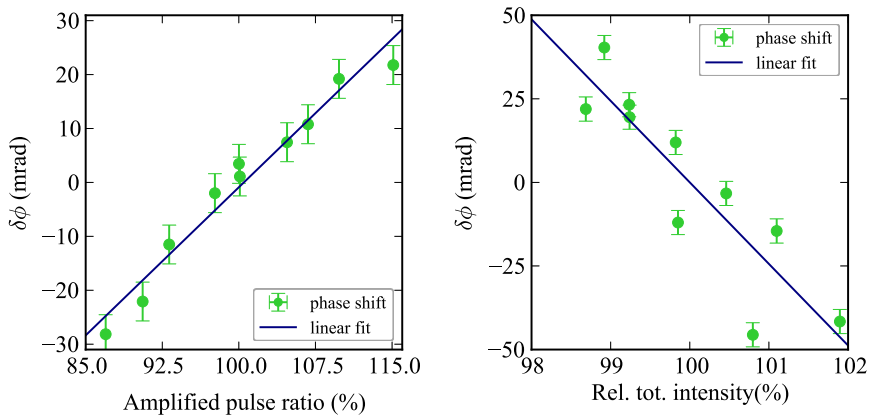


FIGURE 3.18: In the left graph the phase difference between the excitation pulses is plotted as function of relative intensity of the amplified frequency-comb pulses at a fixed time delay. There is a clear correlation between the pulse ratio and the measured phase shift and fitting the data with a straight line indicates a phase change of 2 mrad/1% energy difference. This magnitude of this slope may vary depending on the alignment of the NOPCPA, in part due to residual phase mismatch and due to cross phase modulation from the pump beam. In the right graph also the phase difference at a fixed time delay is plotted, only here as function of the total output of the NOPCPA. Again a clear correlation is observed, and from this measurement phase change of -24 mrad per 1% change in output energy is measured. The data of the right plot was acquired as a quick check of the effect; as a result the conditions were less well controlled and the error bars as shown are most likely underestimated.

in the phase measurement also poses this additional modulation, see the top part of Fig. 3.19. In fact, the higher intensity edges of the spectrum are used for the experiments in krypton (see Chapter 4), and it is therefore important to establish that the phase is constant in these extreme circumstances. To increase the signal-to-noise ratio, the intensity of the amplified pulses is measured separately before each phase measurement and subtracted as background signal to obtain a more flat interferogram, see bottom part of Fig. 3.19. The interferogram presented in this figure is for ~ 3.5 nm wide bandwidth, centered around 852 nm ³.

To determine the phase stability for each part of the spectrum, the left, center and right part are analyzed separately. The different parts of the spectrum are indicated by the solid background color in Fig. 3.19, red, green and blue, respectively. In Fig. 3.20 the obtained phase difference as function of pulse delay is plotted for each part of the spectrum and in addition for the complete spectrum in grey. Within the statistical uncertainty there is no difference in the behavior of the phase for different parts of the

³Based on separate measurements with an Ando optical spectrum analyzer.

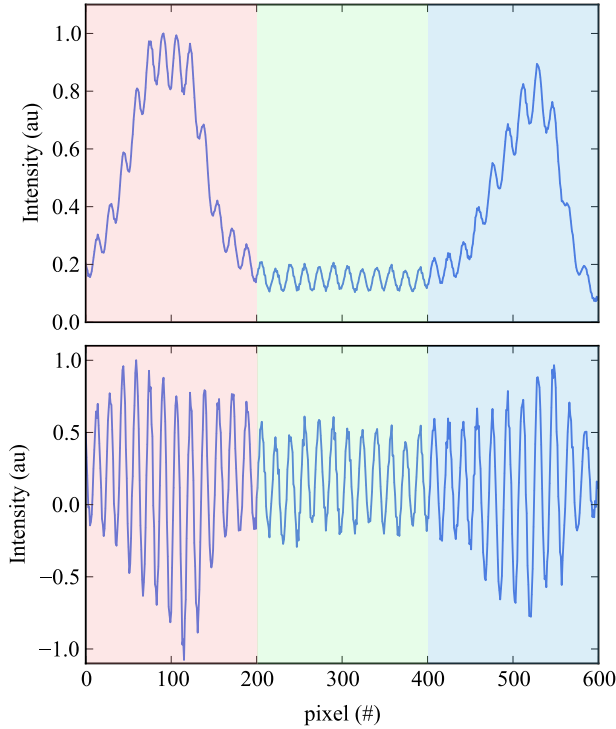


FIGURE 3.19: Top figure: Interferogram as recorded by the camera in the phase measurement setup. The double peak structure of the spectrum from the amplified pulses is clearly visible. The interference with its non-amplified counterpart is superimposed on top of the double peak structure. Bottom figure: To obtain a cleaner signal the intensity from the amplified pulses is recorded separately and subtracted from the measured interferogram, which is depicted in the bottom figure. There is still a slight modulation visible because the intensity at the edges of the spectrum is less stable than in the center and therefore the background from the amplified pulses is not always perfectly canceled. To determine if the phase behaves different at the edges than in the center the analysis was done on separate regions indicated by the red, green and blue shaded areas, see Fig. 3.20.

spectrum. The uncertainty for the separate parts of the spectrum is slightly larger due to the fact that less fringes contribute to the signal, which decreases the signal-to-noise ratio. This result shows that despite the strong saturation effects leading to significant different behavior across the spectrum, the relative phase remains constant across the spectrum of the amplified pulses as function of time delay.

3.6 Conclusion

To conclude, in this chapter a detailed overview of the Ramsey-comb laser system is presented. The laser system provides an amplified frequency-comb pulse pair up to a

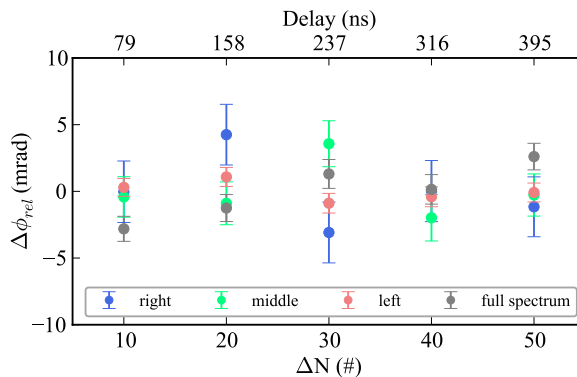


FIGURE 3.20: Phase measurement results for different parts of the spectrum for the same data set. The part of the spectrum is indicated by the different colors (see Fig. 3.19). This measurement shows that there is no significant difference in the behavior of the relative phase difference across the spectrum despite the different influence of the NOPCPA on the different parts of the spectrum.

pulse energy of 2 mJ with an adjustable time delay. The time delay can be adjusted on two time scales; in incremental steps at the repetition time (7.9 ns) by selecting different pulse pairs, and on a much shorter timescale (~ 100 attoseconds) by small adjustments of the repetition time of the frequency-comb and pump laser. In addition, the pulses are produced in such a way that the relative phase remains stable as function of the time delay, a crucial property for Ramsey-comb spectroscopy. We have presented details of the phase measurement setup and shown that for delay-times below 400 ns the phase-measurement itself has no influence on the results. For longer delay times the electronic switching of the Pockels cells in the setup influences the results and therefore requires more careful analysis and further investigation to extend beyond this value. Also the influence of the pump pulse energy on the phase of the amplified frequency comb pulses is calibrated. These properties are carefully monitored in order to obtain a stable phase during the Ramsey-comb measurements presented in this thesis. In addition, the wavelength dependence of the phase in the parametric amplification process is considered. Despite strong differences in behavior across the spectrum the phase remains stable as function of the pulse delay time.

High-precision Ramsey-comb spectroscopy on the two-photon

$4p^6 \rightarrow 4p^5 5p[1/2]_0$ transition in krypton at 212.55 nm

4.1 Abstract

High-precision spectroscopy in systems such as molecular hydrogen and helium ions is very interesting in view of tests of Quantum Electrodynamics (QED) and the Proton Size puzzle. However, the required deep-ultraviolet and shorter wavelengths pose serious experimental challenges. Here we show Ramsey-comb spectroscopy in the deep ultraviolet for the first time, thereby demonstrating its enabling capabilities for precision spectroscopy at short wavelengths. We excite ^{84}Kr in an atomic beam on the two-photon $4p^6 \rightarrow 4p^5 5p[1/2]_0$ transition at 212.55 nm. It is shown that the AC-Stark shift is effectively eliminated, and combined with a counter-propagating excitation geometry to suppress Doppler effects, a transition frequency of 2,820,833,101,679(103) kHz is found. The uncertainty of our measurement is 34 times smaller than the best previous measurement, and only limited by the 27 ns lifetime of the excited state.

4.2 Introduction

Quantum Electrodynamics (QED) theory is a cornerstone of the Standard Model and one of the best tested fundamental theories in physics. Its predictions have been verified with extreme precision, e.g. by measuring the fine structure constant α derived from measurements of the electron g-factor [16, 27], interferometric recoil experiments [115, 116], and bound-state QED tests based on precision spectroscopy in atoms, molecules and highly-charged ions (see e.g. [21, 100, 117–121]). In fact, QED-theory for atomic hydrogen has now become so accurate and the spectroscopic experiments so precise (made possible by the advent of the frequency-comb laser), that the limiting factor in the comparison between theory and experiment is the uncertainty in the proton-charge radius (r_p), and the Rydberg constant (R_∞). In pursuit of testing QED

ever better, substantial efforts have been made to extract the fundamental quantities r_p and R_∞ from the spectroscopy of atomic hydrogen. However, when the CREMA collaboration determined the proton charge radius from spectroscopy in muonic hydrogen (consisting of a proton and a muon), it led to a considerable (5σ to 7σ) mismatch with the value extracted from normal (electronic) hydrogen [28, 29, 122]. This discrepancy between experiment and theory is now commonly known as the *proton-charge radius puzzle* and is enforced by recent results on muonic deuterium that reveal that also the deuteron radius is significantly smaller (7.5σ) than the radius based on electronic deuterium spectroscopy [36].

One approach to solve this puzzle is based on measuring more transition frequencies in muonic and electronic hydrogen. In particular more measurements in electronic hydrogen are helpful to obtain an improved value for the Rydberg constant (see e.g. [117, 118, 123]), to disentangle the influence of this constant and the finite proton size effect. Also spectroscopy of muonic helium ions is pursued [122] to test the finite size effect of a different nucleus. In view of these efforts two more systems are particularly interesting: 1S-2S spectroscopy in electronic helium ions [46, 122], and spectroscopy of *molecular* hydrogen [51, 124]. Molecular hydrogen has also been used recently for searches of physics beyond the Standard Model, such as possible fifth forces [125]. In both systems the challenge is the short wavelengths required for electronic excitation from the ground state: deep-UV for H_2 , and extreme-UV (XUV) for He^+ , where no narrow-band laser sources or frequency combs are available.

To overcome this challenge, nonlinear optics with frequency-comb lasers is pursued to directly excite transitions with an upconverted comb laser [62, 100]. The typical pulse energy of a few nJ of most comb lasers is not sufficient for that. One approach to increase the energy is based on full-repetition rate amplifiers and enhancement resonators to reach the required μJ -level pulse energy for intra-cavity high-harmonic generation (HHG) [60–62]. Alternatively, one can amplify only two pulses from a frequency comb laser for HHG [100]. This can lead to more efficient wavelength conversion and to higher two-photon transition probabilities. If then pulse pairs at multiple delays can be selected, precision spectroscopy via the Ramsey-comb method becomes possible [67] with orders of magnitude higher pulse energy (mJ/pulse in the IR and tens of μJ /pulse in the UV) than achievable with full repetition rate based methods. Previously we demonstrated these properties for near-infrared two-photon transitions of rubidium in a gas cell, showing that even with only two pulses, the accuracy and resolution of frequency combs can be recovered [67, 68].

In this chapter we demonstrate that Ramsey-comb spectroscopy can be extended to

much shorter wavelengths in the deep-UV for the first time. This is illustrated by a 34-times improved frequency measurement in an atomic beam on the $4p^6 \rightarrow 4p^5 5p[1/2]_0$ two-photon transition in ^{84}Kr at $\lambda_c \approx 212.55$ nm.

4.3 Ramsey-comb method

Ramsey-comb spectroscopy is based on a series of measurements using only two phase-coherent pulses from a frequency-comb laser. Frequency comb lasers are ideally suited for this purpose as they produce an infinite train of pulses with a well defined repetition time (T_{rep}) and phase relation ($\Delta\phi_{ceo}$) between subsequent pulses. In the following description we assume excitation of a two-level atom with a transition frequency f_{tr} . Excitation with two selected comb laser pulses resembles Ramsey's method of separated oscillatory fields, which is the basis of most atomic clocks in the radio-frequency and optical domain [65, 126]. Each excitation pulse induces a superposition of the ground and excited state. Quantum interference between the two excitation contributions then leads to an excited state population (ρ_{22}) which depends on the exact time delay (Δt) and optical phase shift ($\Delta\phi$, including $\Delta\phi_{ceo}$) between the two excitation pulses:

$$\rho_{22}(\Delta t) \sim \cos(2\pi f_{tr} \Delta t + \Delta\phi) \quad (4.1)$$

By probing the excited state population as a function of Δt , traditional Ramsey-fringes are observed from which the transition frequency can be determined. One issue with Ramsey spectroscopy is a possible spurious phase shift in the excitation pulses that is not accounted for [63, 100]. With frequency comb lasers this issue can now be solved in an elegant way if pulse pairs are selected at *different* multiples of the repetition time of the frequency-comb laser. One can then record signals at a series of delays equal to

$$\Delta t = \Delta N \cdot T_{rep} + \delta t \quad (4.2)$$

where ΔN is an integer. To record a Ramsey signal at each ΔN , the repetition time of the laser is scanned by a small amount δt . Combined with the larger time steps by changing ΔN this results in a series of recordings that together forms the "Ramsey-comb" signal [67]. The advantage of comparing signals from multiple pulse pairs is that any constant phase shift as function of ΔN can be identified as a common influence. Therefore it can be eliminated from the transition frequency determination even if the absolute value is unknown, which greatly enhances the accuracy. If the pulse energy is kept constant as a function of ΔN , the AC-Stark shift from the excitation pulses also manifests itself as a constant phase shift of the Ramsey signals, which can therefore be

eliminated as well. Moreover, similar to traditional Ramsey spectroscopy, the accuracy of Ramsey-comb spectroscopy becomes better for longer time delays.

4.4 Experimental setup

Experimentally, we create high-intensity pulse pairs by parametric amplification of pulses from a Kerr-lens mode-locked Ti:sapphire frequency-comb laser (see Fig. 4.1). The repetition frequency ($f_{rep}=126$ MHz) and carrier-envelope offset frequency ($f_{ceo} = \Delta\phi_{ceo}f_{rep}/2\pi$) of the comb laser are both referenced to a cesium atomic clock for absolute frequency and time calibration.

In a stretcher the pulses from the comb laser are spectrally clipped to 3 nm around 850.2 nm and chirped by $1.2 \cdot 10^6$ fs² of 2nd order dispersion to produce 12 ps pulses. These pulses seed a noncollinear optical parametric chirped-pulse amplifier (NOPCPA) where selectively two frequency-comb pulses are amplified up to 1.7 mJ. The two 75 ps pump pulses at 532 nm wavelength for the NOPCPA are produced with a separate, synchronized laser system (see [69, 105]).

The sharp spectral clipping of the seeding beam results in a sinc-like pulse in the time domain. The wings of the sinc are strongly amplified in the NOPCPA operating in a saturated regime, and because we use chirped pulses, the amplification in the wings of the pulses corresponds to an enhanced amplification of the "red" front edge and the "blue" trailing edge of the pulse. This results in a spectrum with two peaks at the edges of the spectrum as shown in Fig. 4.2. It also leads to a separation in time of the two spectral regions and increases the total amplified pulse duration to approximately 20 ps.

Deep-ultraviolet generation

The amplified frequency-comb pulses are frequency upconverted using three β -barium-borate (BBO) crystals, producing up to 45 μ J/pulse at 212.55 nm. The resulting deep-UV beam is split in equal parts by a metallic beamsplitter. This enables to excite the two-photon transition in a counter-propagating laser beam configuration so that the first-order Doppler shift is reduced. The collision point of the excitation pulses is overlapped with an atomic beam based on a pulsed supersonic expansion of krypton atoms. The direction and divergence of the atomic beam is determined by a skimmer, 4-5 cm from the nozzle with a circular opening 0.5 mm, and a subsequent

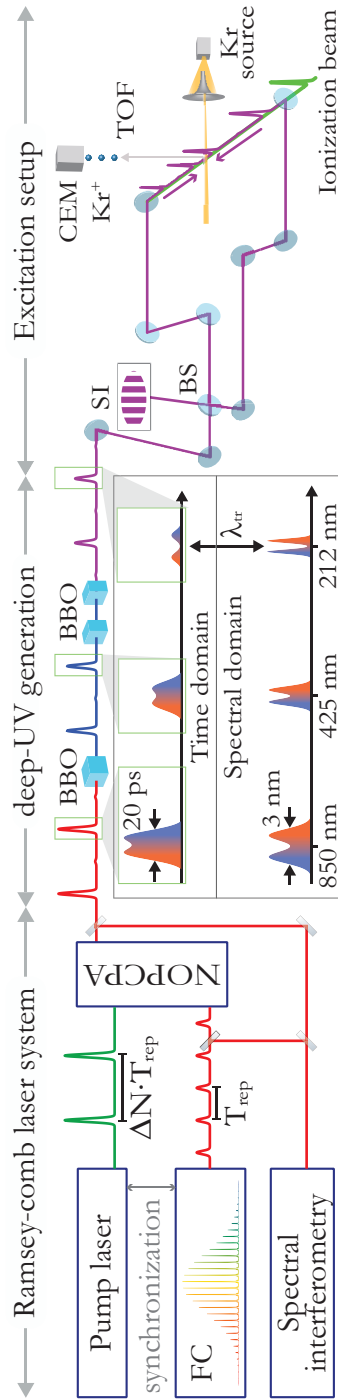


FIGURE 4.1: Schematic overview of the setup. Frequency-comb (FC) pulse pairs are amplified in a non-collinear optical parametric chirped-pulse amplifier (NOPCPA). Spectral interferometry is used to measure the differential phase between the amplified and original frequency-comb pulses. The amplified pulse pairs are upconverted sequentially using three BBO crystals, and the two insets show the spectral and temporal evolution of each Ramsey comb pulse, starting with the original near-infrared spectrum and ending with a "red-blue" split pulse in the deep UV near $\lambda_{\text{tr}} = 212.55$ nm. The UV beams are aligned exactly counter propagating using the fringes observed at the output of the metallic 50% beamsplitter (BS), which acts as a Sagnac interferometer (SI). After excitation, the krypton atoms are ionized and extracted upwards in a time-of-flight (TOF) drift tube and detected with a channel-electron multiplier (CEM, EDR-model from Dr. Sjuets).

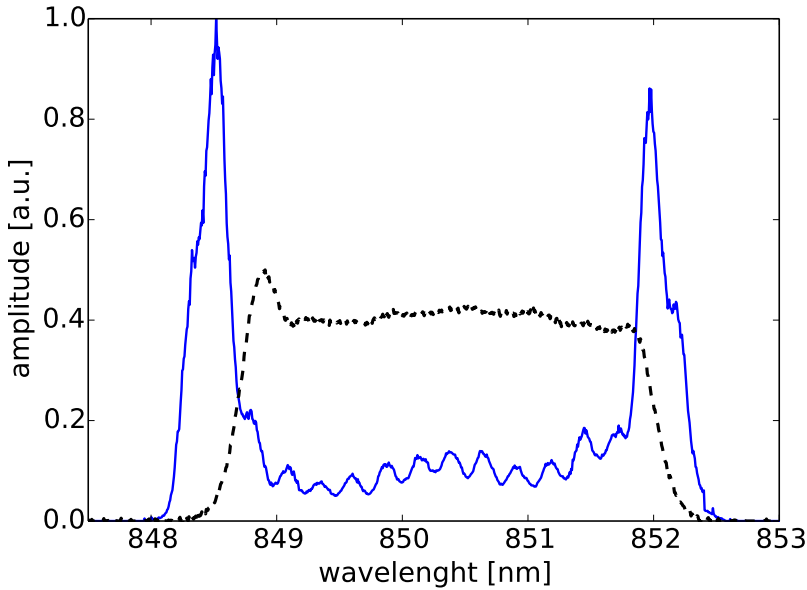


FIGURE 4.2: Spectrum of the selected FC spectrum before amplification (in black dashed line) and after amplification (solid blue line) in the NOPCPA. The oscillations in the amplified spectrum are an artifact, caused by mode beating in the fiber that was used to record the spectrum

slit of 3 mm width ¹. After the excitation pulses, an ionization pulse at 532 nm is applied which only ionizes krypton atoms that are in the excited state. The resulting ions are extracted with a pulsed electric field to enable field-free excitation. A time-of-flight drift tube is then used in combination with a channel-electron multiplier (CEM) to separate and detect the different isotopes with a mass resolution of $m/\Delta m = 212$ (FWHM), see Fig. 4.3. Each isotope is measured individually with a Boxcar integrator (Stanford Research), and the whole experiment is repeated at a rate of 28.2 Hz.

Excitation geometry

With two counter-propagating ultrafast laser pulses, the two-photon transition can still be excited from just one side, leading to calibration errors and reduced signal contrast. This signal can be suppressed by strongly chirped pulses [127, 128], or more effectively by circularly polarized light, or a combination of both [67]. However, purely circularly

¹In retrospect this atomic beam geometry is not ideal. Because the nozzle relatively close to the skimmer the clogging effect will cause the skimmer to act as a secondary source leading to a decreased density. A better geometry (implemented in future experiments) is to use a larger skimmer (± 2 mm) at a much larger distance (± 20 cm)

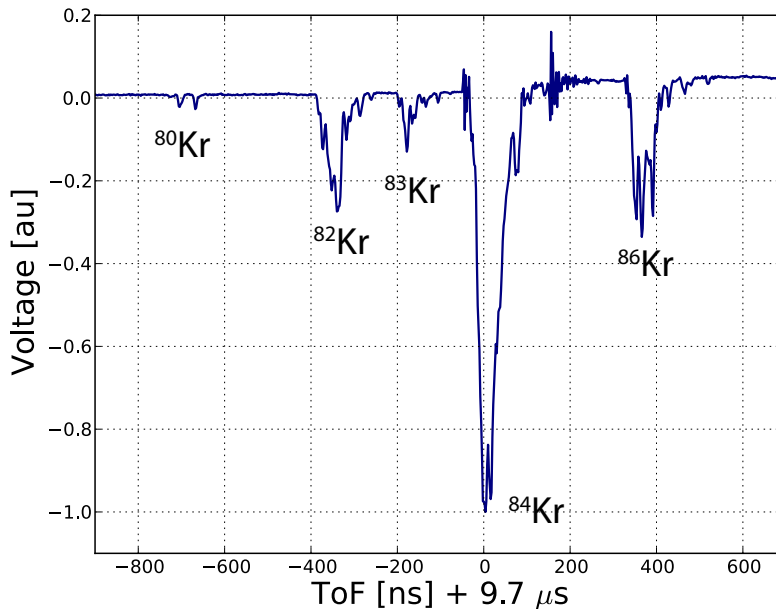


FIGURE 4.3: Typical Time-of-Flight detection of the isotopes of krypton. The relative signal depends on the state of the phase of their respective Ramsey oscillation. We have chosen a time-of-flight snapshot which pattern is a close representation of their natural abundance. The large signal of the most abundant isotope ^{84}Kr strongly affects the operation of the detector, and therefore the signal of isotopes arriving later. This effect can also be seen as a shift of the detector signal baseline after ^{84}Kr .

polarized light is difficult to achieve for deep-UV ultrafast laser pulses. Therefore we use an alternative approach with linear polarized light pulses that are split in two parts, a "red" and a "blue" part relative to the transition frequency [128]. Combined with chirp in the pulses, their time evolution is also split in a "red" and "blue" part. With this temporal and spectral shape the transition can only be excited when the "red" and "blue" parts of the pulses overlap from opposite sides, thereby fully suppressing excitation by a single side.

Experimentally this is realized by nonlinear upconversion of the chirped fundamental pulses in three consecutive nonlinear crystals (see Fig. 4.1). In the first BBO crystal (1.0 mm thick) the full bandwidth of the fundamental pulse is frequency doubled to ~ 425 nm. The second doubling stage, to the deep-UV, is split up over two separate crystals. The thickness of these crystals (0.5 mm) is chosen such that the phase-matching condition is limited to a narrow spectral range (< 0.5 nm). Each crystal is only phase matched at one edge of the spectrum so that a double-peak structure

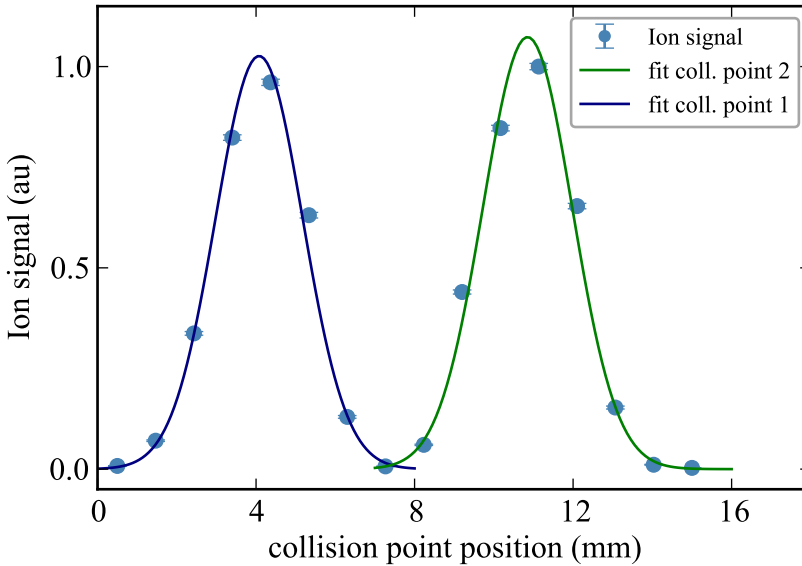


FIGURE 4.4: Measurement of the krypton ion signal as function of the position of the collision point. The collision point of the deep ultraviolet pulses is moved by adjusting a translation stage in one of the arms of the counter propagating beams. Because of the large chirp on the pulses and the frequency upconversion geometry we are able to observe two separate collisions points. This is an effective way to eliminate single side background signal without additional optics in the ultraviolet.

is created in the deep-UV with zero intensity at the two-photon resonance. Because of the large chirp introduced by the stretching, the temporal shape of the laser pulses will have a similar double-peak structure with the "blue" edge of the spectrum trailing the "red" edge (see in Fig. 4.1). The spatial separation of the two colors (~ 6.5 mm, equivalent to 21 ps) is larger than the width of the atomic beam (~ 3 mm), so we are able to observe the two collision points separately (where "blue" meets "red" and vice versa). This is illustrated in Fig. 4.4 where the ion signal is plotted for as function of the position of the collision point. The position of the collision point is changed by moving a translation stage that is mounted in one of the arms after the beam-splitter. We clearly see the two separate appearances of the split ultraviolet pulses, demonstrating the efficiency in removing the background signal using the split pulse technique.

4.5 Ramsey signals at 212 nm

Using this setup Ramsey-comb signals for the ^{84}Kr isotope have been recorded up to eight times the laser repetition time of 7.9 ns. Only a single transition is resonant within the bandwidth of the laser pulses, therefore measuring Ramsey signals at two different ΔN suffices to eliminate common phase shift effects and determine the transition frequency. We start at $\Delta N = 2$ to avoid transient effects, while the longest delay is typically chosen at $\Delta N = 7$ for optimal signal-to-noise ratio given the upper-state lifetime of ~ 27 ns. At each ΔN the repetition time of the laser is scanned over several hundreds of attoseconds to observe roughly two oscillation periods of the Ramsey signal (see Fig. 4.5). Each Ramsey measurement consists of 15 points as a compromise between fast data acquisition to avoid systematic drifts and enough points to properly fit the data. A complete Ramsey-comb measurement requires about 6 minutes of acquisition time and such a recording is performed in a "back and forth" sequence. This means that the even number data points at $\Delta N = 2$ and $\Delta N = 7$ are recorded first, followed by the odd-numbered data points at $\Delta N = 7$ and $\Delta N = 2$ in reversed order. This sequence is adopted to suppress the influence from systematic drifts such as beam pointing. In the ideal case all data points would be sampled in complete random order, however, it is experimentally undesirable to make large jumps in the laser repetition time because it then takes more time for the repetition time to stabilize. In fact, to avoid such transient effects the first 35 data points after each change in repetition time are always removed from the analysis.

The fitting and frequency determination from a Ramsey-comb measurement is done purely on the phase of the recorded time-domain signals as explained in [67, 68]. In this particular case we are resonant with only a single transition and it therefore suffices to measure only two Ramsey fringes because the phase evolves linear for a single frequency. However, analogous to direct frequency-comb spectroscopy, in Ramsey-comb spectroscopy the frequency is extracted modulo the sampling interval, which in this particular case (measuring $\Delta N = 2$ and $\Delta N = 7$) is five times the fundamental laser repetition time, corresponding to 25.2 MHz. This ambiguity can be resolved by performing measurements at different repetition rates. However, in this case the transition frequency is known accurately enough from previous measurements to avoid such ambiguity [63].

The statistical uncertainty of a frequency measurement from the fit is based on the uncertainty of the individual measurement points, which in turn is determined by the signal fluctuations over approximately 350 laser shots, again a compromise between fast acquisition and signal-to-noise ratio. The 1σ statistical uncertainty for

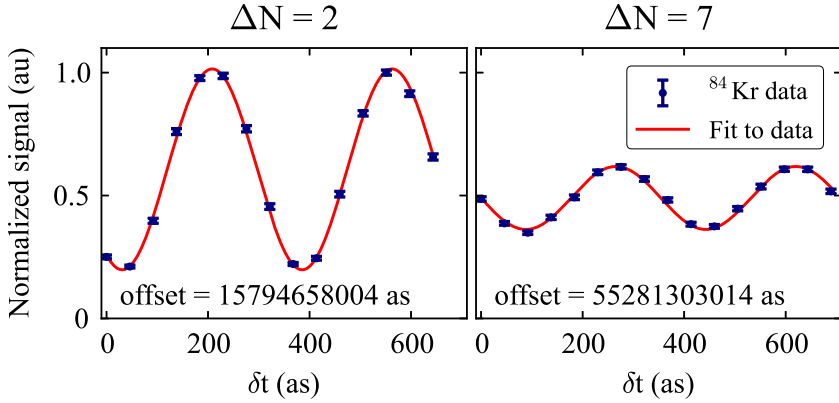


FIGURE 4.5: Example of measured Ramsey-signals at $\Delta N = 2$ and $\Delta N = 7$. At each ΔN the delay time is scanned over ~ 700 attoseconds (as) and is offset by $\Delta N \cdot T_{rep}$ (see Eq. (4.2)) corresponding to 15.79 ns and 55.28 ns respectively as indicated in the figure. Each data point is an average over 350 laser shots and the variation within this set is used to determine the statistical uncertainty of the data points. The signal is normalized to the maximum signal of the first Ramsey fringe. The red line is a fit to the data based on Eq. (4.1).

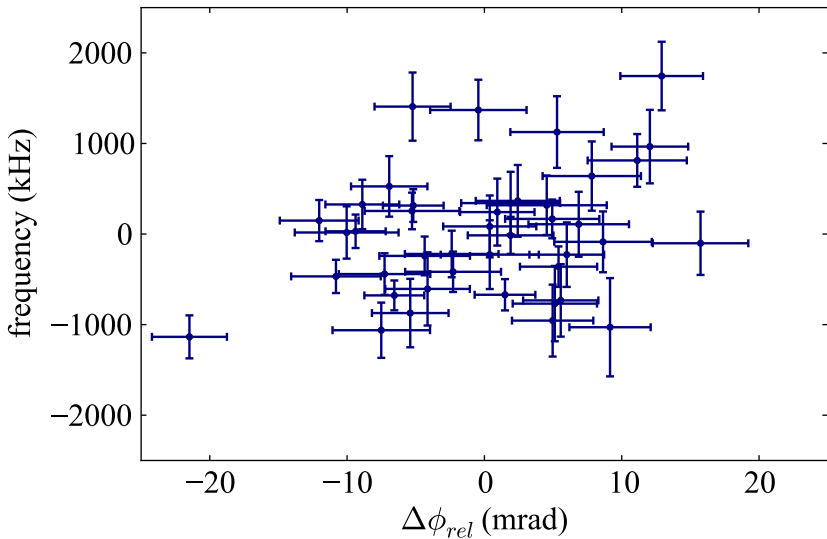


FIGURE 4.6: Correlation between the measured phase difference (x-axis) and the variation of the measured transition frequencies. No clear correlation is present between between the measured phase shift and the determined transition frequency.

one such a Ramsey-comb measurement is around 150 kHz. However, if the transition frequency is measured over a longer period of time the fluctuations of the results are larger, by a factor of 1.85, than the 1σ uncertainty based on the short term variation within one measurement. In order to determine if there is any underlying systematic effect, much effort has been made to correlate these fluctuations with the parameters of the experimental setup. One important parameter is the phase difference of the excitation pulses. Fig. 4.6 shows the variation of the measured transition frequency (on the y-axis) as function of the the measured phase difference (on the x-axis). From this figure we conclude that possible variations in the relative phase between the excitation pulses are not the cause for the observed frequency fluctuations. Similar results were obtained for correlations with beam pointing of the ultraviolet beam, intensity fluctuations of the excitation pulses and temperature. One parameter that cannot be controlled with a high degree of precision is the density of the atomic beam. Fluctuations in the density on a time scale comparable or longer than the acquisition time of a single measurement could potentially lead to small distortions of the Ramsey signal. Taking into consideration the fact that no correlation with any other experimental parameter could be discovered we conclude that the nature of the fluctuations is purely statistical. To properly account for the true statistical uncertainty of a single Ramsey-comb measurement the uncertainty was increased by a Birge factor of 1.85 which was determined from the variation of the measured transition frequencies.

4.6 Calibration of systematic effects

Apart from the statistical uncertainty of each single measurement, any effect that systematically shifts the measured frequency has to be considered carefully. For this experiment there are several potential sources of such a shift that are discussed separately below.

4.6.1 Doppler shift

A misalignment of the laser beams with respect to the atomic beam, or a residual angle between the counter-propagating laser beams both lead to a residual Doppler shift. Therefore we align the deep UV beams as parallel as possible by monitoring the light transmitted through the beamsplitter. This configuration forms a Sagnac interferometer, and with perfect alignment complete extinction is observed at the output [129]. A residual first-order Doppler shift can then still be present due to chirp of the excitation pulses, depending on the trajectory of the atoms through the

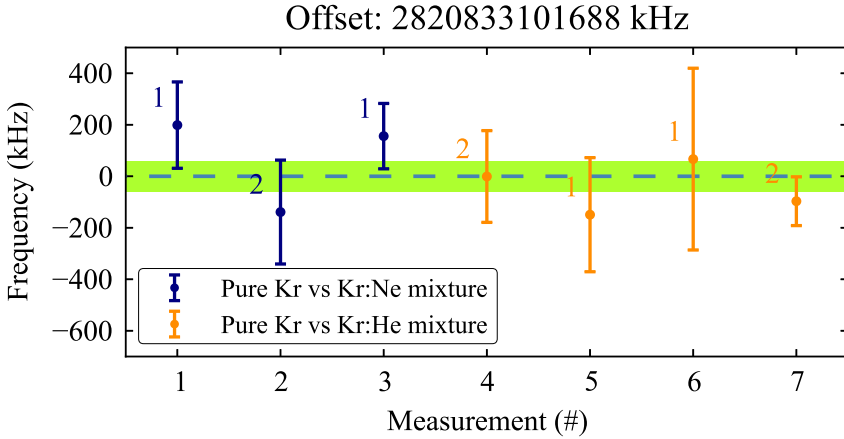


FIGURE 4.7: Measurement results of the $4p^6 \rightarrow 4p^5 5p[1/2]_0$ transition frequency in ^{84}Kr . Each data point is an average over ten to twenty Ramsey-measurements at macro delays $\Delta N = 2$ and $\Delta N = 7$, and the green band shows the 1σ uncertainty of the average. The first-order Doppler shift is determined by measuring the transition frequency difference for pure Kr with respect to Kr:Ne and Kr:He mixtures. The color indicates which noble gas was used to speed up the supersonic expansion, and the numeral which collision point was used.

laser beams [117]. However, this effect and other Doppler effects are minimized with a procedure based on measuring the transition frequency for different velocities of the atomic beam while adjusting the angle between the laser beams and the atomic beam until no more Doppler shift is observed. For this procedure the speed of the atomic beam was increased by mixing pure krypton (380(30) m/s) with at least five times more neon or helium, leading to a Kr velocity of 686(60) m/s and 931(134) m/s respectively. By extrapolating the measured transition frequencies to zero velocity, the Doppler-free transition frequency has been determined with a statistical uncertainty of 58 kHz (see Fig. 4.7). For each velocity class also the 2^{nd} order Doppler shift was taken into account (2.3 kHz for 380 m/s, 7.4 kHz for 686 m/s and 13.6 kHz for 931 m/s). Furthermore, the measurements were performed in both deep-UV collision points, giving consistent results.

4.6.2 Phase shift

Another potential source of systematic error is a phase shift difference between the amplified frequency-comb pulses that depends on ΔN ; it would lead to a frequency shift

$$\Delta f = \frac{8 \cdot \Delta \phi}{2\pi \cdot \Delta N \cdot T_{rep}} \quad (4.3)$$

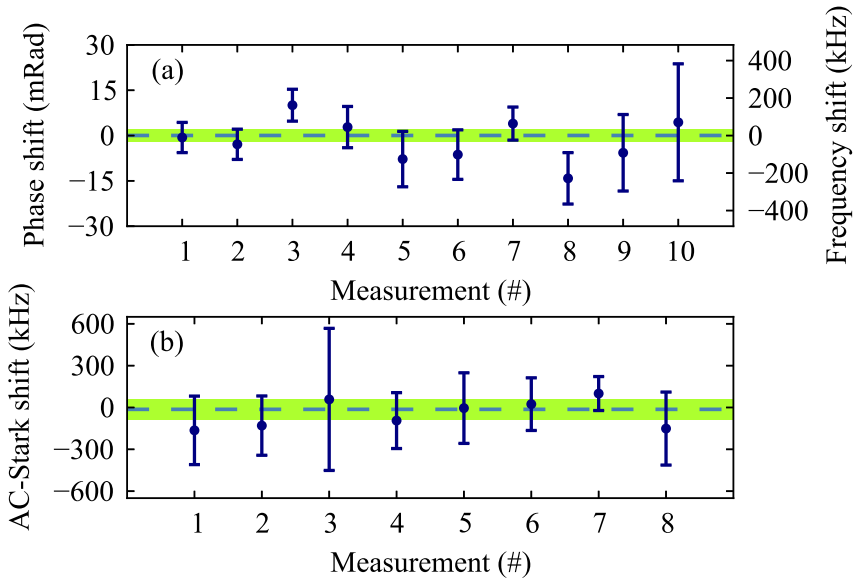


FIGURE 4.8: (a) Results of the differential phase measurement on the fundamental pulses at 850 nm between the $\Delta N = 2$ and $\Delta N = 7$ pulse pairs. The blue and red part of the amplified pulse spectrum are measured separately from which the mean shift is calculated and shown in the graph. No significant phase shift is observed within an uncertainty of 2.1 mrad (indicated with the green band), corresponding to 35 kHz on the transition frequency. (b) Results of the AC-Stark shift determination. Each data point represents an average of ten to twenty measurements. Within the uncertainty of 72 kHz (indicated by the green band) no shift due to the excitation light field is observed.

where $\Delta\phi$ is the phase change between the two excitation pulse pairs (with a factor 8 for using the fourth harmonic on a two-photon transition). The laser system was designed to keep $\Delta\phi$ of the amplified pulses as constant as possible as function of ΔN [69]. This is verified by measuring the phase difference between the amplified pulses and the original frequency-comb pulses with spectral interferometry [67]. Measurement results of the differential phase shift between $\Delta N = 2$ and $\Delta N = 7$ are shown in Fig. 4.8a. This shows the combined phases from the "red" and "blue" part of the spectrum contributing to the two-photon transition. There is no significant phase change within the uncertainty of 2.1 mrad (corresponding to 35 kHz uncertainty for the transition frequency).

4.6.3 DC-Stark shift

The DC-Stark effect is tested by a comparison of measurements in a static 29.4 V/cm electric field, and in a zero electric field (<0.17 V/cm), confirming a negligible ($\ll 1$

kHz) shift in the measured transition frequency.

4.6.4 AC-Stark shift

The AC-Stark shift is suppressed by a factor 100 by keeping the energy of the pulses constant to 1%. To detect any residual effect we vary the pulse energy deliberately with a factor of two, and extrapolate the measured transition-frequency difference to zero intensity. The determined residual AC-Stark of -13 (72) kHz (see Fig. 4.8b) is consistent with zero. Because the pulse energy was varied by reducing the infrared intensity, this simultaneously excludes effects induced in the frequency upconversion stages.

4.6.5 Detector gain shift

The separation of different isotopes in a TOF can be a potential source of systematic error. Isotopes that arrive early on the detector can modify the detector gain experienced by the isotopes that arrive later [130]. However, the natural abundance of ^{82}Kr and ^{83}Kr compared to ^{84}Kr is five times less and is therefore expected to have minimal influence. Any residual effect can be experimentally detected as a variation of the measured ^{84}Kr Ramsey signal phase when ΔN is changed, caused by the different Ramsey-signal phases of the other isotopes for each ΔN . No effect was detected on the ^{84}Kr isotope Ramsey signal when varying ΔN for all values between 2 and 8, with a resulting uncertainty margin of 25 kHz for the transition frequency.

4.6.6 Zeeman shift

Finally, we tested for a Zeeman shift by applying a magnetic field 8 times higher than the earth magnetic field. As expected for the $m_j = 0$ states, no shift was detected, excluding effects with an uncertainty of 13 kHz for the transition.

4.7 Isotope shifts

Our time-of-flight measurement enables to resolve the signals of the different isotopes (see Fig. 4.3). Therefore we can measure the signal for each isotope simultaneously with the ^{84}Kr signal using multiple boxcar integrators, each set on one isotope (see Fig. 4.9). The isotope shift $f_{84\text{Kr}} - f_{X\text{Kr}}$ is straightforwardly extracted from the observed relative phase at one single N . The ambiguity of the isotope shift frequency due to the comb-mode spacing is solved by a comparison with previous measurements

that have sufficient accuracy [63]. Some of the potential phase shifts that could influence the measurement are common-mode in the isotope shift measurement, such as the AC-Stark shift and (to a large extent) the Doppler-shift.

There is, however, an effect that does influence the measured isotope shift due to saturation effects of the ion detector. The different bunches of ions for each of the five isotopes are resolved in time, and give rise to five peaks spanning over roughly 800 ns, as shown in Fig. 4.3. Each peak is equivalent to the detection of approximately 1 to 10 ions within roughly 20 ns. The EDR-CEM detector is not specified for such high count rates. As a result, the signal from isotopes arriving early in the ToF might influence the signal from isotopes arriving later. This effect potentially distorts the Ramsey signal of the heavier isotopes. The situation is even more subtle, because the Ramsey signal amplitudes of the five isotopes signals evolve differently as function of delay time. To estimate the influence of the detector we performed the Ramsey-comb analysis procedure with different pulse delays (i.e. different N). Fig. 4.9 shows the simultaneous acquisition of the Ramsey fringes for the isotopes ^{82}Kr and ^{84}Kr for $N=2$ to 7. The isotope shift $f_{84\text{Kr}} - f_{82\text{Kr}}$ can be extracted from every single N scan. No systematic dependence on N has been observed for the isotopes ^{80}Kr , ^{82}Kr , ^{83}Kr and ^{84}Kr within the statistical uncertainty of 25 kHz. This uncertainty is quadratically added with the individual statistical errors giving rise to the following isotopes shifts: 301 847(43) kHz ($f_{84\text{Kr}} - f_{80\text{Kr}}$), 152 403(35) kHz ($f_{84\text{Kr}} - f_{82\text{Kr}}$) and 98 527(45) kHz ($f_{84\text{Kr}} - f_{83\text{Kr}}$).

However, the ^{86}Kr isotope is strongly affected by the detector saturation effect due to the high abundance and therefore strong signal of the preceding ^{84}Kr . Significant time was spend on characterizing this effect, and an attempt was made to model it. However, the modeling did not have enough predicting power to improve the accuracy. Therefore we conservatively base our error on the variation seen between the different measurements at different pulse delays and obtain an ^{86}Kr isotope shift of $f_{84\text{Kr}} - f_{86\text{Kr}} = -136.40(0.45)$ MHz.

4.8 Conclusion

Taking all measurements into account (see Table 4.1) we arrive at a frequency of 2,820,833,101,679 kHz with a 1σ uncertainty of 103 kHz (a relative uncertainty of $3.7 \cdot 10^{-11}$) for the $4p^6 \rightarrow 4p^5 5p[1/2]_0$ transition in ^{84}Kr . This result is 34 times more accurate and in agreement with the most accurate previous measurement [63], demonstrating the power of the Ramsey-comb method for transitions in the deep-UV wavelength range. The accuracy is mainly limited by the short lifetime (27 ns) of the excited

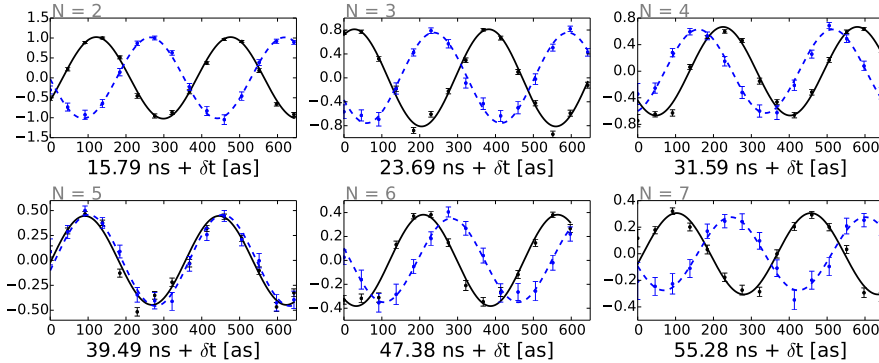


FIGURE 4.9: Example of the isotope shift measurements. Multiple Ramsey scans for ^{84}Kr (solid black line) and ^{82}Kr (dashed blue line) for pulse pairs ranging from $N=2$ to $N=7$ are shown. For each N , the signals of the two isotopes have been acquired simultaneously. Because of the difference in transition frequency, the phases of the Ramsey scans evolve differently in time. The isotope shift can be determined from the relative phase difference at each value of N .

TABLE 4.1: Contributions to the $4p^6 \rightarrow 4p^5 5p[1/2]_0$ transition frequency in ^{84}Kr with their respective uncertainties. All values are listed in kHz.

Contribution	Experimental value	1σ
Transition frequency ²	2820833101688	58
AC-Stark shift	-13	72
DC-Stark effect	0	0
Laser phase shift	1	35
Gain depletion ³	0	25
Zeeman shift	3	13
Total	2820833101679	103

state, because that determines the maximum pulse delay. This is particularly promising for spectroscopy on the $\text{EF} \leftarrow \text{X}$ transition in molecular hydrogen, as the excited state (for vibrational quantum number $\nu = 0$) has a lifetime of 200 ns. Potentially a frequency accuracy significantly better than 50 kHz might therefore be reached. That would be two orders of magnitude better than previous experiments [131], providing new opportunities to test QED and the proton size with H_2 molecules. Similarly, Ramsey-comb spectroscopy of the $1\text{S}-2\text{S}$ transition in He^+ ions looks promising with a 1.9 ms excited state lifetime and the sufficiently strong pulses for high-harmonic generation [100].

In addition to the investigated ^{84}Kr isotope, the other isotopes have been investigated relative to the most abundant ^{84}Kr isotope, see Table 4.2 for the results. This has resulted in an improvement of the uncertainties for the isotope shifts by a factor of 6.5, 4.2 and 3.7 for the isotopes ^{80}Kr , ^{82}Kr and ^{83}Kr respectively, compared to

TABLE 4.2: Measured isotope shifts in krypton relative to the ^{84}Kr isotope. The values listed in this table are in kHz.

Isotope	Isotope shift (relative to ^{84}Kr)	1σ
^{80}Kr	301847	43
^{82}Kr	152403	35
^{83}Kr	98527	45
^{86}Kr	-136400	450

[63]. The present ^{86}Kr isotope shift determination is less precise than the previous measurement, due to the saturation effect discussed in Section 4.7. Furthermore, the improvement in uncertainty is much less compared to improvement on the absolute transition frequency in ^{84}Kr . This is due to the relative nature of the measurement, which could already be performed with high accuracy in the previous experiment [63]. This in combination with the relatively short lifetime of the excited state limits the possible improvement of these determinations.

Deep UV Ramsey-comb spectroscopy of H₂ for fundamental tests of molecular quantum theory.

5.1 Abstract

Molecular hydrogen and its isotopic and ionic species are benchmark systems for testing quantum chemical theory. Advances in molecular energy structure calculations enable testing of quantum electrodynamics and potentially a determination of the proton charge radius from H₂ spectroscopy. We have measured the ground state energy in ortho-H₂ relative to the first electronically excited state by laser spectroscopy on the $EF\ ^1\Sigma_g^+(0,1) \leftarrow X\ ^1\Sigma_g^+(0,1)$ transition. The resulting transition frequency of 2971 234 992 965(73) kHz is two orders of magnitude more accurate than previous measurements. This paves the way for a considerably improved determination of the dissociation energy (D_0) for fundamental tests with molecular hydrogen.

5.2 Introduction

The fully quantized version of electrodynamics (QED) constitutes an important part of the Standard Model and is arguably the best tested theory in physics, based (among other experiments) on spectroscopic measurements of atomic hydrogen [21, 117, 118]. The molecular counterpart, H₂, has served as the model system for molecular quantum theory dating back to 1927 when Heitler and London first explained the existence of a bound state between two hydrogen atoms [132]. Although the increased complexity of the electronic structure and the additional vibrational and rotational degrees of freedom impose serious theoretical and experimental challenges, it also provides additional opportunities to explore new physics. Measurements of various level energies [131, 133–137] are in excellent agreement with the most recent theoretical predictions [124, 138, 139]. Comparisons between the experimental results and theory provide constraints on possible physics beyond the Standard Model, such as hypothetical fifth forces and extra dimensions [120, 125, 140, 141]. In particular the dissociation energy of molecular hydrogen $D_0(\text{H}_2)$ serves as an important benchmark

number for molecular quantum physics, and it has stimulated improvements by seven orders of magnitude in its experimental and theoretical determinations over nearly a century [142].

On the theoretical side a number of refined calculations have been performed to verify and improve the initial results [143]. The Born-Oppenheimer potential of H_2 was calculated to 10^{-15} precision [144], the adiabatic correction was improved by three orders of magnitude to $3 \times 10^{-7} \text{ cm}^{-1}$ [138], non-adiabatic corrections of rovibrational levels were calculated to 10^{-7} cm^{-1} precision [139], the $m\alpha^6$ QED corrections were explicitly calculated [52], and methods to solve the Schrödinger equation were improved [51]. This heroic program led to a value of $D_0(\text{H}_2) = 36\,118.069\,1(6) \text{ cm}^{-1}$, which is more accurate but consistent with the initial value [143]. Moreover, recent breakthroughs in calculating molecular structure and QED now indicate that it will become feasible to determine the proton-charge radius from a sufficiently accurate determination of $D_0(\text{H}_2)$ [51, 52]. This is particularly interesting in view of the proton-charge radius puzzle [29, 33, 36, 37, 122].

To obtain an experimental value of D_0 , it can be related to the ionization energy $E_I(\text{H}_2)$ via a thermodynamic cycle involving the well known atomic ionization energy $E_I(\text{H})$ and the dissociation energy of the ion $D_0(\text{H}_2^+)$ [133]. The value $E_I(\text{H}_2)$ can be experimentally determined by measuring two frequency intervals by way of laser spectroscopy, the $EF \leftarrow X$ and subsequent $54p1_1 \leftarrow EF$ transitions. As a third step in the sequence to determine D_0 extrapolation of the np -Rydberg series via millimeter wave excitation is required [145]. In Fig. 5.1 the level schemes and energy separations are displayed; the logic of connected experiments has been discussed in [142].

Previous experimental values for D_0 [133] were found to be in good agreement at a level of 0.0004 cm^{-1} (12 MHz) with molecular quantum calculations [143]. Agreement was also obtained for D_2 [134], and both results featured thereupon in interpretations in terms of constraints on fifth forces [125] and extra dimensions [141] for typical intramolecular distances at the 1 \AA scale. The uncertainty in these experiments need to be improved by two orders of magnitude in order to challenge the latest calculations and extract a proton-charge radius at the 1 % level.

Moreover, a more accurate determination of the fundamental ground tone (see Fig. 5.1) would provide an additional test of the most recent improvements in the calculation of the rovibrational energy levels of the ground state [124, 138, 139]. Direct excitation of this transition is dipole forbidden in H_2 , instead the energy splitting can also be determined from two separate transitions to the common electronically excited $EF \ ^1\Sigma_g^+(v=0)$ state (see Fig. 5.1) [146]. For the determination of D_0 and the FGT deep ultraviolet radiation (202 nm and 211 nm respectively) is required to excite the

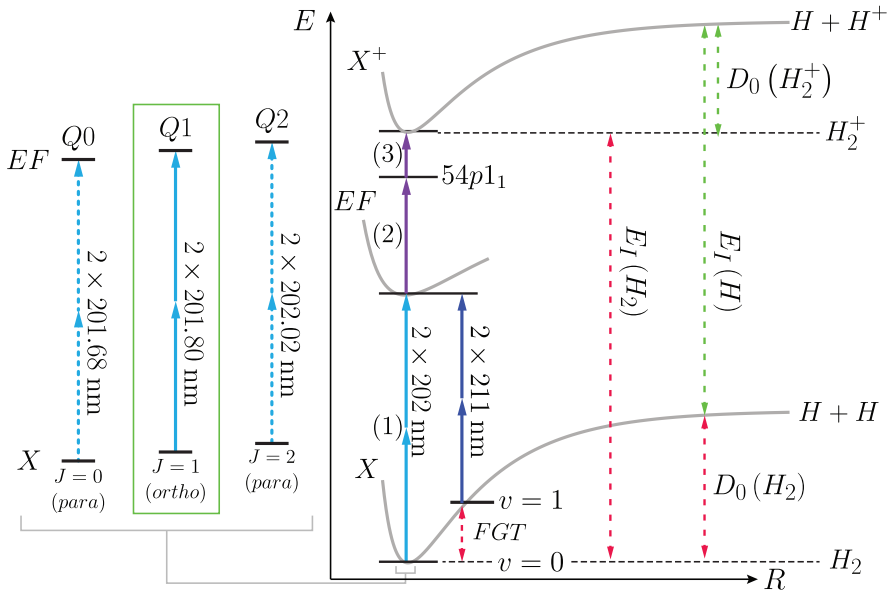


FIGURE 5.1: Energy level diagram of several two-photon transitions from the ground state ($X \ ^1\Sigma_g^+$) to the excited state ($EF \ ^1\Sigma_g^+$) in H_2 . Both the ionization energy (E_i) and the fundamental ground tone (FGT) are interesting tests of molecular QED-theory and are indicated by the red arrows. To determine E_i a series of experiments is required to couple the EF state to the $54p$ Rydberg state and the ionization potential. For the later two steps (indicated by the purple arrows) new experiments are being developed at the ETH in Zurich. To determine the FGT two separate excitations to a common excited state are required, due to the extremely low direct excitation probability. For the measurement of the FGT and the E_i high-accuracy spectroscopy at wavelengths of 202 and 211 nm is required. To demonstrate the feasibility of these experiments we have selected the Q1 line (indicated by the dashed green box) because it is three times more abundant at 300 K.

two photon transitions, making precise measurements difficult.

In this chapter we report on the determination of the $EF^1\Sigma_g^+ - X^1\Sigma_g^+(0,0)$ Q1 transition in H_2 by employing Ramsey-comb two-photon spectroscopy [67, 147] in the deep ultraviolet at 201.80 nm (see Fig. 5.1), which is, as discussed before, an essential ingredient for determining $D_0(H_2)$ and the FGT . Although ultimately a higher precision could be achieved for para- H_2 , due to the absence of hyperfine structure, this transition was selected because of the three times higher natural abundance of ortho- H_2 compared to para- H_2 at room temperature. We demonstrate a fractional uncertainty of $2.5 \cdot 10^{-11}$, achieving a two and three orders of magnitude improvement over previous measurements [148, 149].

5.3 Ramsey excitation with frequency comb pulses

The method of Ramsey-comb spectroscopy [67, 147] combines Ramsey’s method of separated oscillatory fields [65] with frequency comb lasers [56, 70]. It is based on interference between two excitation contributions in an atom or molecule induced by two time-delayed coherent laser pulses. This leads to a variation of the excited state population ($|c_e|^2$) as a function of pulse delay (t) and pulse phase difference ($\Delta\phi$) according to:

$$|c_e(t, \Delta\phi)|^2 \propto \cos(2\pi f_{tr}t + \Delta\phi) \quad (5.1)$$

The transition frequency (f_{tr}) can be determined from this signal, provided that t and $\Delta\phi$ are known with sufficient precision [63, 100]. Frequency comb lasers are therefore a convenient source of light pulses as their repetitive pulsed output (with spacing T_{rep}) and controlled phase slip between successive pulses (the carrier-envelope phase slip $\Delta\phi_{ceo}$) can be referenced with high accuracy to an atomic clock.

To increase the pulse energy of frequency combs for nonlinear frequency upconversion, amplification and enhancement resonators have been employed to increase the pulse energy to the μJ level at full repetition rate [60–62, 150]. In contrast, our method relies on the amplification of only two pulses, enabling orders of magnitude higher pulse energy ($>\text{mJ}$). By choosing pulse pairs with a delay of multiples of T_{rep} , and scanning the pulse delay on a much smaller scale using adjustments of T_{rep} via the comb laser, a series of Ramsey signals starting at time delays $t = T_0 = \Delta N T_{rep}$ is obtained. Here ΔN is an integer, denoting the delay expressed in the number of comb laser pulses. Combining a series of Ramsey signals for different ΔN constitutes a Ramsey-comb measurement [147]. The transition frequency is obtained from it by analyzing only the relative phase evolution between the Ramsey signals [68]. As a consequence, the measurement becomes insensitive to any phase shift that is independent of ΔN . This includes a possible constant phase shift caused by amplification and nonlinear upconversion of the frequency-comb pulses, and also phase shifts induced in the atom by the laser-atom interaction (the AC-Stark shift), provided that the pulse energy is constant as function of ΔN . The accuracy of the method is mainly limited by the maximum time delay that one can experimentally achieve and the accuracy of how constant $\Delta\phi$ is as a function of ΔN .

5.4 Experimental setup

The starting point of the experiment is a Kerr-lens mode-locked Ti:Sapphire frequency comb which runs at a repetition time of 7.9 ns. Both T_{rep} and $\Delta\phi_{ceo}$ are actively

stabilized and referenced to a cesium atomic clock (Symmetricon CsIII 4310B) to provide absolute time and frequency calibration. The pulses are chirped by 2.5×10^6 of 2^{nd} -order dispersion in a 4f-grating based stretcher. In addition, an adjustable slit placed in the Fourier plane of the stretcher that selects only 0.2-0.3 nm bandwidth of the original spectrum centered around 807.18 nm, resulting in pulses of approximately 10-15 ps long and 0.8 pJ. Such a small bandwidth is chosen to avoid excitation of the nearby Q0 and Q2 lines which are at respectively 806.73 and 808.09 nm of the fundamental frequency-comb wavelength (see Fig. 5.1). Only two of these pulses are selectively amplified in a noncollinear optical parametric chirped-pulse amplifier (NOPCPA) upto a pulse energy of 2.4 mJ. The pump pulses for the NOPCPA are derived from a separate Nd:YVO₄ based mode-locked oscillator that is synchronized with the frequency-comb laser. From this oscillator a pulse pair is selected using fast modulators, and subsequently amplified upto 28 mJ (for more detail see [69, 105] and Chapter 3). These pulses are frequency doubled to 532 nm providing two nearly identical pump pulses of 75 ps pulse duration. The complete laser system that produces the two amplified frequency-comb pulses with an adjustable time delay is referred to as the Ramsey-comb laser system in Fig. 5.2.

The amplified frequency-comb pulses are frequency doubled to 403.59 nm in a 0.5 mm thick β -barium-borate (BBO) crystal. Subsequently, the fundamental 807.18 nm and the doubled 403.59 nm radiation are together up-converted to 269.07 nm by sum-frequency generation in a 0.8 mm thick BBO crystal. Then the 269.07 and 807.18 nm are mixed together in 0.3 mm BBO to produce the required 201.80 nm radiation. Before the two mixing stages custom waveplates are placed to be able to orient the polarization of the 807.18 nm, 403.59 nm and 269.07 nm with respect to the optical axis of the BBO crystals. In this configuration we produce upto 62.3 μ J pulse energy in a beam with a FWHM diameter of 1.2 mm (a schematic overview of the setup is depicted in Fig. 5.2).

The ultraviolet radiation is split in two equal parts to excite the transition in a counter-propagating configuration in order to suppress the first-order Doppler shift. The beams are aligned as parallel as possible using the output of the beamsplitter, which forms a Sagnac interferometer [129]. With linear polarized light the two-photon transition may also be excited from just a single side, which gives rise to a Doppler broadened and shifted background. To circumvent this issue a quarter wave plate is placed in both arms in order to convert linear to circular polarization. Together with the strong chirp on the pulses [127, 151], this suppresses the unwanted (Doppler shifted) excitation from a single side by a factor of ten. The intersection point of the ultraviolet pulses is crossed at right angles with a beam of hydrogen molecules. The

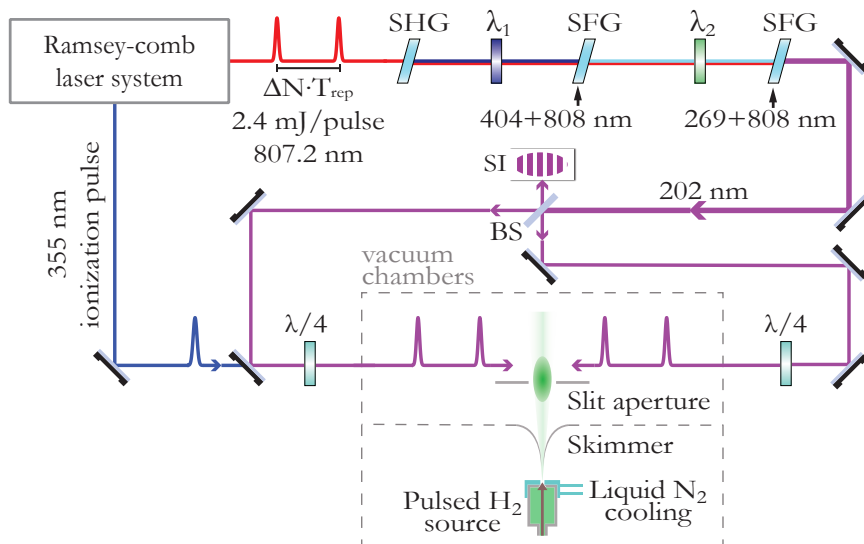


FIGURE 5.2: Schematic overview of the frequency conversion and excitation geometry of the experimental setup. The amplified frequency-comb pulses from the Ramsey-comb setup are passed through a $\lambda/2$ waveplate and thin-film polarizer (tfp). Then they are up-converted in sequential stages of type I frequency doubling and mixing in BBO. In between the frequency up-conversion stages special waveplates are situated to match the polarization of the fundamental and up-converted light to the optical axis of the BBO crystals. The resulting beam of 201.80 nm radiation is split in equal parts by a metallic beamsplitter (BS). The deep ultraviolet beams are aligned as parallel as possible using the fringes observed at the output of the beamsplitter, which forms a Sagnac interferometer (SI). After the last excitation pulse an ionization pulse is applied that state selectively ionizes the H_2 . The ions are then extracted upwards in a time-of-flight drift tube and detected with a electron multiplier. The molecular beam is formed from a pulses supersonic expansion of H_2 which is collimated by a skimmer 0.5 mm aperture and a slit of 3 mm width.

molecular beam of H_2 is generated from a pulsed supersonic expansion from a nozzle operated at 3 bar backing pressure (Parker General Valve series 99). Its divergence is determined by the geometry of a skimmer of 0.5 mm aperture placed 3 cm behind the nozzle and a slit of 3 mm width situated 24 cm after the skimmer. The valve was fitted with a home build liquid nitrogen (LN_2) cooling system and a modified plunger to be able to operate at temperatures below 100 K. By cooling down the valve the the velocity of the molecules in the supersonic expansion can be slowed down.

Exactly 5 ns after the second excitation pulse an ionization pulse of 355 nm wavelength is applied that state-selectively ionizes the molecular hydrogen. The created H_2^+ ions are extracted upwards through a 25 cm time-of-flight drift tube and detected with an electron multiplier (ETP electron multiplier AF880). The electric fields used to accelerate the molecular hydrogen ions is ramped up after the ionization pulse to

ensure field free excitation. The ion signal is measured with a boxcar integrator (Stanford Research SR250) and subsequently digitized. The excitation and detection sequence is repeated at an interval of 35 ms.

5.5 Parametric amplifier phase shift

Both pump pulses for the NOPCPA are derived from the same cycle in the amplification process of the pump pulses. Therefore the two pump pulses will not be exactly equal and influence the frequency-comb pulses differently. This causes a phase shift ($\delta\phi$) between the amplified frequency-comb pulses that can potentially lead to a shift of the measured frequency. In fact, the absolute magnitude of the phase shift can be on the order of a few hundred mrad. However, in a Ramsey-comb measurement this does not translate into a frequency shift if $\delta\phi$ is constant as function of the time delay between the pulses. Any residual linear phase shift ($\delta\phi_{rel}$) as function of the pulse time delay (ΔNT_{rep}) will give rise to a frequency shift (δf) according to:

$$\delta f = \frac{8\delta\phi_{rel}}{2\pi\Delta NT_{rep}} \quad (5.2)$$

The factor 8 accounts for the 4th harmonic generation and the two photons that contribute to the excitation. To ensure that the measurement is not affected by such a frequency shift, the phase shift between the excitation pulses in the infrared is measured using spectral interferometry. A small amount of the original frequency-comb pulse is split off before the NOPCPA and is later recombined its amplified counterpart with an adjustable time delay (on the order of a few ps). The spectral interference is recorded by projecting the first and second excitation pulse separately on a CCD camera in a grating based spectrometer. The phase difference can then be determined from such a recording [69]. An example of such a phase measurement is shown in Fig. 5.3. The phase shift $\delta\phi$ is around -203.5 mrad and the round (grey) data points indicate different measurements. The uncertainty on the round (grey) data points is the statistical uncertainty determined from the variation of the phase shift over 750 laser shots, corresponding to 27 seconds acquisition time and a total acquisition of 3.5 hours. To suppress the influence of any systematic drift, the time delay step ($\Delta N \times T_{rep}$) was scanned linearly up and down and in random order for different measurements. The diamond-shaped (red) data points are the average of the individual measurements at each time delay.

The resolution of the spectrometer is limited by the spacing of the lines on the grating and the size of the beams. Therefore it becomes increasingly difficult to measure

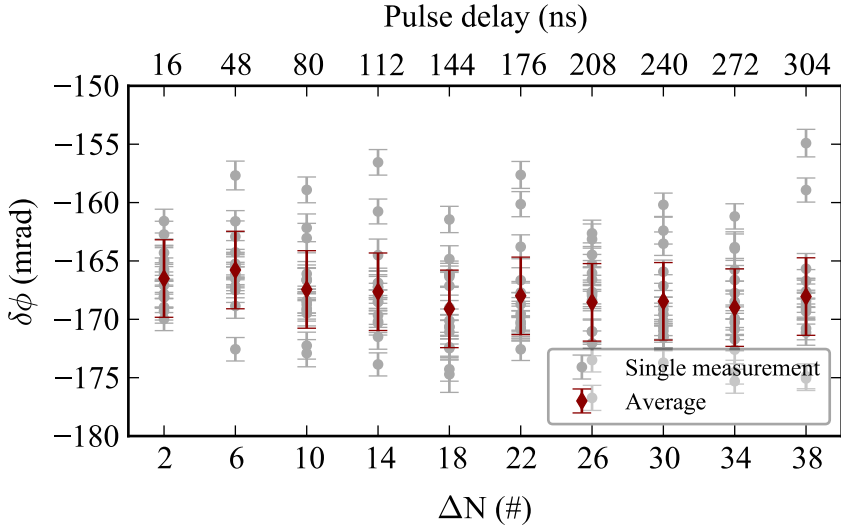


FIGURE 5.3: Measurement example of the phase shift between the two excitation pulses in the infrared. The round data points (grey colored) are an average of 750 laser shots and the error bar indicates the statistical uncertainty based on the variation within that set. To suppress systematic drift, the step size in ΔN was varied differently for different measurements and the total time to acquire all data is 3.5 hours. The diamond-shape data points (red colored) are the average of the individual measurements at each time delay.

the phase difference for an ever smaller bandwidth with any realistic setup. Moreover, spreading out the spectrum over a larger part of the CCD to increase the resolution will lower the total intensity of the light available per pixel. This is not a problem for the amplified pulses but is a limiting factor for the reference pulses from the frequency-comb, leading to a poor signal-to-noise ratio. The Ramsey-comb measurements presented in this paper are typically acquired using 0.2-0.3 nm bandwidth and is therefore particularly challenging for an accurate phase measurement. To determine the phase variation over the time delays that we probe in this experiment we have measured the phase effects for different bandwidths. Measurements of the phase evolution as function of time delay for bandwidths ranging from 0.4 to 3 nm are shown in Fig. 5.4. From these measurements we conclude that there is no systematic change in the operation of the NOPCPA with respect to the phase as function of bandwidth.

If one assumes a linear relation of the relative phase shift as function of time delay the frequency shift can be determined according to Eq.5.2. As an example we have plotted a phase measurement for $\Delta\lambda = 0.4$ nm in Fig. 5.5. This measurement was taken under the same conditions as the data presented in Fig. 5.3. The blue line is a

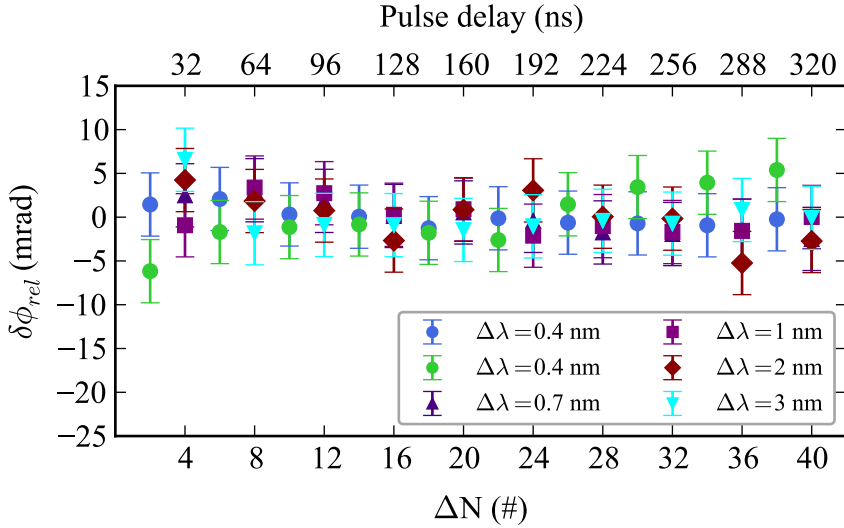


FIGURE 5.4: Measurements of the relative phase shift between the first and second excitation pulse in the infrared as function of delay time between the pulses. The measurements were done by operating the NOPCPA at various bandwidths ranging from 3 down to 0.4 nm, indicated by the different markers (and colors). No systematic change as function of bandwidth can be observed from this data.

linear fit through the data and from the slope a systematic frequency shift of -10 kHz is determined based on Eq.5.2. The two green lines are also linear fits through the data but with an adjusted slope such that the reduced χ^2 of the fit is ≤ 1 . Therefore, based on this data the slope cannot be determined more accurate than indicated by the blue shaded area in Fig. 5.5. As a result we interpret the uncertainty on the slope as 39 kHz. The same analysis was done for the measurements all the measurements presented in Fig. 5.4 and the results range from a frequency shift between -26 kHz and 42 kHz, all with an uncertainty close to 40 kHz. Because the measurements at 0.4 nm bandwidth most closely represents the conditions during the Ramsey-comb measurements, these results are averaged together resulting in a frequency shift of 14(40) kHz due to the amplifier induced phase shift. In this procedure we assumed an upper limit of 40 kHz uncertainty based on the uncertainty of the individual measurements.

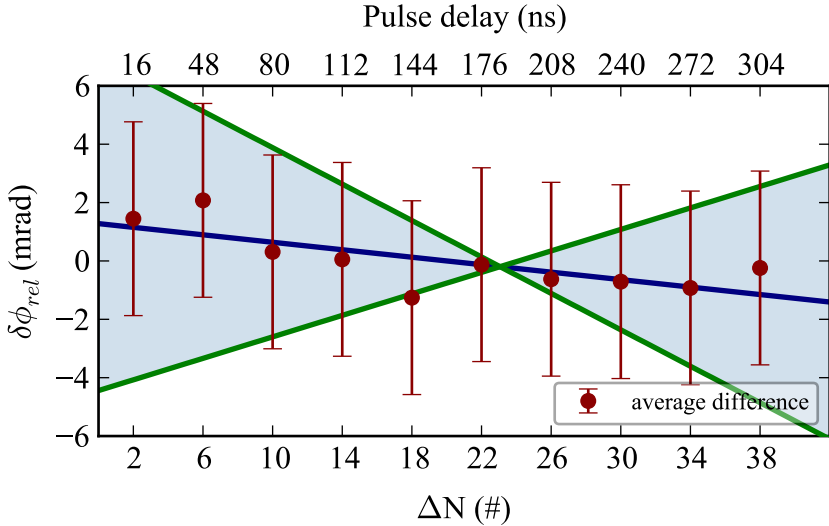


FIGURE 5.5: A measurement under similar conditions as presented in Fig. 5.3. The blue line is a linear fit to the data and based on the slope of this fit the frequency shift can be determined. The green lines are also linear fits through the data that have the maximum slope but still fit the data with a reduced χ^2 of one. Based on this data the frequency shift cannot be determined with an accuracy better than indicated by the blue shaded area within the green fits to the data. These maximum values are taken as the uncertainty on the frequency shift.

5.6 Results and systematic errors

In Fig. 5.6 an example of a Ramsey-comb measurement is shown where the pulse delay is varied up to a maximum delay time of 380 ns, corresponding to a separation of $\Delta N = 48$ pulses. At each ΔN the repetition time is scanned over a range of 600 attoseconds to observe ~ 1.5 period of the Ramsey signal. The uncertainty of the data points is based on the fluctuations of the ion signal averaged over 500 laser shots. The reduction of the signal and modulation contrast as a function of delay is caused by effects such as the laser linewidth, Doppler broadening, transit time, and the lifetime of the excited state (≈ 200 ns [152]). A typical Ramsey-comb measurement consists of sets of three or four Ramsey-scans over a maximum time delay between 181 and 221 ns, which is chosen for optimal signal-to-noise ratio and speed of a single measurement to minimize the influence of drifts. To avoid a systematic effect on the frequency determination we always skip $\Delta N = 1$ to bypass any transient effects, and the measurements were performed in random order, spread out over many days.

One Ramsey-comb measurement typically has a statistical uncertainty of 45 kHz (for details on the signal analysis procedure see [68]). However, the observed transition frequencies fluctuated more than expected based on the 1σ uncertainty of a single measurement. Because no statistically significant correlation could be found with any of the experimental parameters, the uncertainty of each measurement was increased by a Birge factor [153, 154] of 1.9 to correctly account for the true statistical uncertainty. Apart from the statistical uncertainty and the influence of the phase of the excitation pulses the measured frequency can also be influenced by a number of systematic effects. These effects are addressed separately in the subsections below.

The frequency determination of such a measurement is done purely in the time-domain, based on the phase of the Ramsey signals (for detail see [68]). The phase of each Ramsey fringe is determined by fitting a cosine to the individual Ramsey fringes with a fixed initial guess frequency but variable phase, based on Eq. (5.1). The frequency is then determined by a least-square fitting algorithm based the phase difference between the measured phases and phase evolution of the guess frequency. Because we are only resonant with a single transition in the H_2 molecule, it would suffice to measure only three Ramsey fringes to determine the frequency and a global phase shift. In practice if the mode spacing of the individual measurements becomes too large it will be difficult to assign the right mode for the frequency determination, in that case measuring more Ramsey fringes might be required.

Complementary to the time domain Ramsey-comb signal we can obtain a spectrum by fast-Fourier transformation of the data from Fig. 5.6 leading to the spectrum in Fig. 5.7. The frequency-axis spans exactly the fundamental repetition rate of the frequency-comb laser (126 MHz). The recurrence of the signal within this range is caused by the sub-sampling of the Ramsey-signals at an interval of $\Delta N = 5$. This graph illustrates the connection with traditional direct frequency comb spectroscopy where the the signal is convolution of resonance with the comb spectrum giving rise to spectral features that repeat at the repetition rate. In this case (as detailed in Section 2.2.2) the comb spectrum is reconstructed by combining the Ramsey signals from different time delays giving rise to the spectrum. Similarly to the traditional direct frequency-comb spectroscopy the correct mode needs to be assigned for which the investigated resonance transition needs to be known sufficiently accurate. If this is not the case the ambiguity might be solved by repeating the measurement at a different repetition rate, as is the case for normal direct frequency-comb spectroscopy. The best value currently known for the Q1 transition is indicated with the green data

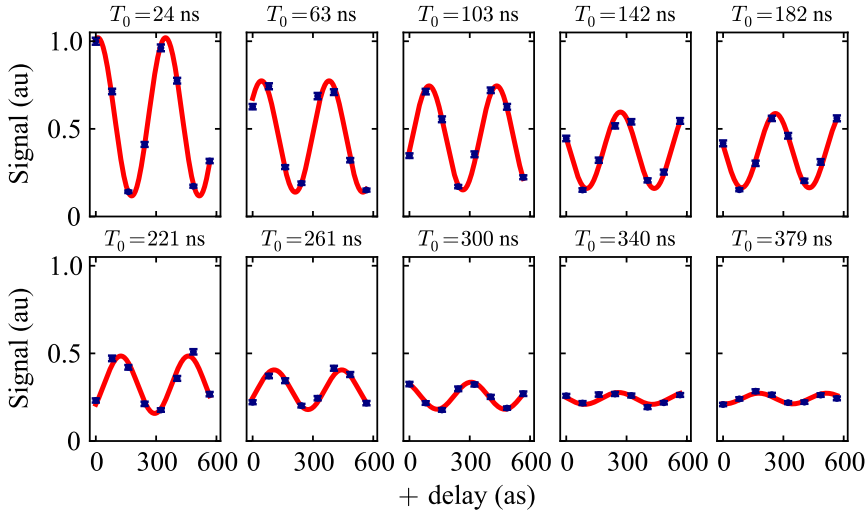


FIGURE 5.6: An example of a Ramsey-comb measurement with a mode spacing $\Delta N = 5$. The decay of contrast of the Ramsey fringes as function of time delay is clearly visible. The red line through the data is a fit based on a fixed frequency but adjustable phase. The phases of the Ramsey-fringes are then used for the determination of the transition frequency. The error bars of the individual data points are based on the variation of the ion signal over 210 laser shots and all the Ramsey fringes are normalized to the maximum signal of the first Ramsey measurement.

point and is in this case sufficiently accurate ¹. Also plotted in this graph are the positions of the Q0 (yellow) and Q2 (red) transitions [148]). From this graph we can also conclude that we are resonant with only one transition, this is important for the analysis because if not taken into account properly can cause a shift of the extracted frequency, see [68].

5.6.1 Doppler shift

The speed of hydrogen molecules from a supersonic expansion at 311 K is 2530 m/s [155, 156]. Because of this, the Doppler effect is one of the more prominent effects that has a systematic influence on the measured transition frequency. The measured frequency is given by:

$$f_{meas} = f_0 + \frac{\mathbf{k} \cdot \mathbf{v}}{2\pi} - \frac{v^2}{2c^2} f_0 \quad (5.3)$$

¹Admittedly, there is some room for debate, based on Fig. 5.7, whether we probe Q1 or Q0. However, measurement we also performed with a spacing of $\Delta N = 1$ providing the necessary resolution. Moreover, already the measurement of the wavelength of the fundamental light provides enough resolution and forms a nice consistency test.

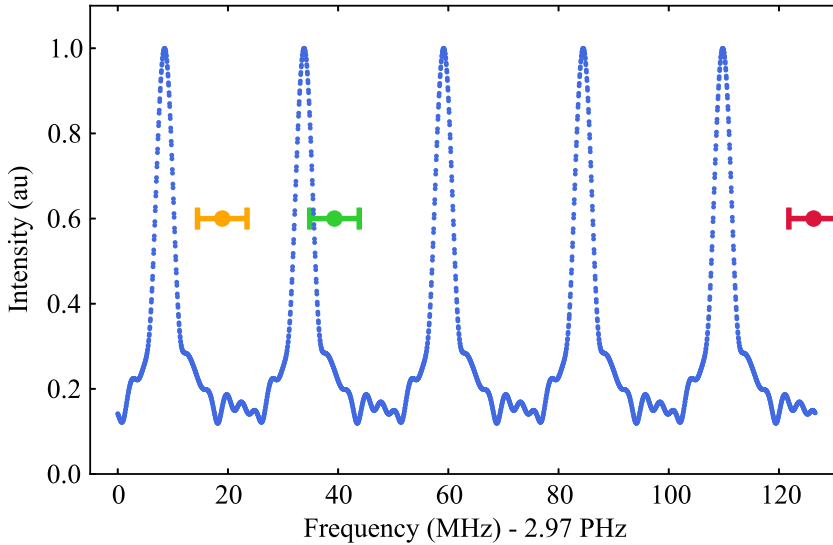


FIGURE 5.7: The fast-Fourier transform of the data presented in Fig 5.6. The x-axis spans exactly the fundamental repetition frequency of the frequency-comb laser. The recurrence of the signal is due to the mode spacing of $\Delta N = 5$ used during this measurement. The orange, green, and red data points indicate the best measurement thus far of the Q0, Q1, and Q2 line respectively. The figure shows that the bandwidth we use is small enough to only excite a single transition and that in this case we are resonant with the Q1 transition. This is also confirmed by measuring the spectrum of the infrared pulses.

where f_0 is Doppler-free transition frequency and $\mathbf{k} = \frac{2\pi f_{laser}}{c} \hat{\mathbf{k}}$ is the wave vector of the excitation laser and $\mathbf{v} = v\hat{\mathbf{v}}$ is the speed and direction of the molecules. In this formula the term that is linear with the speed of the molecules is called the first-order Doppler shift and the term that is quadratic with the speed of the molecules is called the second-order Doppler shift. Although the excitation geometry strongly suppresses the first-order Doppler shift, a residual first-order Doppler shift can still be present due to an asymmetry in the spectrum, a chirp induced first-order Doppler shift [117] or a residual angle between the two counter-propagating beams. The latter leads to a first-order Doppler shift according to:

$$\Delta f = \frac{f_0 \|v\|}{c} \sin\left(\frac{\theta}{2}\right) \quad (5.4)$$

where θ is a small angle between the two excitation beams. To minimize this effect we align the counter propagating beams as parallel as possible by observing a dark fringe at the output port of the Sagnac interferometer (see Fig. 5.2). Observing a dark fringe means that period of the fringes is bigger than the diameter of the beam,

and the angle can then be aligned better than $\theta < \frac{\lambda_{laser}}{2d}$ [129]. In practice we can observe the beam at the output port with a size on the order of 4 mm diameter, it therefore means that we cannot guarantee an aligned of the system with a precision better than 318 kHz. In addition, also the chirp of the pulses will effectively give rise to a first-order Doppler shift depending on the path the atoms travel through the laser beam [117]. To calibrate the first-order Doppler shift measurements were performed at two velocities of the molecular beam. The molecules were slowed down by cooling the nozzle using liquid nitrogen leading to a temperature of the nozzle of 97 K. For both temperatures an uncertainty in the velocity of $\pm 10\%$ was taken into account. The Doppler-free transition frequency can then be determined by extrapolating the measured transition frequencies to zero velocity. In this procedure the second-order Doppler shift correction of 107 and 33 kHz for 2530 and 1420 m/s was taken into account. Furthermore, the system was always aligned such that the observed frequency difference was as small as possible, although this could vary within ± 200 kHz. In total 7 sets of measurements were obtained to determine the Doppler-free transition frequency, each consisting of 20 or more Ramsey-comb measurements at both temperatures (and therefore velocity). All measurements are in agreement with each other within the statistical uncertainty, leading to a weighted average of all measurements (before other corrections) of 2 971 234 992 948(60) kHz.

5.6.2 AC-Stark shift

Although the Ramsey-comb method is to first order insensitive to effects proportional to the pulse energy (such as the AC-Stark effect or phase shifts in the upconversion) a residual light shift might still be present. We test this by measuring the transition frequency at pulse energies of 18 μJ and 62 μJ (the energy at which all other measurements were performed, within 5%). Extrapolation to zero intensity then gives the shift at 62 μJ pulse energy. In total 91 determinations of this kind are taken into account, each consisting of at least four Ramsey-comb measurements (Fig. 5.8). The resulting light shift correction is 3(13) kHz, showing that the Ramsey-comb method is for all practical purposes AC-Stark shift free.

5.6.3 DC-Stark shift

A DC-Stark shift is avoided by ramping-up the ion-extraction fields after the ionization pulse. The uncertainty for any residual electric field during the excitation is ± 0.17 V/cm. By comparing with measurements at a static electric field of 8.33 V/cm we determined a possible frequency shift of 0(2) kHz due to dc electric fields.

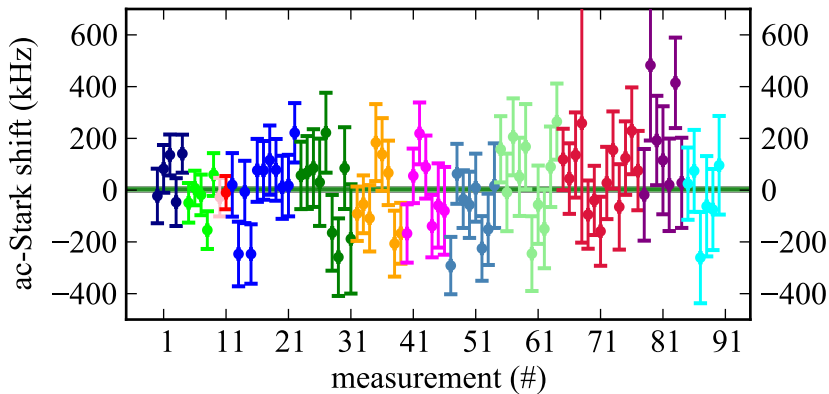


FIGURE 5.8: Measurement of the ac-Stark shift in molecular hydrogen. The different colors indicate measurement taken on different days. Each measurement consists of at least four Ramsey-comb measurements taken between $18 \mu\text{J}$ and $62 \mu\text{J}$ and extrapolated to zero intensity. These measurement show no measurable ac-stark shift within a statistical uncertainty of 13 kHz.

5.6.4 Zeeman shift

To avoid a possible Zeeman-shift the magnetic field is measured and minimized with additional coils to a precision of 0.2 G. A possible shift due to a residual magnetic field was determined by comparing with measurements at a magnetic field strength of 6 G in directions parallel and orthogonal to the polarization of the excitation pulses. No Zeeman-shift was detected, leading to an uncertainty due to this effect of 2 kHz.

It should be considered that for ortho-hydrogen the total nuclear spin $I = 1$, which leads to hyperfine structure in the Q1 line. The splitting in the ground state is too small (≤ 500 kHz) to be observed [157], and in the excited state unknown. Therefore the presented value is a weighted average of the hyperfine components of the Q1 line. The Q0 transition from the true ground state in para-hydrogen does not have hyperfine structure, but is three times weaker due to spin statistics. For this reason Q1 was measured in the current and previous experiments.

5.7 Conclusion

Taking all effects into account results in a transition frequency of $2\,971\,234\,992\,965(73)$ kHz for the $EF^1\Sigma_g^+ - X^1\Sigma_g^+(0,0)$ Q1 transition in ortho- H_2 (see Table 5.1). The relative uncertainty of this result is $2.5 \cdot 10^{-11}$, and is in agreement with the previous measurement [148], but two orders of magnitude more accurate (see Table 5.2). The new

TABLE 5.1: Contributions (in kHz) to the measurement of the $EF^1\Sigma_g^+(0,1) \leftarrow X^1\Sigma_g^+(0,1)$ transition in H_2 . The Doppler-free transition frequency is obtained by the procedure described in the Section 5.6.1. The light induced effects include the AC-Stark shift and non-linear effects.

	Measured value	(1σ)
Doppler-free transition frequency	2971234992948	(60)
Light induced effects	3	(13)
DC-Stark shift	0	(2)
Zeeman shift	0	(2)
Amplifier phase-induced shift	14	(40)
Total	2971234992965	(73)

two-photon transition frequency of the Q1 line of ortho-hydrogen can be used to obtain an improved value for the (rotationless) dissociation energy $D_0(H_2)$ of para-hydrogen, using the procedure from [133]. The result is consistent with previous experimental determinations and theory, as shown in Table 5.2.

However, in a recent study a complete calculation of the relativistic corrections was targeted to reach a full-fledged molecular quantum calculation [158]. In [143] the relativistic correction was partially based on an older study [159]. The new refined calculation surprisingly produces a disagreement of 50 MHz (0.0017 cm^{-1}) with the previous and current experimental values, equal to 2.4σ (see Table 5.2). However, as the authors state, this disagreement is to be considered preliminary since relativistic nuclear recoil corrections have not yet been reliably calculated. Our result now shows that possible deviations are not due to measurements of the $EF - X$ interval, given its new highly accurate value.

The full potential of our measurement can only be reached if the energy separation between $X^+ - EF$ is improved to a level comparable with 70 kHz or better, to bring down the uncertainty of $D_0(H_2)$. This will enable to put further constraints on the strength of fifth forces [140] and on the compactification sizes of extra dimensions [141]. Moreover, given the ≈ 200 ns lifetime of the excited state it seems feasible to ultimately reach 10 kHz accuracy on the Q0 transition (instead of Q1 to eliminate the influence of hyperfine structure). A theoretical and experimental comparison at this level would enable a determination of the proton-charge radius with an accuracy of 1%, therewith resolving the proton-charge radius puzzle. Furthermore, another benchmark test of molecular quantum theory, the determination of the fundamental ground tone splitting (see Fig. 5.1), can be considerably improved now with a measurement of the $EF^1\Sigma_g^+ - X^1\Sigma_g^+(0,1)$ Q1 transition.

TABLE 5.2: Main contributions to the determination of D_0 in H_2 in cm^{-1} and the comparison with previous results and the latest theoretical values.

Transition	Previous results	This result	Theory	Deviation
(1) $EF \leftarrow X$	99 109.731 39(18) [148]	99 109.731 204 9(24)		0.000 19(18)
(2) $54p1_1 \leftarrow EF$	25 209.997 56(29) [133]			
(3) $X^+ \leftarrow 54p1_1$	42.270 539(10) [145]			
D_0	36 188.069 62(37) [133]	36 118.069 45(31)	36 118.069 5(10) [143] 36 118.069 1(6) [52] 36 118.067 8(6) [158]	0.000 1(10) -0.000 4(7) -0.001 7(7)

The experiments described in this thesis had two main objectives. The first was to demonstrate that the Ramsey-comb method can be applied in the deep ultraviolet after frequency upconversion of the amplified frequency-comb pulses. The second objective was to then measure a transition that is relevant for tests of QED or molecular quantum mechanics. The experimental results achieved with krypton and molecular hydrogen demonstrate that the amplified frequency-comb pulses can be upconverted efficiently and used for high-precision spectroscopy. Concerning the second goal, the energy levels of krypton are not very interesting regarding QED because calculations for such a many-electron system cannot be performed at (or even close to) the same level of accuracy as the measurements. In contrast, transitions in molecular hydrogen are actually useful to perform tests for molecular QED. However, the measured transition still requires additional measurements before a 'direct' test of molecular QED can be performed through a comparison of the dissociation limit. Nonetheless, the results presented in this thesis show the feasibility of experiments on transitions that can lead to new and improved tests of (molecular) QED calculations.

6.1 Molecular hydrogen

One interesting transition that can readily be investigated with the current setup is the $EF(\nu = 0) \leftarrow X(\nu = 1)$ transition in molecular hydrogen. By combining this value with the measurement presented in this thesis on the $EF(\nu = 0) \leftarrow X(\nu = 0)$ transition a better determination of the fundamental ground tone (first vibrational energy splitting) can be achieved (see also Fig. 5.1). Progress on the theoretical side in recent years has led to accurate ab initio calculations for the entire ground state rovibrational manifold [124, 143]. Therefore a measurement of the fundamental ground tone can directly be compared to calculations providing a stringent test of molecular QED, and can even provide constraints on possible physics beyond the Standard Model, such as hypothetical fifth forces and extra dimensions [120, 125, 140, 141]. Although the required wavelength can be obtained in a fairly straightforward way, the difficulty of this experiment is in the low abundance of molecules that are in the $\nu = 1$ excited state. One route to enhance the population of this state is to make an electric discharge at the exit of the nozzle for the molecular beam. This experiment has been performed by our group based on a completely different laser system [131]. To limit the uncertainty due to the Doppler shift, now the largest contributor to

the error budget, it is desirable to redesign the molecular beam line. Especially the distances and size of the first skimmer with respect to the nozzle can be improved to obtain a much better collimated molecular beam and avoid 'skimmer clogging'. It is feasible to reach a similar accuracy for this transition as presented in this thesis, and this would lead to a two orders of magnitude improvement of the fundamental ground tone energy accuracy. In addition, similar studies on the isotopes of hydrogen would provide additional tests without having to change much in the experimental setup.

6.2 Extension to the XUV: Towards spectroscopy on the 1S-2S transition in He^+

Helium is also a very interesting candidate but an even more challenging element for precision tests QED. It is interesting because helium has a higher nuclear charge, compared to hydrogen, which leads to an increased contribution of higher-order QED corrections [46]. The challenge on the theory side in neutral helium is the coupling between the two electrons which limits the precision of the calculations. Therefore more interesting is the singly-ionized helium atom, and in particular the 1S-2S transition. The simplicity of the one-electron system allows for highly accurate calculations of the energy levels and a comparison with theory would provide stringent tests of these calculations. Moreover, in combination with measurements in μHe^+ [47], it would provide a similar comparison as was made between electronic and muonic hydrogen [29](see Fig. 1.1). Muonic systems have the added benefit that the nuclear size effects are nearly 2 orders of magnitude stronger compared to hydrogen [46]. The main reason that singly-ionized atomic helium has not been excited on the 1S-2S transition yet is that it requires XUV radiation to excite the two-photon transition. To add to the complexity of the experiment, in order to control the systematic effects the helium ions need to be trapped and sympathetically cooled [160]. With the Ramsey-comb method it is now feasible to generate enough flux at the required XUV wavelengths via high harmonic-generation (see e.g. [161]) and perform ultra precise measurements. At the time of writing, a vacuum setup for XUV generation based on 2 amplified comb pulses (and refocusing of the generated light) has been constructed, and high harmonics have been produced. The next step is to demonstrate Ramsey-comb excitation in the vacuum- or extreme-ultraviolet with it, and ultimately to use it to measure the 1S-2S transition in He^+ with 1 kHz or better accuracy.

Excitation with two phase coherent laser pulses



In order to understand and analyze the Ramsey-comb signals the interaction of a two-level quantum system with an electromagnetic field close to resonance is analyzed. The interrogated atoms or molecules can be approximated as a two level the quantum system, where the eigen energies of the two states are called E_1 and E_2 , which are separated by an energy interval $\Delta E = E_2 - E_1 = \hbar\omega_0$. The zero point energy can be chosen such that $E_2 = -E_1 = \frac{\hbar\omega_0}{2}$. The time evolution of such a system is governed by the time-dependent Schrödinger equation:

$$i\hbar\frac{\partial}{\partial t}\Psi(\mathbf{r}, t) = H(t)\Psi(\mathbf{r}, t) \quad (\text{A.1})$$

where the atom is represented by the wave function or state vector

$$\Psi(\mathbf{r}, t) = c_1(t)\psi_1(\mathbf{r}) + c_2(t)\psi_2(\mathbf{r}) \equiv |\Psi\rangle = c_1(t)|1\rangle + c_2(t)|2\rangle \quad (\text{A.2})$$

Here the two eigenstates are labeled $|1\rangle$ and $|2\rangle$ respectively and normalization requires $|c_1(t)|^2 + |c_2(t)|^2 = 1$. To determine the state vector $|\Psi(t)\rangle$ after a certain time t , the coefficients $c_n(t)$ need to be determined (from now on the time dependence will be omitted but is assumed implicitly). For this the Schrödinger equation needs to be solved for the appropriate Hamiltonian. The Hamiltonian can be separated in a time-independent and a time dependent term

$$H(t) = H_0 + H_{int}(t) \quad (\text{A.3})$$

where the time-dependent term describes the interaction with an oscillating electric field that perturbs the eigenfunctions of the time-independent H_0 . The unperturbed eigenvalues of H_0 are just the atomic energy levels (neglecting spontaneous emission,) and the state vector should satisfy

$$H_0|\Psi\rangle = E|\Psi\rangle = -\frac{\hbar\omega_0}{2}|1\rangle + \frac{\hbar\omega_0}{2}|2\rangle \quad (\text{A.4})$$

In this basis the Hamiltonian of the free atom can be written as

$$H_0 = \frac{\hbar\omega_0}{2}(|2\rangle\langle 2| - |1\rangle\langle 1|) \quad (\text{A.5})$$

and a convenient choice for an operator basis in this space is

$$\mathbf{1} = |1\rangle\langle 1| + |2\rangle\langle 2| \quad (\text{A.6})$$

$$\sigma_z = |2\rangle\langle 2| - |1\rangle\langle 1| \quad (\text{A.7})$$

$$\sigma^+ = |2\rangle\langle 1| \quad (\text{A.8})$$

$$\sigma^- = |1\rangle\langle 2| \quad (\text{A.9})$$

If we apply these operators to some arbitrary state $|\Psi\rangle = c_1|1\rangle + c_2|2\rangle$ we get

$$\sigma_z|\Psi\rangle = c_2|2\rangle - c_1|1\rangle \quad (\text{A.10})$$

$$\sigma^+|\Psi\rangle = c_1|2\rangle \quad (\text{A.11})$$

$$\sigma^-|\Psi\rangle = c_2|1\rangle \quad (\text{A.12})$$

The physical meaning of the (non Hermitian) operators σ^+ and σ^- is that they generate transitions from the ground to the excited state and vice versa. The operator σ_z is Hermitian and its expectation value therefore an observable quantity. The operators σ^+ and σ^- can be replaced by the Hermitian operators $\sigma_{\mathbf{x},\mathbf{y}}$

$$\sigma_{\mathbf{x}} = \sigma^+ + \sigma^- \quad (\text{A.13})$$

$$\sigma_{\mathbf{y}} = -i\sigma^+ + i\sigma^- \quad (\text{A.14})$$

The operators $\sigma_{\mathbf{x},\mathbf{y},\mathbf{z}}$ are also called the Pauli matrices and will be used later in the evaluation. In this basis we can now write the Hamiltonian of the free atom as

$$H_0 = \frac{\hbar\omega_0}{2}\sigma_z \quad (\text{A.15})$$

The Hamiltonian for the interaction of an atom with the electromagnetic field can be derived from the coupling between a charged particle of mass m and charge q at the position \mathbf{r} with the electric field $E(\mathbf{r}, t)$ of an electromagnetic wave. Note that in frequency standards (atomic clocks) also other relevant types of interactions, e.g. magnetic dipole and electric quadrupole have to be considered at the extreme precision that can now be reached. However, in this description we only look at the lowest order interaction. The electric dipole moment \mathbf{d} is determined by the position operator \mathbf{r} through

$$\mathbf{d} = -e_0\mathbf{r} \quad (\text{A.16})$$

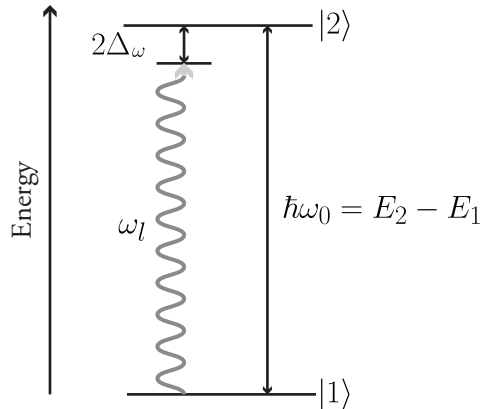


FIGURE A.1: Schematic picture of a two level atom with energies E_1 and E_2 that are separated by an energy interval of $\hbar\omega_0$. The frequency of the applied field is indicated by ω_l . The detuning of the laser with respect to the resonance (Δ_ω) is defined in Eq. A.32

where e_0 is the elementary charge. The expectation value for the dipole moment of an atom in an arbitrary state is equal to

$$\langle \Psi | \mathbf{d} | \Psi \rangle = -e_0 (|c_1|^2 \langle 1 | \mathbf{r} | 1 \rangle + |c_2|^2 \langle 2 | \mathbf{r} | 2 \rangle + c_1 c_2^* \langle 2 | \mathbf{r} | 1 \rangle + c_2 c_1^* \langle 1 | \mathbf{r} | 2 \rangle) \quad (\text{A.17})$$

Atoms (but also some molecules) do not have a permanent dipole due to symmetry, therefore the state dipole moments $\langle n | \mathbf{r} | n \rangle$ are equal to zero and only the transition dipole moments remain. This results in

$$\langle \Psi | \mathbf{d} | \Psi \rangle = -e_0 (c_1 c_2^* \langle 2 | \mathbf{r} | 1 \rangle + c_2 c_1^* \langle 1 | \mathbf{r} | 2 \rangle) \quad (\text{A.18})$$

By defining the dipole moments that connect the ground and excited state as

$$\mathbf{d}_{12} = e_0 \langle 1 | \mathbf{r} | 2 \rangle \quad \mathbf{d}_{21} = \mathbf{d}_{12}^* = e_0 \langle 2 | \mathbf{r} | 1 \rangle \quad (\text{A.19})$$

and using the definitions of σ^+ and σ^- , Eq. A.18 can be re-written as

$$\langle \Psi | \mathbf{d} | \Psi \rangle = -\langle \Psi | \mathbf{d}_{12} \sigma^- + \mathbf{d}_{21} \sigma^+ | \Psi \rangle \quad (\text{A.20})$$

Since this holds for an arbitrary state the dipole operator can be represented as

$$\mathbf{d} = -(\mathbf{d}_{12} \sigma^- + \mathbf{d}_{21} \sigma^+) \quad (\text{A.21})$$

The Hamiltonian of an induced electric dipole by an external electromagnetic field is given by

$$H_{int} = -\mathbf{d} \cdot E(\mathbf{r}, t) \quad (\text{A.22})$$

If we assume monochromatic radiation then the electric field at the position of the atom \mathbf{r}_0 is described by

$$E(\mathbf{r}_0, t) = \frac{1}{2} E_0 e^{i\omega_l t} \hat{e} + E_0^* e^{-i\omega_l t} \hat{e} \quad (\text{A.23})$$

where ω_l is the (angular) frequency of the radiation, E_0 the complex amplitude of the field and \hat{e} denotes direction of the polarization. Plugging this and the previously defined \mathbf{d} into Eq. A.22 and using the definition for the Rabi frequency

$$\Omega_R \equiv \Omega = \frac{E_0^*}{2\hbar} \mathbf{d}_{21} \cdot \hat{e} \quad (\text{A.24})$$

leads to an expression for the interaction Hamiltonian as:

$$H_{int} = \hbar \sigma^- (\tilde{\Omega}^* e^{i\omega_l t} + \Omega^* e^{-i\omega_l t}) + \hbar \sigma^+ (\tilde{\Omega} e^{i\omega_l t} + \Omega e^{-i\omega_l t}) \quad (\text{A.25})$$

With this the full Hamiltonian can be written down as

$$H_{tot} = \hbar \left(\frac{\omega_0}{2} \sigma_z + (\tilde{\Omega}^* e^{i\omega_l t} + \Omega^* e^{-i\omega_l t}) \sigma^- + (\tilde{\Omega} e^{i\omega_l t} + \Omega e^{-i\omega_l t}) \sigma^+ \right) \quad (\text{A.26})$$

In the "Schrödinger picture" the operators are fixed while the Schrödinger equation changes the state vectors with time. In order to go to this picture we remove the time dependence from the interaction Hamiltonian by applying the unitary transformation that describes a rotation at the frequency of the applied electromagnetic field

$$U = e^{-\frac{i\omega_l}{2} t} |1\rangle\langle 1| + e^{\frac{i\omega_l}{2} t} |2\rangle\langle 2| \quad (\text{A.27})$$

which relates the initial state $|\Psi\rangle$ to the transformed state $|\bar{\Psi}\rangle$ via the multiplication

$$|\Psi(t)\rangle = U |\bar{\Psi}(t)\rangle \quad (\text{A.28})$$

By inserting this transformation into the Schrödinger equation and by multiplying the equation from the left with U^\dagger we find the transformed Hamiltonian to be

$$i\hbar U^\dagger (\partial_t U |\bar{\Psi}\rangle + U \partial_t |\bar{\Psi}\rangle) = U^\dagger H_{tot} U |\bar{\Psi}\rangle \quad (\text{A.29})$$

$$\bar{H} = -i\hbar U^\dagger \partial_t U + U^\dagger H_{tot} U |\bar{\Psi}\rangle \quad (\text{A.30})$$

Filling in for U and H_{tot} results in

$$\bar{H}_{tot} = \hbar \frac{\omega_0 - \omega_l}{2} \sigma_z + \hbar (\tilde{\Omega}^* e^{i2\omega_l t} + \Omega^*) \sigma^- + \hbar (\tilde{\Omega} e^{i2\omega_l t} + \Omega) \sigma^+ \quad (\text{A.31})$$

The remaining time dependent terms in the Hamiltonian oscillate at $2\omega_l$. If we assume that we are close to resonance, i.e. $\omega_l \approx \omega_0$, this term is assumed to average out quickly over timescales relevant to the interaction and are therefore neglected, a procedure known as the rotating-wave approximation. If we define the detuning of the laser field with respect to the atomic resonance as (see Fig. A.1)

$$\Delta_\omega = \frac{\omega_0 - \omega_l}{2} \quad (\text{A.32})$$

Then the approximated time-independent Hamiltonian becomes

$$\bar{H}_{tot} = \hbar (\Delta_\omega \sigma_z + \Omega^* \sigma^- + \Omega \sigma^+) \quad (\text{A.33})$$

This Hamiltonian can be re-written in the form of a vector product of $\mathbf{r} \equiv (Re(\Omega), -Im(\Omega), \Delta)$ with $\sigma = (\sigma_x, \sigma_y, \sigma_z)$, where $\sigma_{\mathbf{x},\mathbf{y},\mathbf{z}}$ are the previously defined Pauli matrices, leading to the simplified form of the Hamiltonian

$$\bar{H}_{tot} = \hbar (\mathbf{r} \cdot \sigma) \quad (\text{A.34})$$

The general expression for the wave function in the Schrödinger picture (no time dependence in the operator) is found by integrating the Schrödinger equation

$$|\Psi(t)\rangle = e^{\frac{-i\hat{O}}{\hbar}t} |\Psi(0)\rangle \quad (\text{A.35})$$

A quantum operator as the argument of the exponential is defined in terms of the power series expansion

$$e^{\frac{-i\hat{O}}{\hbar}t} = \sum_{n=0}^{+\infty} \frac{1}{n!} \left(\frac{i}{\hbar} \hat{O} t \right)^n \quad (\text{A.36})$$

Doing the expansion for the Hamiltonian and using the commutation relations for the Pauli matrices, $[\sigma_i, \sigma_j]_+ = 0$ and $\sigma_i^2 = \mathbf{1}$, the exponential can be written as

$$\mathcal{M}_{int} = e^{\frac{-i\bar{H}}{\hbar}t} = \cos(rt) \mathbf{1} + i \frac{\mathbf{r} \cdot \sigma}{|\mathbf{r}|} \sin(rt) \quad (\text{A.37})$$

where $r = |\mathbf{r}| = \sqrt{\Omega^2 + \Delta_\omega^2}$. The state vector $|\Psi(t)\rangle$ can now be found by applying this operator to the initial state vector $|\Psi(0)\rangle$ and the coefficients c_1 and c_2 are determined

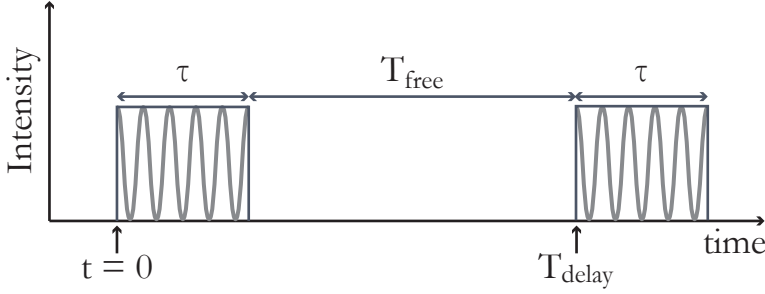


FIGURE A.2: Schematic overview of two square pulse sequence, each of duration τ separated by a field-free period of T_{free} . $t = 0$ and pulse delay T_{delay} are defined at the onset of the first and second pulse respectively.

by the projection on each state, i.e.

$$\langle 1|\Psi(\tau)\rangle = c_1 = \langle 1|\mathcal{M}_{int}(\tau)|\Psi(0)\rangle \quad (\text{A.38a})$$

$$\langle 2|\Psi(\tau)\rangle = c_2 = \langle 2|\mathcal{M}_{int}(\tau)|\Psi(0)\rangle \quad (\text{A.38b})$$

If we assume the initial conditions at $t = 0$ to be $|\Psi(0)\rangle = |1\rangle$, i.e. all the population starts out in the ground state, then the evolution of the excited state is given by

$$c_2 = \cos(rt)\langle 2|\mathbf{1}|1\rangle + i\frac{\langle 2|\mathbf{r}\cdot\sigma|1\rangle}{r}\sin(rt) \quad (\text{A.39})$$

$$\Rightarrow c_2 = i\frac{\Omega}{r}\sin(rt) \quad (\text{A.40})$$

The probability to find an atom in the excited state upon a measurement is then given by the squared value, $|c_2|^2$, which results in

$$|c_2|^2 = \frac{\Omega^2}{r^2}\sin^2(rt) \quad (\text{A.41})$$

We see that the probability to find an atom in the excited state oscillates with the frequency r which is determined by the detuning of the radiation from the atomic resonance and the Rabi frequency Ω which itself determined by the transition dipole moment and the intensity of applied radiation.

We now want to study the probability of finding the atom in the excited state after interaction with two square pulses (as an approximation of the excitation process) of duration τ separated by a time interval T_{free} where no field is present, see Fig. A.2. The Hamiltonian for the field-free period is given by Eq. A.37 with Ω set to zero,

which then reduces to

$$\mathcal{M}_{free} = e^{-i\Delta\omega T_{free}}|1\rangle\langle 1| + e^{i\Delta\omega T_{free}}|2\rangle\langle 2| \quad (\text{A.42})$$

This neglects spontaneous decay and other de-phasing mechanisms such as Doppler broadening, it however does not alter the shape of the result. If we again assume the atoms are initially in the ground state then the excitation amplitude after two pulses can now be described by a series of multiplications

$$\langle 2|\Psi(\tau + T_{free} + \tau)\rangle = \langle 2|\mathcal{M}_{int}(\tau)\mathcal{M}_{free}(T_{free})\mathcal{M}_{int}(\tau)|1\rangle \quad (\text{A.43})$$

Working out the multiplication gives the amplitude of the state vector $|2\rangle$ at time $t = \tau + T_{free} + \tau$

$$c_2(t) = \frac{2\Omega}{r} \sin(r\tau) \left(\cos(r\tau) \cos(\Delta\omega T_{free}) - \frac{\Delta\omega}{r} \sin(r\tau) \sin(\Delta\omega T_{free}) \right) \quad (\text{A.44})$$

so that the probability to find the atom in the excited state upon a measurement becomes

$$|c_2(t)|^2 = \frac{4\Omega^2}{r^2} \sin^2(r\tau) \left(\cos(r\tau) \cos(\Delta\omega T_{free}) - \frac{\Delta\omega}{r} \sin(r\tau) \sin(\Delta\omega T_{free}) \right)^2 \quad (\text{A.45})$$

In typical Ramsey-type spectroscopy the delay time between the excitation pulses is kept constant and the frequency of the interrogation field is scanned with respect to the resonance. In order to conveniently describe optical Ramsey fringes where the delay time between the two excitation pulses is varied and the frequency of the laser is kept constant we need to make the substitution $T_{free} = \Delta t - \tau$. In addition we need incorporate the possibility of potential phase shifts between the two excitation pulses Φ .

$$|c_2|^2 = \frac{4\Omega^2}{r^2} \sin^2(r\tau) \left(\cos(r\tau) \cos\left(\Delta\omega\Delta t - \Delta\omega\tau - \frac{\Phi}{2}\right) - \frac{\Delta\omega}{r} \sin(r\tau) \sin\left(\Delta\omega\Delta t - \Delta\omega\tau - \frac{\Phi}{2}\right) \right)^2 \quad (\text{A.46})$$

In the situation of excitation with a phase locked pulse pair changing the pulse delay Δt leads to an effective phase change according to $-\omega_l\Delta t$. In addition, other potential sources of phase change ($\Delta\phi$) have to be carefully considered and analyzed, leading to $\Phi = -\omega_l\Delta t + \Delta\phi$. One example of a source of phase shift is the carrier-envelope phase shift, $\Delta\phi_{ceo}$, when the pulses are derived from a frequency-comb laser.

This phase shift is generally not equal to zero and has to be accounted for in the analysis of the signals. In practice, to maximize the signal the laser is tuned as close to resonance as possible, i.e. $\omega_l \approx \omega_0$ and $\Delta_\omega \approx 0$, than Eq. A.46 can be reduced to

$$|c_2|^2 = 4 \sin^2(\Omega\tau) \cos^2(\Omega\tau) \cos^2\left(\frac{\omega_0\Delta t - \Delta\phi}{2}\right) \quad (\text{A.47})$$

This can be cast into the even simpler form describing Ramsey interference fringes as function of the pulse delay time

$$|c_2|^2 = \frac{A_0}{2} \{1 + \cos(\omega_0\Delta t - \Delta\phi)\} \quad (\text{A.48})$$

with

$$A_0 = 4 \sin^2(\Omega\tau) \cos^2(\Omega\tau) \quad (\text{A.49})$$

Bibliography

- [1] N. Bohr. On the constitution of atoms and molecules. *Philosophical Magazine*, **26**(153), 476–502, 1913.
- [2] A. A. Michelson and E. W. Morley. On a method of making the wave-length of sodium light the actual and practical standard of length. *Philosophical Magazine*, **24**(151), 463–466, 1887.
- [3] P. A. M. Dirac. The Quantum Theory of the Electron. *Proceedings of the Royal Society of London*, **117**, 610–624, 1928.
- [4] W. E. Lamb and R. C. Retherford. Fine structure of the hydrogen atom by a microwave method. *Physical Review*, **72**(3), 241–243, 1947.
- [5] W. E. Lamb and R. C. Retherford. Fine structure of the hydrogen atom. Part I. *Physical Review*, **79**(4), 549–572, 1950.
- [6] H. Bethe. The electromagnetic shift of energy levels. *Physical Review*, **72**(4), 339–341, 1947.
- [7] F. J. Dyson. The Radiation Theories of Tomonaga, Schwinger, and Feynman. *Physical Review*, **75**(3), 486–502, 1949.
- [8] F. Dyson. Divergence of Perturbation Theory in Quantum Electrodynamics. *Physical Review*, **85**(4), 631–632, 1952.
- [9] J. E. Nafe, E. B. Nelson, and I. I. Rabi. The Hyperfine Structure of Atomic Hydrogen and Deuterium. *Physical Review*, **71**(12), 914–915, 1947.
- [10] G. Breit. Does the electron have an intrinsic magnetic moment? *Physical Review*, **7**, 984, 1947.
- [11] J. Schwinger. On quantum-electrodynamics and the magnetic moment of the electron. *Physical Review*, **73**(4), 416–417, 1948.
- [12] R. Karplus and N. M. Kroll. Fourth-Order Corrections in Quantum Electrodynamics and the Magnetic Moment of the Electron. *Physical Review*, **77**(4), 536–549, 1950.
- [13] S. Koenig, A. Prodell, and P. Kusch. The Anomalous Magnetic Moment of the Electron. *Physical Review*, **88**(2), 191–199, 1952.

- [14] F. Biraben. Spectroscopy of atomic hydrogen. *The European Physical Journal Special Topics*, **172**, 109–119, 2009.
- [15] T. Aoyama, M. Hayakawa, T. Kinoshita, and M. Nio. Complete Tenth-Order QED Contribution to the Muon $g-2$. *Physical Review Letters*, **109**, 111808, 2012.
- [16] D. Hanneke, S. Fogwell, and G. Gabrielse. New Measurement of the Electron Magnetic Moment and the Fine Structure Constant. *Physical Review Letters*, **100**(12), 120801, 2008.
- [17] P. Clade, E. D. Mirandes, M. Cadoret, C. Schwob, F. Nez, L. Julien, and F. Biraben. Determination of the Fine Structure Constant Based on Bloch Oscillations of Ultracold Atoms in a Vertical Optical Lattice. *Physical Review Letters*, **96**, 033001, 2006.
- [18] V. Gerginov, K. Calkins, C. E. Tanner, J. McFerrari, S. Diddams, A. Bartels, and L. Hollberg. Optical frequency measurements of $6s^2S_{1/2} - 6p^2P_{1/2}(D_1)$ transitions in ^{133}Cs and their impact on the fine-structure constant. *Physical Review A*, **73**, 032504, 2006.
- [19] R. H. Parker, C. Yu, W. Zhong, B. Estey, and H. Müller. Measurement of the fine-structure constant as a test of the Standard Model. **360**, 191–195, 2018.
- [20] C. G. Parthey, A. Matveev, J. Alnis, B. Bernhardt, A. Beyer, R. Holzwarth, A. Maistrou, R. Pohl, K. Predehl, T. Udem, T. Wilken, N. Kolachevsky, M. Abgrall, D. Rovera, C. Salomon, P. Laurent, and T. W. Hänsch. Improved Measurement of the Hydrogen 1S-2S Transition Frequency. *Physical Review Letters*, **107**, 203001, 2011.
- [21] A. Matveev, C. G. Parthey, K. Predehl, J. Alnis, A. Beyer, R. Holzwarth, T. Udem, T. Wilken, N. Kolachevsky, M. Abgrall, D. Rovera, C. Salomon, P. Laurent, G. Grosche, O. Terra, T. Legero, H. Schnatz, S. Weyers, B. Altschul, and T. W. Hänsch. Precision measurement of the hydrogen 1S-2S frequency via a 920-km fiber link. *Physical Review Letters*, **110**, 230801, 2013.
- [22] V. A. Yerokhin and V. M. Shabaev. Lamb Shift of $n = 1$ and $n = 2$ States of Hydrogen-like Atoms, $1 \leq Z \leq 110$. *Journal of Physical and Chemical Reference Data*, **44**(3), 33103, 2015.
- [23] R. Rosenfelder. Coulomb corrections to elastic electron-proton scattering and the proton charge radius. *Physics Letters B*, **479**, 381–386, 2000.
- [24] I. Sick. On the rms-radius of the proton. *Physics Letters B*, **576**, 62–67, 2003.

- [25] I. Sick. Form Factors and Radii of Light Nuclei. *Journal of Physical and Chemical Reference Data*, **44**(3), 31213, 2015.
- [26] P. J. Mohr, B. N. Taylor, and D. B. Newell. CODATA Recommended Values of the Fundamental Physical Constants:2006. *Reviews of Modern Physics*, **80**(2), 633, 2008.
- [27] P. J. Mohr, B. N. Taylor, and D. B. Newell. CODATA recommended values of the fundamental physical constants: 2010. *Reviews of Modern Physics*, **84**(4), 1527–1605, 2012.
- [28] R. Pohl, A. Antognini, F. Nez, F. D. Amaro, F. Biraben, J. M. R. Cardoso, D. S. Covita, A. Dax, S. Dhawan, L. M. P. Fernandes, A. Giesen, T. Graf, T. W. Hänsch, P. Indelicato, L. Julien, C.-Y. Kao, P. Knowles, E.-O. Le Bigot, Y.-W. Liu, J. a. M. Lopes, L. Ludhova, C. M. B. Monteiro, F. Mulhauser, T. Nebel, P. Rabinowitz, J. M. F. Dos Santos, L. a. Schaller, K. Schuhmann, C. Schwob, D. Taqqu, J. F. C. a. Veloso, and F. Kottmann. The size of the proton. *Nature*, **466**, 213–216, 2010.
- [29] A. Antognini, F. Nez, K. Schuhmann, F. D. Amaro, F. Biraben, J. M. R. Cardoso, D. S. Covita, A. Dax, S. Dhawan, M. Diepold, L. M. P. Fernandes, A. Giesen, A. L. Gouvea, T. Graf, T. W. Hänsch, P. Indelicato, L. Julien, C.-Y. Kao, P. Knowles, F. Kottmann, E.-O. Le Bigot, Y.-W. Liu, J. a. M. Lopes, L. Ludhova, C. M. B. Monteiro, F. Mulhauser, T. Nebel, P. Rabinowitz, J. M. F. dos Santos, L. a. Schaller, C. Schwob, D. Taqqu, J. F. C. a. Veloso, J. Vogelsang, and R. Pohl. Proton structure from the measurement of 2S-2P transition frequencies of muonic hydrogen. *Science*, **339**, 417–420, 2013.
- [30] H. S. Margolis. How Big Is the Proton? *Science*, **339**, 405–406, 2013.
- [31] J. C. Bernauer and R. Pohl. The Proton Radius Problem. *Scientific American*, **310**(2), 32–39, 2014.
- [32] P. J. Mohr, D. B. Newell, and B. N. Taylor. CODATA Recommended Values of the Fundamental Physical Constants:2014. *Reviews of Modern Physics*, **88**, 035009, 2016.
- [33] R. Pohl, R. Gilman, G. A. Miller, and K. Pachucki. Muonic Hydrogen and the Proton Radius Puzzle. *Annual Review of Nuclear and Particle Science*, **63**, 175–204, 2013.
- [34] C. E. Carlson. The proton radius puzzle. *Progress in Particle and Nuclear Physics*, **82**, 59–77, 2015.

- [35] R. Pohl. Laser spectroscopy of muonic hydrogen and the puzzling proton. *Journal of the Physical Society of Japan*, **85**, 091003, 2016.
- [36] R. Pohl, F. Nez, L. M. P. Fernandes, A. D. Fernando, F. Biraben, J. M. R. Cardoso, D. S. Covita, A. Dax, S. Dhawan, M. Diepold, A. Giesen, A. L. Gouvea, T. Graf, T. W. Hänsch, P. Indelicato, L. Julien, P. Knowles, F. Kottmann, E.-O. Le Bigot, Y.-W. Liu, J. A. M. Lopes, L. Ludhova, C. M. B. Monteiro, F. Mulhauser, T. Nebel, P. Rabinowitz, J. M. F. dos Santos, L. A. Schaller, K. Schuhmann, C. Schwob, D. Taqqu, J. F. C. A. Veloso, A. Antognini, and The CREMA Collaboration. Laser spectroscopy of muonic deuterium. *Science*, **353**(6300), 669–672, 2016.
- [37] A. Beyer, L. Maisenbacher, A. Matveev, R. Pohl, K. Khabarova, A. Grinin, T. Lamour, D. Yost, T. Hänsch, N. Kolachevsky, and T. Udem. The Rydberg constant and proton size from atomic hydrogen. *Science*, **358**(6359), 79–85, 2017.
- [38] H. Fleurbaey, S. Galtier, S. Thomas, M. Bonnaud, L. Julien, F. Biraben, F. Nez, M. Abgrall, and J. Guéna. New measurement of the $1S-3S$ transition frequency of hydrogen: contribution to the proton charge radius puzzle. *Physical Review Letters*, **120**, 183001, 2018.
- [39] M. Niering, R. Holzwarth, J. Reichert, P. Pokasov, T. Udem, M. Weitz, T. W. Hänsch, P. Lemonde, G. Santarelli, M. Abgrall, P. Laurent, C. Salomon, and A. Clairon. Measurement of the Hydrogen $1S-2S$ Transition Frequency by Phase Coherent Comparison with a Microwave Cesium Fountain Clock. *Physical Review Letters*, **84**(24), 5496–5499, 2000.
- [40] B. de Beauvoir, C. Schwob, O. Acef, L. Jozefowski, L. Hilico, F. Nez, L. Julien, A. Clairon, and F. Biraben. Metrology of the hydrogen and deuterium atoms: Determination of the Rydberg constant and Lamb shifts. *Eur. Phys. J. D*, **12**(1), 61–93, 2000.
- [41] C. Schwob, L. Jozefowski, B. de Beauvoir, L. Hilico, F. Nez, L. Julien, F. Biraben, O. Acef, J.-J. Zondy, and A. Clairon. Optical Frequency Measurement of the $2S-12D$ Transitions in Hydrogen and Deuterium: Rydberg Constant and Lamb Shift Determinations. *Physical Review Letters*, **82**(25), 4960–4963, 1999.
- [42] J. Arrington. An Examination of Proton Charge Radius Extractions from $e-p$ Scattering Data. *Journal of Physical and Chemical Reference Data*, **44**(3), 31203, 2015.

- [43] I. Sick. Precise radii of light nuclei from electron scattering. In *Precision physics of simple atoms and molecules*, pages 57–75. Springer, 2008.
- [44] E. Kraus, K. E. Mesick, A. White, R. Gilman, and S. Strauch. Polynomial fits and the proton radius puzzle. *Physical Review C*, **90**, 045206, 2014.
- [45] I. T. Lorenz, U. G. Meißner, H. W. Hammer, and Y. B. Dong. Theoretical constraints and systematic effects in the determination of the proton form factors. *Physical Review D*, **91**, 014023(18), 2015.
- [46] M. Herrmann, M. Haas, U. D. Jentschura, F. Kottmann, D. Leibfried, G. Saathoff, C. Gohle, A. Ozawa, V. Batteiger, S. Knünz, N. Kolachevsky, H. A. Schüssler, T. W. Hänsch, and T. Udem. Feasibility of coherent xuv spectroscopy on the 1S-2S transition in singly ionized helium. *Physical Review A*, **79**, 052505, 2009.
- [47] A. Antognini, F. Biraben, J. M. Cardoso, D. S. Covita, A. Dax, L. M. Fernandes, A. L. Gouvea, T. Graf, T. W. Hänsch, M. Hildebrandt, P. Indelicato, L. Julien, K. Kirch, F. Kottmann, Y.-W. Liu, C. M. Monteiro, F. Mulhauser, T. Nebel, F. Nez, J. M. dos Santos, K. Schuhmann, D. Taqqu, J. F. Veloso, A. Voss, and R. Pohl. Illuminating the proton radius conundrum: the μHe^+ Lamb shift. *Canadian Journal of Physics*, **89**, 47–57, 2011.
- [48] R. V. Rooij, J. S. Borbely, J. Simonet, M. D. Hoogerland, K. S. E. Eikema, R. A. Rozendaal, and W. Vassen. Frequency Metrology in Quantum Degenerate Helium : Direct Measurement of the $2^3S_1 \rightarrow 2^1S_0$ Transition. *Science*, **333**, 196–199, 2011.
- [49] D. Shiner, R. Dixson, and V. Vedantham. Three-Nucleon Charge Radius: A Precise Laser Determination Using ^3He . *Physical Review Letters*, **74**(18), 3553–3556, 1995.
- [50] P. Cancio Pastor, L. Consolino, G. Giusfredi, P. De Natale, M. Inguscio, V. A. Yerokhin, and K. Pachucki. Frequency Metrology of Helium around 1083 nm and Determination of the Nuclear Charge Radius. *Physical Review Letters*, **108**, 143001, 2012.
- [51] K. Pachucki and J. Komasa. Schrödinger equation solved for the hydrogen molecule with unprecedented accuracy. *Journal of Chemical Physics*, **144**, 164306, 2016.

- [52] M. Puchalski, J. Komasa, P. Czachorowski, and K. Pachucki. Complete $\alpha^6 m$ Corrections to the Ground State of H_2 . *Physical Review Letters*, **117**, 263002, 2016.
- [53] A. L. Schawlow. Spectroscopy in a new light. *Reviews of Modern Physics*, **54**(3), 697–707, 1982.
- [54] T. W. Hänsch and H. Walther. Laser spectroscopy and quantum optics. *Reviews of Modern Physics*, **71**(2), S242–S252, 1999.
- [55] H. Schnatz, B. Lipphardt, J. Helmcke, F. Riehle, and G. Zinner. First Phase-Coherent Frequency Measurement of Visible Radiation. *Physical Review Letters*, **76**(1), 18–21, 1996.
- [56] R. Holzwarth, T. Udem, T. W. Hänsch, J. C. Knight, W. J. Wadsworth, and P. S. J. Russell. Optical frequency synthesizer for precision spectroscopy. *Physical Review Letters*, **85**(11), 2264–2267, 2000.
- [57] S. Diddams, D. Jones, J. Ye, S. Cundiff, J. Hall, J. Ranka, R. Windeler, R. Holzwarth, T. Udem, and T. Hänsch. Direct Link between Microwave and Optical Frequencies with a 300 THz Femtosecond Laser Comb. *Physical review letters*, **84**(22), 5102, 2000.
- [58] S. A. Diddams. The evolving optical frequency comb. *Journal of the Optical Society of America B*, **27**(11), B51–B62, 2010.
- [59] F. Krausz and M. Ivanov. Attosecond physics. *Reviews of Modern Physics*, **81**(1), 163–234, 2009.
- [60] C. Gohle, T. Udem, M. Herrmann, J. Rauschenberger, R. Holzwarth, H. A. Schuessler, F. Krausz, and T. W. Hänsch. A frequency comb in the extreme ultraviolet. *Nature*, **436**, 234–237, 2005.
- [61] A. Ozawa, W. Schneider, T. W. Hänsch, T. Udem, and P. Hommelhoff. Phase-stable single-pass cryogenic amplifier for high repetition rate few-cycle laser pulses. *New Journal of Physics*, **11**, 083029, 2009.
- [62] A. Cingoz, D. C. Yost, T. K. Allison, A. Ruehl, M. E. Fermann, I. Hartl, and J. Ye. Direct Frequency Comb Spectroscopy in the Extreme Ultraviolet. *Nature*, **482**, 68–71, 2012.
- [63] S. Witte, R. T. Zinkstok, W. Ubachs, W. Hogervorst, and K. S. E. Eikema. Deep-Ultraviolet Quantum Interference Metrology with Ultrashort Laser Pulses. *Science*, **307**, 400–403, 2005.

- [64] N. Ramsey. A New Molecular Beam Resonance Method. *Physical Review*, **76**(7), 996, 1949.
- [65] N. F. Ramsey. A molecular beam resonance method with separated oscillating fields. *Physical Review*, **78**(6), 695–699, 1950.
- [66] D. Z. Kandula, C. Gohle, T. J. Pinkert, W. Ubachs, and K. S. E. Eikema. XUV frequency-comb metrology on the ground state of helium. *Physical Review A*, **84**(6), 062512, 2011.
- [67] J. Morgenweg, I. Barmes, and K. S. E. Eikema. Ramsey-comb spectroscopy with intense ultrashort laser pulses. *Nature Physics*, **10**, 30–33, 2014.
- [68] J. Morgenweg and K. S. E. Eikema. Ramsey-comb spectroscopy: Theory and signal analysis. *Physical Review A*, **89**, 052510, 2014.
- [69] J. Morgenweg and K. S. E. Eikema. Multi-delay, phase coherent pulse pair generation for precision Ramsey-frequency comb spectroscopy. *Optics Express*, **21**(5), 5275–5286, 2013.
- [70] D. Jones, S. Diddams, J. Ranka, A. Stentz, R. Windeler, J. Hall, and S. Cundiff. Carrier-Envelope Phase Control of Femtosecond Mode-Locked Lasers and Direct Optical Frequency Synthesis. *Science*, **288**, 635–639, 2000.
- [71] S. T. Cundiff, J. Ye, and J. L. Hall. Optical Frequency Synthesis Based on Mode-Locked Lasers. *Review of Scientific Instruments*, **72**(10), 3749–3771, 2001.
- [72] J. Helmcke, G. Wilpers, T. Binnewies, C. Degenhardt, U. Sterr, H. Schnatz, and F. Riehle. Optical frequency standard based on cold Ca atoms. *IEEE Transactions on Instrumentation and Measurement*, **52**(2), 250–254, 2003.
- [73] F. Keilmann, C. Gohle, and R. Holzwarth. Time-domain mid-infrared frequency-comb spectrometer. *Optics Letters*, **29**(13), 1542–1544, 2004.
- [74] A. Schliesser, N. Picque, and T. W. Hänsch. Mid-infrared frequency combs. *Nature Photonics*, **6**(7), 440–449, 2012.
- [75] T. Yasui, Y. Kabetani, E. Saneyoshi, S. Yokoyama, and T. Araki. Terahertz frequency comb by multifrequency-heterodyning photoconductive detection for high-accuracy, high-resolution terahertz spectroscopy. *Applied Physics Letters*, **88**(24), 241104, 2006.

- [76] E. Peters, S. Diddams, P. Fendel, S. Reinhardt, T. W. Hänsch, and T. Udem. A deep-UV optical frequency comb at 205 nm. *Optics Express*, **17**(11), 9183–9190, 2009.
- [77] R. T. Zinkstok, S. Witte, W. Ubachs, W. Hogervorst, and K. S. E. Eikema. Frequency comb laser spectroscopy in the vacuum-ultraviolet region. *Physical Review A*, **73**, 061801, 2006.
- [78] R. J. Jones, K. D. Moll, M. J. Thorpe, and J. Ye. Phase-Coherent Frequency Combs in the Vacuum Ultraviolet via High-Harmonic Generation inside a Femtosecond Enhancement Cavity. *Physical Review Letters*, **94**, 193201, 2005.
- [79] A. K. Mills, T. J. Hammond, M. H. C. Lam, and D. J. Jones. XUV frequency combs via femtosecond enhancement cavities. *Journal of Physics B: Atomic, Molecular and Optical Physics*, **45**(14), 142001, 2012.
- [80] A. Ozawa and Y. Kobayashi. Vuv frequency-comb spectroscopy of atomic xenon. *Physical Review A*, **87**, 022507, 2013.
- [81] I. Coddington, W. C. Swann, L. Nenadovic, and N. R. Newbury. Rapid and precise absolute distance measurements at long range. *Nature Photonics*, **3**, 351–356, 2009.
- [82] D. Kielpinski. Laser cooling of atoms and molecules with ultrafast pulses. *Physical Review A*, **73**, 063407, 2006.
- [83] K. K. Ni, S. Ospelkaus, M. H. G. de Miranda, A. Pe’er, B. Neyenhuis, J. J. Zirbel, S. Kotochigova, P. S. Julienne, D. S. Jin, and J. Ye. A High Phase-Space-Density Gas of Polar Molecules. *Science*, **322**, 231–236, 2008.
- [84] T. Udem, S. A. Diddams, K. R. Vogel, C. W. Oates, E. A. Curtis, W. D. Lee, W. M. Itano, R. E. Drullinger, J. C. Bergquist, and L. Hollberg. Absolute Frequency Measurements of the Hg^+ and Ca Optical Clock Transitions with a Femtosecond Laser. *Physical Review Letters*, **86**(22), 4996–4999, 2001.
- [85] H. S. Margolis, G. P. Barwood, G. Huang, H. A. Klein, S. N. Lea, K. Szymaniec, and P. Gill. Hertz-Level Measurement of the Optical Clock Frequency in a Single $^{88}\text{Sr}^+$ Ion. *Science*, **306**, 1355–1358, 2004.
- [86] T. Rosenband, D. Hume, P. Schmidt, C. Chou, A. Brusch, L. Lorini, W. Oskay, R. Drullinger, T. Fortier, J. Stalnaker, S. Diddams, W. Swann, N. Newbury, W. Itano, D. Wineland, and J. Bergquist. Frequency Ratio of Al^+ and Hg^+

- Single-Ion Optical Clocks; Metrology at the 17th Decimal Place. *Science*, **319**, 1808–1812, 2008.
- [87] O. McDuff and S. Harris. Nonlinear theory of the internally loss-modulated laser. *IEEE Journal of Quantum Electronics*, **3**(3), 101–111, 1967.
- [88] J. N. Eckstein, A. I. Ferguson, and T. W. Hänsch. High-Resolution Two-Photon Spectroscopy with Picosecond Light Pulses. *Physical Review Letters*, **40**(13), 847–850, 1978.
- [89] S. T. Cundiff and J. Ye. Phase stabilization of mode-locked lasers. *Journal of Modern Optics*, **52**(2-3), 201–219, 2005.
- [90] R. Paschotta and U. Keller. Passive mode locking with slow saturable absorbers. *Applied Physics B*, **73**, 653–662, 2001.
- [91] J.-C. Diels and W. Rudolph. *Ultrashort Laser Pulse Phenomena*. Elsevier Science, 2006.
- [92] U. Keller. Recent developments in compact ultrafast lasers. *Nature*, **424**, 831, 2003.
- [93] U. Morgner, F. X. Kärtner, S. H. Cho, Y. Chen, H. A. Haus, J. G. Fujimoto, E. P. Ippen, V. Scheuer, G. Angelow, and T. Tschudi. Sub-two-cycle pulses from a Kerr-lens mode-locked Ti:sapphire laser. *Optics Letters*, **24**(6), 411–413, 1999.
- [94] D. H. Sutter, G. Steinmeyer, L. Gallmann, N. Matuschek, F. Morier-Genoud, U. Keller, V. Scheuer, G. Angelow, and T. Tschudi. Semiconductor saturable-absorber mirror-assisted Kerr-lens mode-locked Ti:sapphire laser producing pulses in the two-cycle regime. *Optics Letters*, **24**(9), 631–633, 1999.
- [95] S. Cundiff and J. Ye. Colloquium: Femtosecond optical frequency combs. *Reviews of Modern Physics*, **75**(1), 325–342, 2003.
- [96] J. Ye and S. T. Cundiff. *Femtosecond optical frequency comb technology: Principle and operation and application*. Springer Science, 2005.
- [97] S. Witte, R. T. Zinkstok, A. L. Wolf, W. Hogervorst, W. Ubachs, and K. S. E. Eikema. A source of 2 terawatt, 2.7 cycle laser pulses based on noncollinear optical parametric chirped pulse amplification. *Optics Express*, **14**(18), 8168–8177, 2006.
- [98] G. Cerullo and S. De Silvestri. Ultrafast optical parametric amplifiers. *Review of Scientific Instruments*, **74**(1), 1–18, 2003.

- [99] A. Ruehl, A. Marcinkevicius, M. E. Fermann, and I. Hartl. 80 W, 120 fs Yb-fiber frequency comb. *Optics Letters*, **35**(18), 3015–3017, 2010.
- [100] D. Z. Kandula, C. Gohle, T. J. Pinkert, W. Ubachs, and K. S. E. Eikema. Extreme Ultraviolet Frequency Comb Metrology. *Physical Review Letters*, **105**, 063001, 2010.
- [101] J. E. Bernard, E. McCullough, and A. J. Alcock. High gain, diode-pumped Nd:YVO₄ slab amplifier. *Optics Communications*, **109**(1), 109–114, 1994.
- [102] J. Morgenweg and K. Eikema. A 1.8 mJ, picosecond Nd:YVO₄ bounce amplifier pump front-end system for high-accuracy XUV-frequency comb spectroscopy. *Laser Physics Letters*, **5**(11), 781–785, 2012.
- [103] R. Lavi, S. Jackel, Y. Tzuk, M. Winik, E. Lebiush, M. Katz, and I. Paiss. Efficient pumping scheme for neodymium-doped materials by direct excitation of the upper lasing level. *Applied Optics*, **38**(36), 7382–7385, 1999.
- [104] T. C. Briles, D. C. Yost, A. Cingöz, J. Ye, and T. R. Schibli. Simple piezoelectric-actuated mirror with 180 kHz servo bandwidth. *Optics Express*, **18**(10), 9739–9746, 2010.
- [105] J. Morgenweg and K. S. E. Eikema. Tailored pulse sequences from an 880 nm pumped Nd:YVO₄ bounce amplifier. *Optics Letters*, **37**(2), 208–210, 2012.
- [106] Y. F. Chen. Design criteria for concentration optimization in scaling diode end-pumped lasers to high powers: influence of thermal fracture. *IEEE Journal of Quantum Electronics*, **35**(2), 234–239, 1999.
- [107] D. J. Farrell and M. J. Damzen. High power scaling of a passively modelocked laser oscillator in a bounce geometry. *Optics Express*, **15**(8), 4781, 2007.
- [108] D. Z. Kandula, A. Renault, C. Gohle, a. L. Wolf, S. Witte, W. Hogervorst, W. Ubachs, and K. S. E. Eikema. Ultrafast double-pulse parametric amplification for precision Ramsey metrology. *Optics Express*, **16**(10), 7071–7082, 2008.
- [109] A. Renault, D. Z. Kandula, S. Witte, a. L. Wolf, R. T. Zinkstok, W. Hogervorst, and K. S. E. Eikema. Phase stability of terawatt-class ultrabroadband parametric amplification. *Optics Letters*, **32**(16), 2363–2365, 2007.
- [110] M. Takeda, H. Ina, and S. Kobayashi. Fourier-transform method of fringe-pattern analysis for computer-based topography and interferometry. *Journal of the Optical Society of America*, **72**(1), 156–160, 1982.

- [111] S. Witte. *Terawatt-intensity few-cycle laser pulses*. PhD thesis, VU University Amsterdam, 2007.
- [112] J. A. Armstrong, N. Bloembergen, J. Ducuing, and P. S. Pershan. Interactions between light waves in a nonlinear dielectric. *Physical Review*, **127**(6), 1918–1939, 1962.
- [113] R. Baumgartner and R. Byer. Optical parametric amplification. *IEEE Journal of Quantum Electronics*, **15**(6), 432–444, 1979.
- [114] J. Morgenweg. *Ramsey-comb spectroscopy*. PhD thesis, VU University Amsterdam, 2014.
- [115] A. Wicht, J. M. Hensley, E. Sarajlic, and S. Chu. A Preliminary Measurement of the Fine Structure Constant Based on Atom Interferometry. *Physica Scripta*, **T102**, 82–88, 2002.
- [116] R. Bouchendira, P. Cladé, S. Guellati-Khélifa, F. Nez, and F. Biraben. New Determination of the Fine Structure Constant and Test of the Quantum Electrodynamics. *Physical Review Letters*, **106**, 080801, 2011.
- [117] D. C. Yost, A. Matveev, A. Grinin, E. Peters, L. Maisenbacher, A. Beyer, R. Pohl, N. Kolachevsky, K. Khabarova, T. W. Hänsch, and T. Udem. Spectroscopy of the hydrogen 1S-3S transition with chirped laser pulses. *Physical Review A*, **93**, 042509, 2016.
- [118] S. Galtier, H. Fleurbaey, S. Thomas, L. Julien, F. Biraben, and F. Nez. Progress in Spectroscopy of the 1S-3S Transition in Hydrogen. *Journal of Physical and Chemical Reference Data*, **44**, 031201, 2015.
- [119] R. P. M. J. W. Notermans and W. Vassen. High-Precision Spectroscopy of the Forbidden $2^3S_1 \rightarrow 2^1P_1$ Transition in Quantum Degenerate Metastable Helium. *Physical Review Letters*, **112**, 253002, 2014.
- [120] J. Biesheuvel, J. P. Karr, L. Hilico, K. S. E. Eikema, W. Ubachs, and J. C. J. Koelemeij. Probing QED and fundamental constants through laser spectroscopy of vibrational transitions in HD^+ . *Nature Communications*, **7**, 10385, 2016.
- [121] P. Beiersdorfer. Testing QED and atomic-nuclear interactions with high- Z ions. *Journal of Physics B: Atomic, Molecular and Optical Physics*, **43**, 074032, 2010.
- [122] A. Antognini, K. Schuhmann, F. D. Amaro, P. Amaro, and F. Biraben. Experiments towards resolving the proton charge radius puzzle. *EPJ Web of Conferences*, **113**, 01006, 2016.

- [123] A. Beyer, C. G. Parthey, N. Kolachevsky, J. Alnis, K. Khabarova, R. Pohl, E. Peters, D. C. Yost, A. Matveev, K. Predehl, S. Droste, T. Wilken, R. Holzwarth, T. W. Hänsch, M. Abgrall, D. Rovera, C. Salomon, P. Laurent, and T. Udem. Precision Spectroscopy of Atomic Hydrogen. *Journal of Physics: Conference Series*, **467**, 012003, 2013.
- [124] J. Komasa, K. Piszczatowski, G. Łach, M. Przybytek, B. Jeziorski, and K. Pachucki. Quantum Electrodynamics Effects in Rovibrational Spectra of Molecular Hydrogen. *Journal of Chemical Theory and Computation*, **7**, 3105–3115, 2011.
- [125] W. Ubachs, J. C. J. Koelemeij, K. S. E. Eikema, and E. J. Salumbides. Physics beyond the Standard Model from hydrogen spectroscopy. *Journal of Molecular Spectroscopy*, **320**, 1–12, 2016.
- [126] B. Gross, A. Huber, M. Niering, M. Weitz, and T. W. Hänsch. Optical Ramsey spectroscopy of atomic hydrogen. *Europhysics Letters*, **44**(2), 186–191, 1998.
- [127] A. Ozawa and Y. Kobayashi. Chirped-pulse direct frequency-comb spectroscopy of two-photon transitions. *Physical Review A*, **86**, 022514, 2012.
- [128] I. Barmes, S. Witte, and K. S. E. Eikema. High-precision spectroscopy with counterpropagating femtosecond pulses. *Physical Review Letters*, **111**, 023007, 2013.
- [129] S. Hannemann, E. J. Salumbides, and W. Ubachs. Reducing the first-order Doppler shift in a Sagnac interferometer. *Optics Letters*, **32**(11), 1381–1383, 2007.
- [130] E. Gilabert, B. Lavielle, B. Thomas, S. Topin, F. Pointurier, and C. Moulin. Ultratrace analysis of krypton isotopes by resonant ionization spectroscopy-time of flight mass spectrometry (RIS-TOF). *Journal of Analytic Atomic Spectrometry*, **31**, 994–1001, 2016.
- [131] G. D. Dickenson, M. L. Niu, E. J. Salumbides, J. Komasa, K. S. E. Eikema, K. Pachucki, and W. Ubachs. Fundamental vibration of molecular hydrogen. *Physical Review Letters*, **110**, 193601, 2013.
- [132] W. Heitler and F. London. Wechselwirkung neutraler Atome und homöopolare Bindung nach der Quantenmechanik. *Zeitschrift für Physik*, **44**(6-7), 455–472, 1927.

- [133] J. Liu, E. J. Salumbides, U. Hollenstein, J. C. J. Koelemeij, K. S. E. Eikema, W. Ubachs, and F. Merkt. Determination of the ionization and dissociation energies of the hydrogen molecule. *Journal of Chemical Physics*, **130**, 174306, 2009.
- [134] J. Liu, D. Sprecher, C. Jungen, W. Ubachs, and F. Merkt. Determination of the ionization and dissociation energies of the deuterium molecule (D_2). *Journal of Chemical Physics*, **132**, 154301, 2010.
- [135] E. J. Salumbides, G. D. Dickenson, T. I. Ivanov, and W. Ubachs. QED effects in molecules: Test on rotational quantum states of H_2 . *Physical Review Letters*, **107**, 043005, 2011.
- [136] M. L. Niu, E. J. Salumbides, and W. Ubachs. Communication: Test of quantum chemistry in vibrationally hot hydrogen molecules. *Journal of Chemical Physics*, **143**, 081102, 2015.
- [137] T. M. Trivikram, M. L. Niu, P. Wcislo, W. Ubachs, and E. J. Salumbides. Precision measurements and test of molecular theory in highly excited vibrational states of H_2 ($\nu = 11$). *Applied Physics B*, **122**, 294, 2016.
- [138] K. Pachucki and J. Komasa. Accurate adiabatic correction in the hydrogen molecule. *Journal of Chemical Physics*, **141**, 224103, 2014.
- [139] K. Pachucki and J. Komasa. Leading order nonadiabatic corrections to rovibrational levels of H_2 , D_2 and T_2 . *Journal of Chemical Physics*, **143**, 034111, 2015.
- [140] E. J. Salumbides, J. C. J. Koelemeij, J. Komasa, K. Pachucki, K. S. E. Eikema, and W. Ubachs. Bounds on fifth forces from precision measurements on molecules. *Physical Review D*, **87**, 112008, 2013.
- [141] E. J. Salumbides, A. N. Schellekens, B. Gato-Rivera, and W. Ubachs. Constraints on extra dimensions from precision molecular spectroscopy. *New Journal of Physics*, **17**, 033015, 2015.
- [142] D. Sprecher, C. Jungen, W. Ubachs, and F. Merkt. Towards measuring the ionisation and dissociation energies of molecular hydrogen with sub-MHz accuracy. *Faraday Discussions*, **150**, 51–70, 2011.

- [143] K. Piszczatowski, G. Lach, M. Przybytek, J. Komasa, K. Pachucki, and B. Jeziorski. Theoretical determination of the dissociation energy of molecular hydrogen. *Journal of Chemical Theory and Computation*, **5**(11), 3039–3048, 2009.
- [144] K. Pachucki. Born-Oppenheimer potential for H₂. *Physical Review A*, **82**, 032509, 2010.
- [145] A. Osterwalder, A. Wüest, F. Merkt, and C. Jungen. High-resolution millimeter wave spectroscopy and multichannel quantum defect theory of the hyperfine structure in high Rydberg states of molecular hydrogen H₂. *Journal of Chemical Physics*, **121**, 11810, 2004.
- [146] M. L. Niu, E. J. Salumbides, G. D. Dickenson, K. S. E. Eikema, and W. Ubachs. Precision spectroscopy of the $X^1\Sigma_g^+, \nu = 0 \rightarrow 1(J = 0 - 2)$ rovibrational splittings in H₂, HD and D₂. *Journal of Molecular Spectroscopy*, **300**, 44–54, 2014.
- [147] R. K. Altmann, S. Galtier, L. S. Dreissen, and K. S. E. Eikema. High-Precision Ramsey-Comb Spectroscopy at Deep Ultraviolet Wavelengths. *Physical Review Letters*, **117**, 173201, 2016.
- [148] S. Hannemann, E. J. Salumbides, S. Witte, R. T. Zinkstok, E.-J. van Duijn, K. S. E. Eikema, and W. Ubachs. Frequency metrology on the $EF^1\Sigma_g^+ \leftarrow X^1\Sigma_g^+$ (0,0) transition in H₂, HD, D₂. *Physical Review A*, **74**, 062514, 2006.
- [149] A. Yiannopoulou, N. Melikechi, S. Gangopadhyay, J. C. Meiners, C. H. Cheng, and E. E. Eyler. Determinations of $EF^1\Sigma_g^+ \leftarrow X^1\Sigma_g^+$ transition frequencies in H₂, D₂, and HD. *Physical Review A*, **73**, 022506, 2006.
- [150] C. Benko, T. K. Allison, A. Cingöz, L. Hua, F. Labaye, D. C. Yost, and J. Ye. Extreme ultraviolet radiation with coherence time greater than 1 s. *Nature Photonics*, **8**, 530–536, 2014.
- [151] I. Barmes, S. Witte, and K. S. E. Eikema. Spatial and spectral coherent control with frequency combs. *Nature Photonics*, **7**, 38–42, 2013.
- [152] D. W. Chandler and L. R. Thorne. Measured radiative lifetimes for H₂ and HD in the E,F¹ Σ_g^+ electronic state. *The Journal of Chemical Physics*, **85**(4), 1733–1737, 1986.
- [153] M. Henrion and B. Fischhoff. Assessing uncertainty in physical constants. *American Journal of Physics*, **54**(9), 791–798, 1986.

- [154] G. Mana, E. Massa, and M. Predescu. Model selection in the average of inconsistent data: an analysis of the measured Planck-constant values. *Metrologia*, **49**, 492–500, 2012.
- [155] R. C. Mockler. Atomic Beam Frequency Standards. *IRE Transactions on Instrumentation*, **I-9**(2), 1960.
- [156] S. Y. T. van de Meerakker, H. L. Bethlem, and G. Meijer. Taming molecular beams. *Nature Physics*, **4**, 595–602, 2008.
- [157] N. F. Ramsey. Theory of Molecular Hydrogen and Deuterium in Magnetic Fields. *Physical Review*, **85**(1), 60–65, 1952.
- [158] M. Puchalski, J. Komasa, and K. Pachucki. Relativistic corrections for the ground electronic state of molecular hydrogen. *Physical Review A*, **95**, 052506, 2017.
- [159] L. Wolniewicz. Relativistic energies of the ground state of the hydrogen molecule. *The Journal of Chemical Physics*, **99**(3), 1851–1868, 1993.
- [160] B. Roth, U. Fröhlich, and S. Schiller. Sympathetic Cooling of $^4\text{He}^+$ Ions in a Radio-Frequency Trap. *Physical Review Letters*, **94**(5), 53001, 2005.
- [161] T. J. Pinkert, D. Z. Kandula, C. Gohle, I. Barmes, J. Morgenweg, and K. S. E. Eikema. Widely tunable extreme UV frequency comb generation. *Optics Letters*, **36**(11), 2026–2028, 2011.

Summary

Laser and microwave spectroscopy of simple atomic and molecular systems has played a crucial role in the development of quantum theories. In 1947 this resulted in the formulation of what is now called quantum electrodynamics (QED). QED is arguably the best tested theory in physics and a corner stone of the Standard Model. In the last two decades the improvement of experimental techniques, and most notably the invention of the frequency-comb laser, significantly enhanced the accuracy of spectroscopic experiments. At the level of accuracy now achieved in spectroscopic experiments, the comparison between theory and experiment is often limited by the uncertainty in the theoretical calculations, or the fundamental constants that are required for them. In the case of precision spectroscopy of atomic hydrogen, the current bottle neck is the accuracy of the Rydberg constant and the proton charge radius. However, because the experimental accuracy exceeds the theoretical precision, such a spectroscopic measurement can be used to determine the proton radius and Rydberg constant, under the assumption that QED is correct. This procedure led to a value for the proton-charge radius that is in agreement with the evaluation from electron-scattering experiments. This agreement between experiments and theory was disrupted in 2010 when results were published from a spectroscopy experiment based on muonic hydrogen. Although measurements on muonic hydrogen resulted in a more precise determination of the proton-charge radius, the obtained value deviated by more than five standard deviations from the electronic hydrogen value. This discrepancy between experimental results is now called the proton radius puzzle. More recent measurements of the proton charge radius in different systems, and on several transitions, have resulted in results that agree with either the small (muonic) value of about 0.84 fm, or the larger value of 0.88 fm that was found originally from electron scattering and hydrogen spectroscopy.

It is crucial that this conundrum is resolved because it could indicate new physics beyond the Standard Model, much like the discovery of the Lamb shift which led to the development of QED. To tackle this problem, novel experiments are required to gather information and provide new input for the theoretical efforts. One suggestion for new experiments is to make a similar comparison in singly ionized helium as in hydrogen, to complement the experiments on hydrogen with a different nucleus. Experimentally this is challenging because XUV radiation is required to excite the 1S-2S transition. A different route to determine the proton-charge radius is made possible by recent breakthroughs in calculation of molecular QED theory. This gives good prospects to

resolve the proton charge radius from sufficiently accurate spectroscopy of molecular hydrogen, the benchmark system for molecular quantum theory and spectroscopy. Also in this system, the required wavelength of ~ 200 nm makes high-resolution spectroscopy difficult. Our group aims to make these experiments possible, and in this thesis high-resolution spectroscopic experiments are described that demonstrate the feasibility of these efforts.

In Chapter 2 of this thesis the concept of the frequency-comb laser is introduced and the principle and analysis of Ramsey-comb spectroscopy is explained. Ramsey-comb spectroscopy is based on a combination of Ramsey's method of separated oscillatory fields and frequency-comb pulses. Ramsey excitation, or quantum-interference metrology, has proven to be extremely fruitful and is now applied in many laboratories around the world, most notably in cesium atomic clocks and other microwave frequency standards. In our application of Ramsey's method, the phase evolution of an atom is probed with two frequency-comb laser pulses that are separated by a time delay. In the case of excitation with two phase-locked pulses, the relative phase of the contribution to the induced ground- and excited-state superposition is determined by the time delay between the excitation pulses and their relative phase. By adjusting the time delay of two such pulses with sufficient resolution and accuracy, a quantum interference signal can be probed from which the transition frequency is determined. In Ramsey-comb spectroscopy a series of quantum-interference signals is measured by selecting frequency-comb pulse pairs at multiples of the original repetition time. Combining these signals, and performing the analysis on all of them simultaneously constitutes a Ramsey-comb measurement. The maximum time delay between the excitation pulses is limited to several times the excited state lifetime, allowing for high-precision measurements. Moreover, the frequency-comb pulses can be amplified to very high-pulse energies and used for efficient frequency up-conversion.

To perform Ramsey-comb measurements with deep-ultraviolet frequency-comb pulses a complicated laser setup is required, which is described in Chapter 3 of this thesis. The heart of the setup is a frequency-comb based on a mode-locked Ti:sapphire laser. The frequency-comb pulses are used to seed an optical parametric amplifier (OPA) where two pulses are selectively amplified. The pump pulses for this device are delivered by a separate laser system that is based on a passive mode-locked oscillator operating at 1064 nm. The repetition rate of the pump laser is synchronized with the frequency comb because precise temporal overlap of the frequency-comb and pump pulses is required for amplification in the OPA. To be able to amplify different pairs of frequency-comb laser pulses, pulses with adjustable inter-pulse delay are selected from the pump-pulse train using fast electro-optic modulators. These two pulses are

amplified by several amplification stages up to a pulse energy of 27 mJ. They are then frequency doubled to 532 nm through frequency up-conversion in a BBO crystal, and used to pump the OPA. After the parametric amplification process, the two amplified frequency-comb pulses have an energy of 1-2 mJ which can be used for efficient up-conversion. One crucial detail of this setup is that the amplification process influences the phase of the frequency-comb pulses, which potentially can lead to a frequency-shift in the interpretation of a Ramsey-comb measurement. To ensure that the phase is stable as a function of the inter-pulse delay, the relative phase of the amplified frequency-comb pulses is measured based on spectral interferometry in a Mach-Zehnder type interferometer.

In chapter 4 of this thesis we demonstrate Ramsey-comb spectroscopy in the deep ultraviolet for the first time. ^{84}Kr is excited in an atomic beam on the two-photon $4p^6 \rightarrow 4p^5 5p[1/2]_0$ transition at 212.55 nm. The 212.55 nm radiation is generated by frequency quadrupling the amplified frequency-comb pulses using two sequential stages of BBO-crystals. The resulting deep-UV beam is split in equal parts by a beam-splitter, which enables to excite the two-photon transition in a counter-propagating laser beam configuration so that the first-order Doppler shift is reduced. The collision point of the excitation pulses is overlapped with an atomic beam based on a pulsed supersonic expansion of krypton atoms. After the excitation pulses, an ionization pulse at 532 nm is applied which only ionizes krypton atoms that are in the excited state. The resulting ions are extracted and detected using a channel-electron multiplier (CEM). In addition, a time of flight drift tube between the laser excitation point and the detector separates the krypton isotopes. This time-of-flight measurement enables to resolve the signals of the different isotopes.

It is shown that the AC-Stark shift is effectively eliminated, and combined with the counter-propagating excitation geometry to suppress Doppler effects, a transition frequency of 2,820,833,101,679(103) kHz is found. The uncertainty of our measurement is 34 times smaller than the best previous measurement, and mainly limited by the 27 ns lifetime of the excited state. This result demonstrates the power of the Ramsey-comb method for transitions in the deep-UV wavelength range.

In chapter 5 we report on the determination of the $EF^1\Sigma_g^+ - X^1\Sigma_g^+(0,0)$ Q1 transition in H_2 by employing Ramsey-comb two-photon spectroscopy in the deep ultraviolet at 201.80 nm. This is an essential ingredient for determining the dissociation energy (D_0) of molecular hydrogen and the fundamental ground tone (FGT), which serve as important benchmark numbers for molecular quantum physics. Advances in molecular energy structure calculations enable testing of quantum electrodynamics and potentially a determination of the proton charge radius from H_2 spectroscopy.

The 201 nm radiation is created through three sequential steps of frequency doubling and sum-frequency generation in BBO crystals. The transition is then excited in a counter propagating beam configuration to suppress the first-order Doppler shift. After the excitation pulses, another laser pulse is applied that state-selectively ionizes the hydrogen molecules. The ionized molecules are extracted using pulsed electrical fields and detected with an electron multiplier. With this setup Ramsey-comb measurements are performed and Ramsey fringes are observed up to a maximum delay time of 380 ns, corresponding to a separation of 48 times the frequency-comb repetition time.

Taking all systematic effects into account, we determined a transition frequency of 2971 234 992 965(73) kHz for the $EF^1\Sigma_g^+ - X^1\Sigma_g^+(0,0)$ Q1 transition in ortho- H_2 . The relative uncertainty of this result is $2.5 \cdot 10^{-11}$, and is in agreement with the previous measurement, but two orders of magnitude more accurate. The new two-photon transition frequency of the Q1 line of ortho-hydrogen can be used to obtain an improved value for the (rotation-less) dissociation energy D_0 of para-hydrogen, and the result is consistent with previous experimental determinations and theory.

The experimental results achieved with krypton and molecular hydrogen demonstrate that the amplified frequency-comb pulses can be upconverted efficiently and used for high-precision spectroscopy. With minor modifications the experimental setup can be used to measure additional level energies in molecular hydrogen for more precise determinations of the fundamental ground tone and the dissociation energy. This is briefly discussed in chapter 6 (outlook), together with a new experimental setup that is under construction to enable spectroscopy on singly-ionized helium at 32 nm, based on a combination of high-harmonic generation and Ramsey-comb spectroscopy. This would allow a new precise test of QED, or it could be used to determine either the alpha-particle radius or the Rydberg constant.

Samenvatting

Laser spectroscopie aan eenvoudige atomaire en moleculaire systemen heeft een cruciale rol gespeeld in de ontwikkeling van de kwantumtheorie. Dit resulteerde, in 1947, in de totstandkoming van wat nu bekend staat als de Kwantumelektrodynamica, of QED (van Quantum Electrodynamics). QED is wellicht de meest rigoureuze getoetste theorie in de natuurkunde, en is een essentieel onderdeel van het Standaard Model. Gedurende de laatste twee decennia heeft de verbetering van experimentele technieken, en vooral de ontwikkeling van de frequentiekam laser, er toe geleid dat de precisie van spectroscopische experimenten significant is verbeterd. De meetnauwkeurigheid die behaald kan worden in de huidige spectroscopie is zo hoog dat de vergelijking met theorie vaak gelimiteerd is door de onzekerheid in de berekeningen, of door de nauwkeurigheid van de fundamentele natuurconstanten die nodig zijn voor deze berekeningen. Voor precisionspectroscopie aan atomair waterstof is het knelpunt in de vergelijking met theorie de onzekerheid in de Rydbergconstante, en de proton radius. Omdat de experimentele precisie de theoretische precisie overtreft, kan een dergelijke meting ook gebruikt worden voor het bepalen van de protonstraal en Rydbergconstante, als aangenomen wordt dat QED correct is. Door middel van deze procedure is een protonstraal bepaald die in overeenstemming is met metingen op basis van elektron verstrooiing experimenten. Deze consensus tussen experiment en theorie werd verstoord in 2010 na de publicatie van spectroscopie experimenten aan muonisch waterstof. In dit experiment is een protonstraal bepaald met een (veel) lagere meetonzekerheid, echter, de absolute waarde week meer dan vijf standaarddeviaties af het resultaat behaald met elektronisch waterstof. Deze discrepantie tussen experimentele resultaten wordt ook wel de "protonstraal puzzel" genoemd. Recente metingen van de protonstraal in andere systemen, en overgangen, zijn ofwel in overeenstemming met de muonische waarde van ongeveer 0.84 fm, of met de waarde van 0.88 fm die oorspronkelijk met spectroscopie in gewoon waterstof en met electronverstrooiing werd gemeten.

Het is van wetenschappelijk belang dat dit raadsel wordt opgelost omdat het een indicatie kan zijn van nieuwe fysica, zoals ook het geval was met de ontdekking van de Lamb verschuiving die heeft geleid tot de ontwikkeling van QED. Om dit probleem op te lossen zijn er nieuwe experimenten noodzakelijk, waarvan de resultaten kunnen dienen als input voor de theoretische inspanningen. Een mogelijkheid is het maken van een zelfde vergelijking in enkelvoudig geïoniseerd helium; dit zou de waterstof metingen complementeren met een andere kern. Experimenteel is dit zeer uitdagend vanwege

de extreem-ultraviolet (XUV) straling die nodig is voor het aanslaan van de 1S-2S overgang He^+ . Een ander alternatief voor het bepalen van de protonstraal is recent mogelijk gemaakt door grote vooruitgang van quantummechanische berekeningen (inclusief QED) van de energieniveaus van moleculen. Die ontwikkelingen bieden perspectief om de protonstraal te bepalen door middel van precisiespectroscopie aan moleculair waterstof, het ijksysteem voor moleculaire kwantumtheorie en spectroscopie. Echter, ook voor H_2 is de vereiste golflengte van ~ 200 nm experimenteel een beperkende factor. Onze onderzoeksgroep heeft als doel deze experimenten te realiseren, en in dit proefschrift worden Ramsey-comb experimenten beschreven die de haalbaarheid hiervan aantonen.

In hoofdstuk 2 van dit proefschrift wordt het concept van de frequentiekamlaser geïntroduceerd, en wordt het principe en de analyse van Ramsey-comb spectroscopie uitgelegd. Ramsey-comb spectroscopie is gebaseerd op een combinatie van Ramsey's gescheiden-veld excitatie methode en frequentiekampulsen. Ramsey excitatie, of kwantum-interferentie metrologie, is een zeer nuttige methode en wordt toegepast in bijvoorbeeld atomaire klokken en andere microgolf frequentiestandaarden. In onze toepassing van Ramsey's methode wordt de fase-evolutie van een atoom door middel van twee in de tijd gescheiden frequentiekampulsen gemeten. De relatieve fase tussen de superpositie van grond- en aangeslagen-toestand geïnduceerd door de twee laser pulsen wordt bepaald door de fase evolutie van het atoom (de overgangsfrequentie) en de fase-evolutie van de laserpulsen zelf. Door het tijdsverschil tussen de pulsen te variëren, met voldoende nauwkeurigheid en resolutie, kan het resulterende kwantuminterferentiesignaal worden gemeten, op basis waarvan de overgangsfrequentie kan worden bepaald. In Ramsey-comb spectroscopie wordt een serie kwantuminterferentiesignalen gemeten door paren van frequentiekampulsen te selecteren met een tijdsafstand gelijk aan veelvouden van de originele repetitie tijd van de laser. Het combineren en gelijktijdig analyseren van een dergelijke meetserie vormt een Ramsey-comb meting. De tijdsduur tussen de pulsen kan een aantal maal de levensduur van de aangeslagen toestand zijn, wat zeer precieze metingen mogelijk maakt. Tevens kunnen de frequentiekampulsen worden versterkt tot een zeer hoge pulsenergie; daardoor kunnen deze worden gebruikt voor efficiënte frequentieconversie in non-lineaire processen.

Het uitvoeren van een Ramsey-comb meting met diep-ultraviolette frequentiekampulsen vereist een gecompliceerde opstelling. In hoofdstuk 3 van dit proefschrift wordt deze opstelling gedetailleerd beschreven. Het hart van de opstelling wordt gevormd door een frequentiekam die gebaseerd is op een gemodelockte titaan-saffierlaser. De frequentiekampulsen worden gebruikt voor het aandrijven van een optische parametrische

versterker (OPA) waarin selectief twee pulsen worden versterkt. De 'pomp'-pulsen voor deze versterker worden gegenereerd in een apart laser systeem dat gebaseerd is op een passief-gemodelockte oscillator die opereert bij een golflengte van 1064 nm. De repetitiefrequentie van pomp laser is gesynchroniseerd met de frequentiekam laser, omdat nauwkeurige temporele overlap vereist is voor versterking in de OPA. Uit de 'pomp'-pulstrein worden twee pulsen met geselecteerd door middel van snelle elektro-optische modulators, dit maakt het mogelijk verschillende frequentiekam pulsparen te versterken. De twee geselecteerde pomp-pulsen worden versterkt in twee versterking trappen tot een pulsenergie van 27 mJ. Daaropvolgend worden deze pulsen verdubbeld in optische frequentie naar 532 nm, en gebruikt om de OPA te 'pompen'. Na de parametrische versterking hebben de frequentiekampulsen dan een energie van 1-2 mJ. Een cruciaal detail van deze opstelling is dat het versterkingsproces de fase van de frequentiekampulsen kan beïnvloeden, wat weer kan leiden tot een frequentiever-schuiving in de interpretatie van een Ramsey-comb meting. Om zeker te zijn dat de fase stabiel is als functie van het tijdsverschil tussen de pulsen, wordt de relatieve fase tussen de versterkte kampulsen gemeten op basis van spectrale interferentie in een Mach-Zehnder interferometer.

In hoofdstuk 4 worden de eerste Ramsey-comb spectroscopie meting in het diep-ultraviolette deel van het spectrum gepresenteerd. In een atoombundel van ^{84}Kr wordt de twee-foton overgang $4p^6 \rightarrow 4p^5 5p[1/2]_0$ aangeslagen met 212.55 nm. De 212.55 nm wordt gegenereerd in twee opeenvolgende frequentie-verdubbeling stappen van de versterkte kampulsen door middel van niet-lineaire wisselwerking in twee BBO kristallen. De resulterende UV bundel wordt in twee gelijke delen gesplitst, om daarmee de twee-foton overgang aan te slaan met tegengesteld propagerende laserbundels. Door deze configuratie wordt de eerste-orde Doppler verschuiving sterk onderdrukt. Het intersectiepunt van de excitatie pulsen wordt overlapt met een atoombundel, gebaseerd op een supersonische expansie van krypton atomen. Na de excitatiepulsen wordt een 532 nm laserpuls gebruikt om de atomen die zich in de aangeslagen toestand bevinden te ioniseren. De gecreëerde krypton ionen worden vervolgens geëxtraheerd en gedetecteerd door middel van een channel electron multiplier (CEM).

Een opmerkelijk resultaat is dat het AC-Stark (invloed van de laserintensiteit op het atoom) effect vrijwel volledig onderdrukt wordt, en in combinatie met de onderdrukking van het Doppler effect is een overgangsfrequentie 2 820 833 101 679(103) kHz bepaald. De onzekerheid van deze meting is 34 maal kleiner dan de beste meting tot op heden, en wordt vooral gelimiteerd door de levensduur van 27 ns van de aangeslagen toestand. Dit resultaat toont de effectiviteit van de Ramsey-comb methode aan voor overgangen in het diep-ultraviolette deel van het spectrum.

In hoofdstuk 5 rapporteren wij de bepaling van de twee-foton $EF^1\Sigma_g^+ - X^1\Sigma_g^+(0,0)$ Q1 overgang in H_2 door gebruik te maken van de Ramsey-comb opstelling bij 201.80 nm. Dit is een essentieel ingrediënt door het bepalen van de dissociatie energie en de fundamentele grondtoon van moleculair waterstof, beide belangrijke ijkpunten in moleculaire kwantum fysica. Recente doorbraken in berekeningen aan de moleculaire energie structuur maken het steeds beter mogelijk QED te toetsen, en potentieel de straal van het proton te bepalen op basis van H_2 spectroscopie.

De vereiste 201 nm straling wordt gegenereerd door drie opeenvolgende stappen van frequentie verdubbeling en som-frequentie mixing. De overgang wordt vervolgens aangeslagen door twee tegengesteld propagerende laserbundels, dit om de eerste-orde Doppler verschuiving te onderdrukken. Door middel van een ionisatie puls worden de moleculen in de aangeslagen toestand geïoniseerd, en vervolgens met een gepulst elektrisch velden omhoog bewogen en gedetecteerd. Met deze opstelling zijn Ramsey oscillaties gemeten tot een maximaal tijdsverschil tussen de excitatie pulsen van 380 ns, wat correspondeert met 48 maal de repetitie tijd van de frequentiekam.

Na evaluatie van alle systematische effecten is een overgangsfrequentie van 2 971 234 992 965(73) kHz bepaald voor de $EF^1\Sigma_g^+ - X^1\Sigma_g^+(0,0)$ Q1 overgang in ortho- H_2 . Deze waarde is in overeenstemming met eerdere resultaten, maar de relatieve onzekerheid van $2.5 \cdot 10^{-11}$ is een verbetering met bijna een factor honderd. Deze verbeterde overgangsfrequentie kan gebruikt worden voor een betere bepaling van de (rotatie-vrije) dissociatie-energie, en de gevonden waarde is consistent met de eerdere experimentele bepaling en theorie.

De resultaten die behaald zijn met krypton en moleculair waterstof tonen aan dat de versterkte frequentiekampulsen gebruikt kunnen worden voor efficiënte frequentie op-conversie en precisespectroscopie experimenten. Met enkele aanpassingen aan de opstelling kunnen andere overgangen in moleculair waterstof gemeten worden. Zodoende kan de dissociatie energie en de fundamentele grondtoon nog preciezer worden bepaald. Dit staat kort beschreven in hoofdstuk 6 (Outlook), tezamen met een nieuwe experimentele opstelling die wordt opgebouwd om spectroscopie aan enkelvoudig geïoniseerd helium bij 32 nm mogelijk te maken. Dit is gebaseerd op een combinatie van hoge-harmonische generatie en Ramsey-comb spectroscopie. Hiermee zou op termijn een bijzonder nauwkeurige QED test gedaan kunnen worden, of in plaats daarvan een bepaling van de Rydberg constante of de straal van het alpha-deeltje.

Acknowledgements

Dit proefschrift was niet tot stand gekomen zonder hulp van een aantal mensen die er aan heeft bijgedragen. Het dankwoord wil ik dan ook graag beginnen met het bedanken van mijn promotiebegeleider Kjeld Eikema. Kjeld, ik ben diep onder de indruk van wat jij hier in Amsterdam aan experimenten hebt weten op te bouwen, wat echt van wereld niveau is. Dat is te danken aan de eindeloze hoeveelheid energie die jij erin stopt, en het enthousiasme waarmee jij dit werk doet. Ik wil je bedanken voor de kans die jij mij hebt gegeven om deel uit te maken van deze omgeving. Ik kijk met veel plezier terug op de jaren die ik in het lab heb kunnen werken. Ook wil graag mijn copromotor Wim Ubachs bedanken. Niet alleen heb jij een belangrijk aandeel geleverd in, met name, het laatste deel van dit proefschrift, het is ook met dank aan jou dat de AML groep een mooie, levendige en stimulerende plaats is om onderzoek te doen.

Ondertussen is de onderzoeksgroep behoorlijk gegroeid, maar toen ik net kwam kijken was ik een geruime tijd alleen. Ik wil de gelegenheid aangrijpen om Laura te bedanken voor het doorbreken van die eenzaamheid, en dat zij ervoor koos om bij ons in de groep te komen promoveren. Niet alleen heb jij mij veel geholpen met experimenten en discussies, maar jouw echte Amsterdamse spirit, eerlijkheid en humor hebben ervoor gezorgd dat het geen dag meer saai is geweest. Dankzij jou heb ik veel kunnen lachen tijdens talloze bakkies koffie, praatjes op conferenties en biertjes in het café. Ik hoop dat wij onze vriendschap nog lang kunnen voortzetten. I would also like to thank Sandrine, who came to join us in the lab shortly after Laura. Sandrine, I found working with you very enjoyable due to your relaxed and calm attitude. I will remember your friendliness the most, and wish you much success in your academic career.

Dan wil ik ook graag de "lensless XUV" mannen Stefan, Matthijs en Daniel (en later versterkt door Denis) bedanken voor alle discussies en inzichten die we hebben gedeeld, onder andere tijdens het groepsoverleg deel II. Jullie expertise op het gebied van (XUV) lasers was vaak een nuttige bron van informatie, en daarnaast hebben jullie kritische vragen en nieuwe inzichten een belangrijk aandeel geleverd in dit werk.

Verder wil ik graag Jeroen Koelemeij, Rick Bethlem, Wim Vassen en Steven Knoop bedanken voor hun aandeel in de groep, en alle discussies en vragen tijdens het groepsoverleg en andere besprekingen. Ondanks dat jullie niet direct betrokken waren bij mijn project heb ik veel van jullie kunnen leren.

Ook Rob Kortekaas wil ik bedanken, een cruciale schakel in de (mechanische) keten. Hoewel we niet hebben samengewerkt aan grote projecten stond je wel altijd klaar om mij te helpen met problemen en het aandragen van uitstekende oplossingen. Verder heb ik genoten en veel geleerd van je nuchtere en praktische kijk op problemen.

My time as a PhD student would undoubtly have been much more difficult and less fun if not for all the colleagues at the LaserLaB that I had the pleasure to work and interact with. In particular I would like to thank Edcel for helping me many times with practical (UV) issues as well as (molecular) theoretical issues. Also, I find your positive attitude contagious, and I really appreciated your presence and the atmosphere you brought to the whole group. Ook Remy, kerel, het was mooi om deze jaren met jou te hebben gewerkt. Vooral woordgrappen zullen nog wel even herinneringen aan jou oproepen.

Dan wil ik ook graag mijn ouders bedanken, jullie hebben altijd in mij geloofd en dankzij de onvoorwaardelijke steun die jullie mij hebben geboden heb ik mij altijd zeker gevoeld. Als laatste wil ik Shira bedanken, jij bent onlosmakelijk verbonden aan dit werk. Jij hebt al het mogelijke gedaan om mij te helpen bij mijn onderzoek, waardoor ik altijd zonder zorgen tijdens menig weekend en avond heb kunnen schrijven. Ook heb jij met mij de successen gevierd vooral als ik dat zelf niet deed; bedankt voor alles.